Direction-sensitive dark matter search
with a gaseous micro time projection chamber

Kiseki Nakamura

2014.01.06

Abstract

Non-baryonic dark matter is widely believed to account for a large fraction of the mass in the universe by a lot of observation of the universe. Weakly Interacting Massive Particle (WIMP) is the leading candidate of the dark matter. Many direct search experiments of dark matter have been performed so far. Although some experiments have reported positive results, no experiment has reached a widely agreed discovery. A more reliable method, direction-sensitivity, is expected to provide a strong evidence of the dark matter. We developed a direction-sensitive dark matter detector, NEWAGE-0.3b' to improve the sensitivity by one order of magnitude from our previous measurement performed by NEWAGE-0.3a. NEWAGE-0.3b' was designed to have a twice larger target volume with low background material, a lowered threshold of $50\,\mathrm{keV}$, an improved data acquisition system, and a gas circulation system with cooled charcoal. A direction-sensitive dark matter search in Kamioka underground laboratory with NEWAGE-0.3b' was performed from July 17th, 2013 to November 12th, 2013. With an exposure of $0.327\,\mathrm{kg\cdot days}$, a new 90% C.L. direction-sensitive SD cross section limit $557\,\mathrm{pb}$ for WIMP mass of $200\,\mathrm{GeV/c^2}$ was obtained. This result improved the limit by ~ 10 times from previous measurement, and marks the best direction-sensitive limit. From the detail study on the remaining background, radon gas and the substrate of μ-PIC was found to be the dominant background source, and prospects for future improvements were discussed.

Contents

Chapter 1

Introduction

Dark matter is one of the biggest puzzle of the universe. In 1960s, the modern cosmology was started by both the theory of relativity and observations of Cosmic Microwave Background (CMB). In particular, recent observations of CMB[1], Baryon Acoustic Oscillation (BAO)[2], and far distant Type Ia Supernovae[3], favor a flat universe consisting of 68.3 % dark energy, 26.8 % dark matter, and 4.9 % baryon (ordinary matter), as shown in Figure 1.0.1. According to these "understandings", the dark matter is not ordinary baryonic matter and it is very likely to a particle in new physics beyond the Standard Model (SM) of the particle physics. In this section, studies on the dark matter from the viewpoints of astrophysics (Section 1.1) and particle physics (Section 1.2) are discussed, then the dark matter search experiments (Section 1.3) are reviewed.
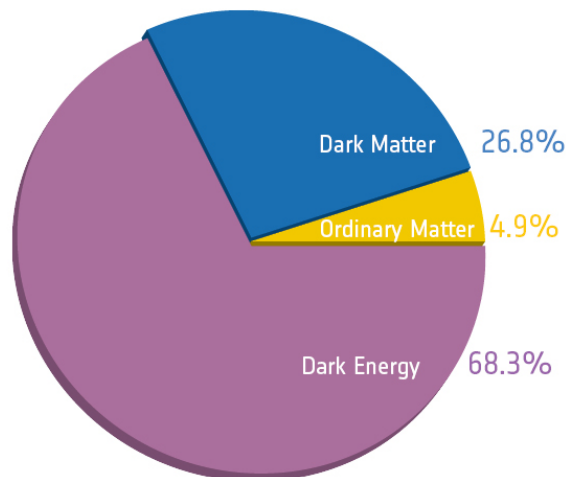
Figure 1.0.1: Composition of the energy of the universe. The universe was known to consist of 68.3 % dark energy, 26.8 % dark matter, and 4.9 % baryon (ordinary matter) from recent observations[1]
.

1.1 Astrophysical dark matter : evidences

The dark matter was introduced by Zwicky in 1930s[4]. He studied the motions of galaxies in Coma Cluster and Virgo Cluster, and noticed that the velocities of galaxies were too high to keep them in a cluster by the gravity potential of visible galaxies. Thus he introduced "dark matter" as an invisible matter to keep them in a cluster. The mass of the dark matter was thought to be 10 to 100 times larger than the visible matter. Owing to the following observations of galaxies and clusters, we now have a lot of evidences of dark matter as invisible mass. Also, non-baryonic mass is required in the whole universe from the measurements of chemical component of primordial nucleosynthesis.

1.1.1 Rotation curve of the galaxy

Galaxy rotation problem was reported in 1970s. This problem is that a galaxy rotation velocity in the outer part is too high to keep the stars within a galaxy. To solve this problem, additional invisible mass providing sufficient gravitational potential was needed to explain the rotation of the galaxy. The star's rotation velocity in a galaxy is calculated from Kepler's law as

$$\frac{v_c^2(r)}{r} = G\frac{M(r)}{r^2}, \tag{1.1}$$

where r is a radial distance from the center of the galaxy, $v_c(r)$ is a rotation velocity as the function of r, and $M(r)$ is a total mass within the radius r. The rotation velocity was measured from observations of the Doppler shift of bright lines in the spectra of stars, using $21\,\mathrm{cm}$ and $3.6\,\mathrm{mm}$ lines of the HI gas (neutral hydrogen gas) and the CO gas. If a galaxy consisted of only visible stars, the rotation velocity v must have fallen as $r^{-1/2}$ because observed stars concentrated at the center of the galaxy. However, the measured rotation velocity was almost constant even the outer region of the galaxy where the population of visible stars were very low. This observational result implies that the mass distribution $M(r)$ was proportional to r even at a large radius, and the galaxy must contains large amount of invisible mass, or the dark matter.

Figure 1.1.1 is the rotation curve of NGC6503 galaxy measured by Doppler shift of $21\,\mathrm{cm}$ line[5]. This galaxy is a typical spiral galaxy with a $2\,\mathrm{kpc}$ radius core and a luminous disk expanding to more than $\sim 5\,\mathrm{kpc}$ from the center of the galaxy. Since the measured rotation curve was flat even up to the outer region, dark matter is required in the galaxy halo.
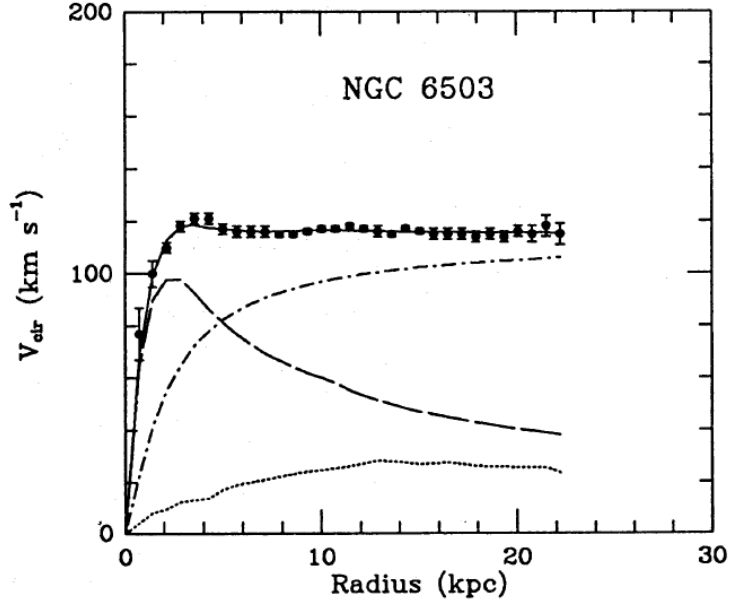
Figure 1.1.1: The rotation curve of NGC6503 spiral galaxy. The black points are measured velocity by Doppler shift of 21 cm line[5]. The dashed line and dotted line are the contribution to the rotation velocity from the observed disk and gas, respectively. The dashed-dotted line is the contribution from the invisible mass at the galaxy halo. The solid line is a sum of them.

1.1.2 X-ray observation of the cluster of galaxy

A cluster of galaxies is a largest structure in the universe where $100 - 1000$ galaxies concentrate. The existence of the dark matter in the cluster of galaxies scale was noticed from the X-ray observation of the cluster of galaxies since 1980s.

X-ray observation for the cluster of galaxies enabled us to see the distribution of high temperature gas. As a result, it was found out that clusters of galaxies was filled with high temperature plasma of about $10^7 \sim 10^8$ K and that almost all baryons exist as plasma instead of stars. Since such high temperature plasma becomes high pressure, the cluster of galaxies needs a gravitational potential to keep galaxies inside. Calculated necessary mass was $10 - 100$ times as much as the sum of the galaxies and plasma in a cluster. Thus, the dark matter was suggested to sustain the distribution of cluster of galaxies scale.

In the X-ray observation of clusters of galaxies Abell1060 and AWM7 by ASCA (Japanese X-ray satellite), the baryon fractions at clusters of galaxies was derived as shown in Figure 1.1.2[6]. Obtained baryon fractions were less than ~ 0.2, and then it revealed the existence of dark matter around a cluster of galaxies.
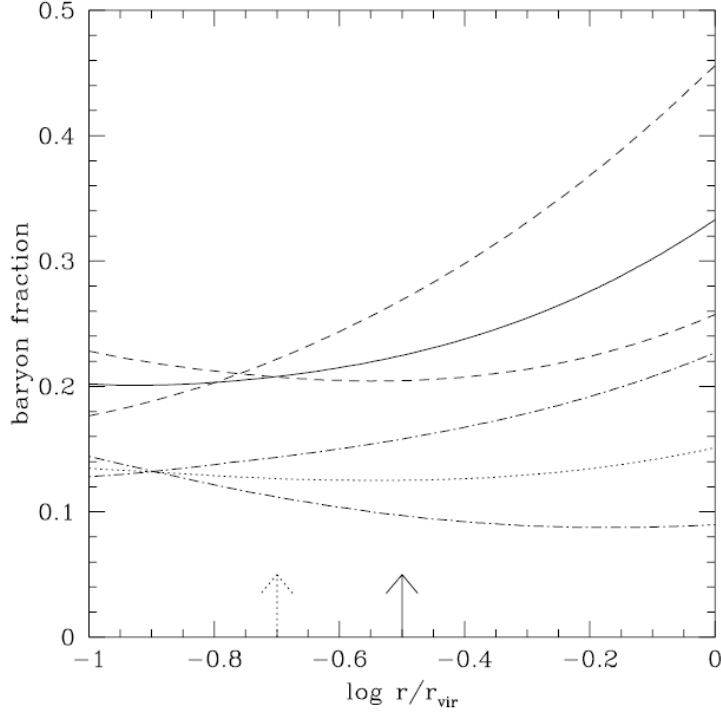
Figure 1.1.2: The baryon fraction of galaxy clusters Abell1060 and AWM7 observed by ASCA[6]. Horizontal axis is distance from the center of galaxy clusters normalized by r_{vir}. r_{vir} is the $2 \pm 0.5\,\mathrm{Mpc}$ and $2 \pm 0.4\,\mathrm{Mpc}$ for Abel1060 and AWM7 were taken, respectively. Solid line and dotted line show the best fit model corresponding to Abel1060 and AWM7, respectively. Dashed line and dot-dash line show the model in case most compact and most expanded, respectively.

1.1.3 Weak gravitational lensing of Bullet Cluster

1E 0657-558, so-called "Bullet Cluster", is the region where galaxy clusters collide. Another dark matter evidence was observed in this region by weak gravitational lensing.

Gravitational lensing is the phenomenon that the light from a distant source (a background galaxy) toward an observer is bended by a distribution of the gravitational potential between the source and the observer. Then the background object is observed to be multiplied or amplified or warped. When a gravitational potential is not so strong, a background galaxy is just warped, and this phenomenon is called "weak gravitational lensing." Using weak gravitational lensing, we can evaluate the shape and the amount of the gravitational potential with a statistical analysis of the warps of galaxies.

The region around 1E 0657-558 was observed by Hubble Space Telescope to evaluate the mass distribution through weak gravitational lensing observation and statistical analysis. Obtained mass distribution was the green contour in Figure 1.1.3. In addition, the optical and
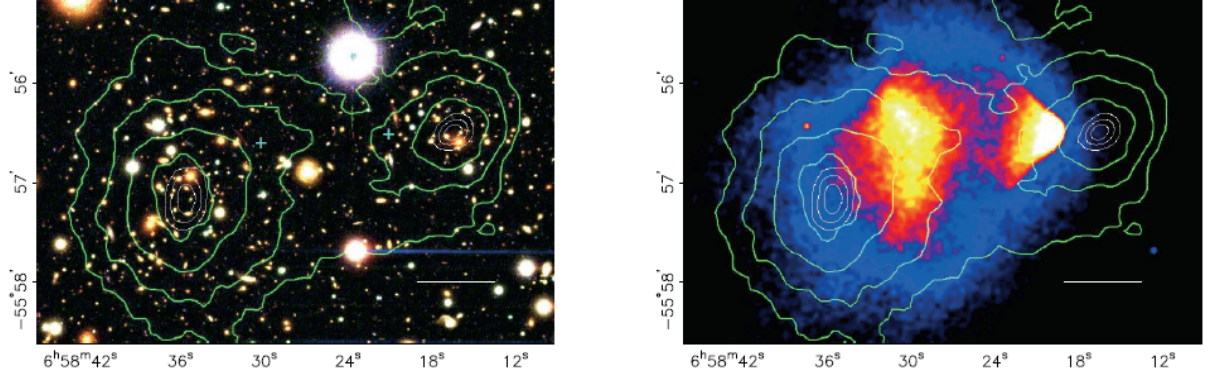
Figure 1.1.3: Space distribution of 1E 0657-558 where galaxy cluster collided. Left color image, right one and green contour represent space distribution measured by optical, X-ray and gravitational lensing, respectively. [7]. The green contour in both figure is the distribution of gravitational potential measured by weak gravitational lensing.

X-ray radiation distribution observed by Magellan telescope and Chandra satellite are shown in the left and the right, respectively. The high temperature plasma observed by the X-ray expanded about 0.72 Mpc and the right side cluster is moving away from the left side one at ~ 4700 km/s. As a line-of-sight velocity is only ~ 600 km/s, the collision occurred nearly in the plane of the sky. From these observations, gravitational potential does not trace the plasma distribution and obtained the picture that weakly interacting dark matter goes ahead in contrast to the viscous plasma. This result is one of the clear evidence of the existence of the dark matter at a cluster of galaxies scale.

1.1.4 Cosmological parameters

Cosmology is the theory which covers the whole universe. The ΛCDM model, one of the Big Bang cosmological model including a cosmological constant denoted by Λ and cold dark matter (CDM), is now considered as a standard model of cosmology. In the ΛCDM model, the energy densities of the universe components are normalized by a critical density $\rho_{\rm c} \left(= \frac{3c^2 H_0^2}{8\pi G} \right)$, and called cosmological parameters. The normalized parameters, the dark energy, the matter and the radiation are referred to as Ω_Λ, $\Omega_{\rm m}$ and $\Omega_{\rm r}$, respectively. Only $\Omega_{\rm r}$ is accurately measured directly as following. The radiation density is dominated by the energy of the CMB, and several satellite observations determined its temperature to be T $= 2.72548 \pm 0.00057$K, corresponding to $\Omega_{\rm r} h^2 = 2.47 \times 10^{-5}$[8], where h is Hubble parameter normalized by 100. $\Omega_{\rm r}$ is negligible compared with $\Omega_{\rm m}$ after the transition from the radiation dominant era to the matter dominant era at the early universe ($z \sim 10^4$). When we consider baryon and dark matter separately, matter($\Omega_{\rm m}$) is divided into baryon($\Omega_{\rm b}$) and dark matte($\Omega_{\rm DM}$).

Here, we briefly explain the cosmological parameters. The evolution of the scale factor a, representing the size of universe, is written as

$$\left(\frac{\dot{a}}{a}\right)^2 = H_0^2 \left\{\frac{\Omega_m}{a^3} + \frac{\Omega_r}{a^4} + \Omega_\Lambda - \frac{\Omega_k}{a^2}\right\}, \tag{1.2}$$

where, H_0 is Hubble constant and Ω_k is the normalized curvature of the universe. Equation (1.2) is the normalized Friedmann equation and derived from general relativity assuming a homogeneous isotropic universe. By solving this differential equation, we can evaluate the time evolution of the universe and investigate the universe constriction/expansion, the flatness of the universe, and the existence of the Big Bang. The evolution depends on cosmological parameters and the observational results on cosmological parameters are shown in Figure 1.1.4. There are several observations to determine the cosmological parameters; the observations of Type Ia Super Nova (IaSN)[3], Cosmic Microwave Background (CMB)[1], and Baryon Acoustic Oscillation (BAO)[2] representatively. Each observation set the limit or allowed region of the cosmological parameters as shown in Figure 1.1.4.
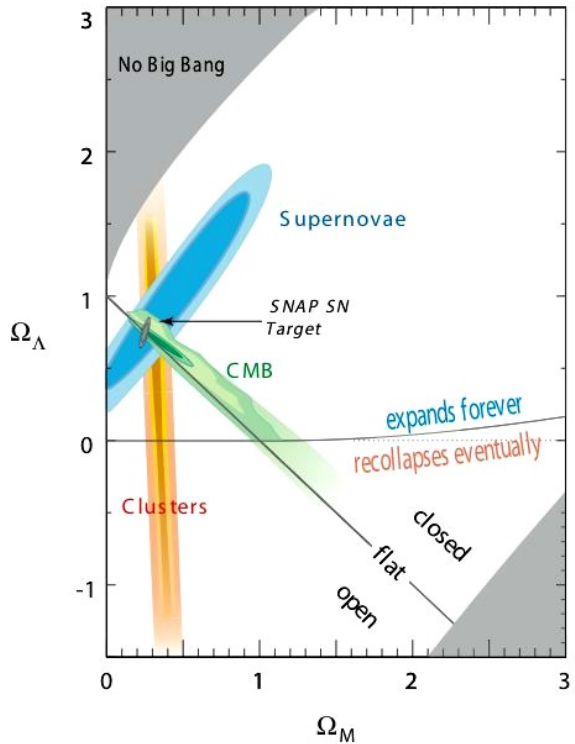
Figure 1.1.4: Allowed regions of cosmological parameters (Ω_Λ, Ω_m) by observations of IaSN ("Supernovae" in figure)[3], CMB[1], and BAO ("clusters" in figure) [2]. A flat universe with (Ω_Λ, Ω_m) $\simeq (0.7, 0.3)$ is favored by each three observations.

A Type Ia Super Nova (IaSN) explosion occurs when a white dwarf in a binary system getting mass accretion from a companion star reaches to the Chandrasekhar mass. Thus, the maximum luminosity of IaSN is considered to be constant in spite of individual situations. In addition, a super nova is so luminous phenomenon that we can investigates a distant universe over $z \sim 1$. The redshift of IaSN spectrum gives the expansion velocity of the universe at the distance of IaSN, and the measured intensity of a IaSN gives a luminosity distance d_{L} using $F = \frac{L}{4\pi d_{\mathrm{L}}^2}$, where F is observed flux at the Earth and L is an intrinsic luminosity of a IaSN. On the other hand, the luminosity distance can be written with cosmological parameters as

$$d_{\mathrm{L}}(z) = \frac{1+z}{H_0} \int_0^z \left[\Omega_{\Lambda,0} + (1+z')^3 \Omega_{\mathrm{m},0} - (1+z')^2 \Omega_{\mathrm{k}} \right]^{-\frac{1}{2}} dz'. \tag{1.3}$$

From the equation above, cosmological parameters can be evaluated. Figure 1.1.5 shows observed IaSN luminosity (converted to magnitude m) as a function of the distance (shown in units of redshift z)[3]. From this figure, the model with $\Omega_{\mathrm{m}} = 0.25$, $\Omega_{\Lambda} = 0.75$ was found to be consistent to measurements.
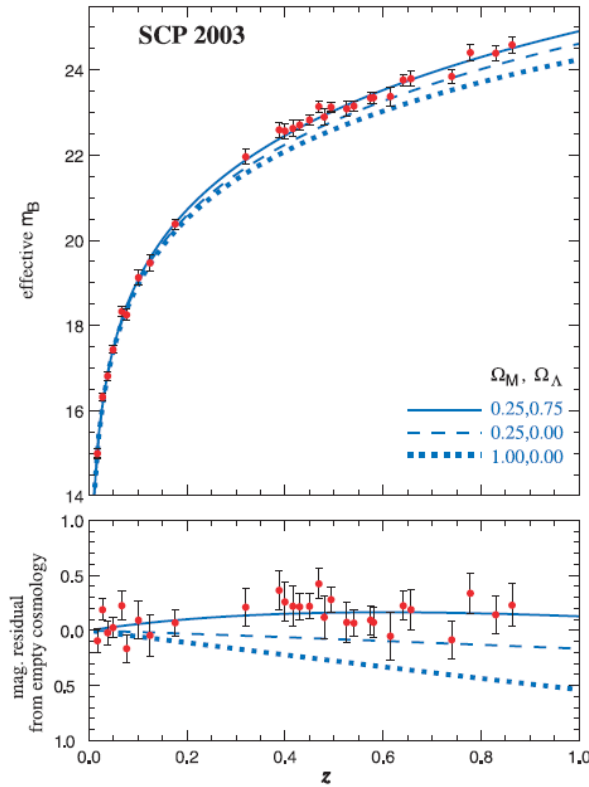
Figure 1.1.5: Observed IaSN luminosity (converted to magnitude m) as a function of the distance (shown in units of redshift z)[3] Red points are measured and blue lines are models. Bottom figure shows the residual from the model assuming $\Omega_{\mathrm{m}} = 0$, $\Omega_{\Lambda} = 0$. The model with $\Omega_{\mathrm{m}} = 0.25$, $\Omega_{\Lambda} = 0.75$ was found to be consistent to the measurements.

Cosmic Microwave Background (CMB) is the thermal radiation left from the Big Bang. In the early and high temperature universe, where electrons, protons and photons exist with thermal equilibrium, photons cannot move straight due to Compton scatterings with electrons. As the temperature decreased adiabatically with the universe expansion, electrons and protons formed atoms, and photons can go straight. This phenomenon is called recombination and the temperature of this time corresponds to the ionizing energy of a hydrogen atom which is $\sim 3000\,\mathrm{K}$. After the recombination, photon's wavelength increased according to the universe expansion. And now, we observe this remained photon as a microwave and its spectrum is consistent to a black body of $2.725\,\mathrm{K}$. Observed CMB is perfectly isotropic, but it has a little fluctuation in temperature. In order to study the fluctuations for various scales, the spatial distribution of the temperature $T(\theta, \phi)$ is obtained by fitting with spherical harmonics Y_{lm} using coefficients a_{lm} as

$$T(\theta, \phi) = \sum_{l=0}^{\infty} \sum_{m=-l}^{l} a_{lm} Y_{lm}(\theta, \phi), \tag{1.4}$$

$$C_l = \frac{1}{2l+1} \sum_{m=-l}^{l} |a_{lm}|^2.$$

Here C_l is called angular power spectrum and represents the amplitude of the fluctuation at the scale of l ($\sim \frac{180°}{l}$ in degree). C_0 is the monopole and corresponds to the average temperature, and C_1 is the dipole moment and corresponds to the motion of the earth. At the finer scale, fluctuations were induced by integrated Sachs-Wolfe effect (ISW) and have information of the recombination era ($z \sim 1100$). ISW is the wavelength shifting effect that causes red shift at higher density region and blue shift at lower one due to a density fluctuation which was drawn out a quantum fluctuation by inflation. Assuming the cosmological parameters, we can evaluate the angular power spectrum by developing the temperature fluctuation induced by ISW according to the Boltzmann equation. Planck satellite observed the cosmic microwave fluctuations all over the sky[1]. Observed fluctuation of CMB was quite tiny as $\sim 100\mu\mathrm{K}$. Figure 1.1.6 shows the angular power spectrum measured by Planck. Comparing the measurement to the model, cosmological parameters were evaluated as $\Omega_\mathrm{m} \simeq 0.3$, $\Omega_\Lambda \simeq 0.7$ as shown in Figure 1.1.4.

Baryon acoustic oscillations (BAO) is the fluctuation in the density of the visible baryonic matter of the universe, caused by acoustic waves which existed in the early universe. Now theoretical model of the structure formation of the cluster of galaxy, we can predict how to develop the density fluctuation from acoustic waves to visible galaxies. Cosmological parameters are estimated by comparing observed galaxies distribution to the calculated one. The density fluctuation is considered to be developed by the gravitational instability because gravity is
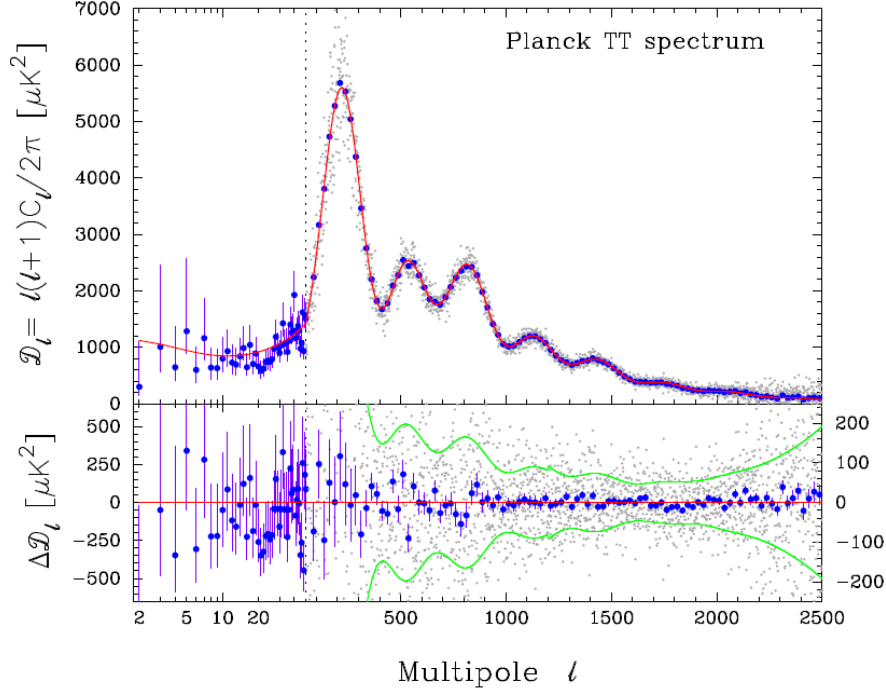
Figure 1.1.6: Angular power spectrum of CMB observed by Planck[1]. Blue points are measured data, red line is the best fit model. Bottom figure shows the residual from the best fit model.

unique long-range force in four fundamental forces in the universe. In order to turn out the density fluctuation, two types of dark matter were considered. One is the low mass dark matter, which velocity is relativistic (hot). This type of dark matter is called hot dark matter (HDM). The other is the massive dark matter, which is non-relativistic (cold). This type of dark matter is called cold dark matter (CDM). In case of HDM, a fine structure is disturbed by the motion of the dark matter. In this case, a scenario that large scale structure is formed in the first place then divide into clusters and galaxies, is favored (top-down scenario). But this top-down scenario is not supported because galaxies exist even at the early universe around $z \sim 6$. On the other hand, a bottom up scenario is favored in case of CDM and now this scenario is widely supported. Sloan Digital Sky Survey (SDSS) is the project surveying galaxies to investigate the distribution of galaxies[2]. In order to compare observations with the structure formation model, "two point correlation function" was used. Two point correlation function indicates the difference from the random distribution and defined as follows. Consider the probability $P(\mathbf{x}_1, \mathbf{x}_2)(dx_1)^3(dx_2)^3$ for galaxies contained to both of two volumes $(dx_1)^3(dx_2)^3$ around two points $\mathbf{x}_1, \mathbf{x}_2$ at a distance r. If the distribution of galaxies is perfectly at random, this probability is given as $\bar{n}^2(dx_1)^3(dx_2)^3$ using the number density of galaxies $\bar{n}$. But, the

12
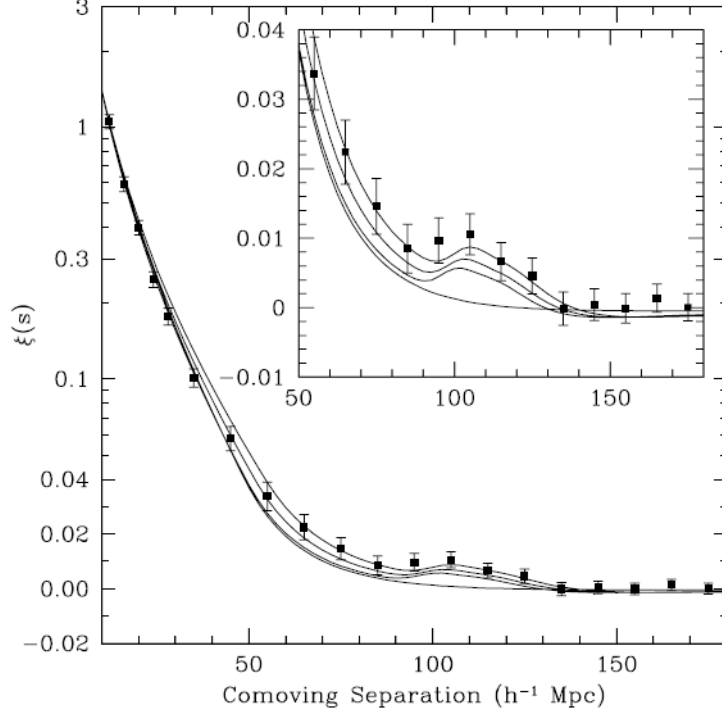
Figure 1.1.7: Measured two point correlation function of galaxies by SDSS[2]. Top, second and third lines show models assuming $\Omega_{\mathrm{m}}h^2 = 0.12$, 0.13 and 0.14, respectively, all with $\Omega_{\mathrm{b}}h^2 = 0.024$ and $n = 0.98$. The bottom line shows a pure CDM model assuming $\Omega_{\mathrm{b}}h^2 = 0$ and $\Omega_{\mathrm{m}}h^2 = 0.105$. Here, h is Hubble parameter normalized by 100 and n is number density of galaxy. Inset is the enlarged view.

actual probability differs from random as

$$P(\mathbf{x}_1, \mathbf{x}_2)d^3x_1 d^3x_2 = \bar{n}^2 \left[1 + \xi(r)\right](dx_1)^3(dx_2)^3 \tag{1.5}$$

and $\xi(r)$ is the two point correlation function. Figure 1.1.7 is measured two point correlation function of galaxies by SDSS. The peak around $\sim 100h^{-1}$Mpc is the indication of BAO and called an acoustic peak. The amplitude of an acoustic peak is sensitive to the gravitational components of the universe, and Ω_{m} is estimated by BAO as shown in Figure 1.1.4.

1.1.5 Big Bang nucleosynthesis

Big Bang Nucleosynthesis (BBN) describes the production of light nuclei besides hydrogen during the early universe. In 1940s, BBN was advocated by George Gamow to explain the ratio of elements in the universe, and after some discussions, the existence of CMB was predicted. Hence the discovery of CMB strongly supported BBN. Baryon density Ω_{b} is evaluated by BBN, and the dark matter density can be estimated as $\Omega_{\mathrm{DM}} = \Omega_{\mathrm{m}} - \Omega_{\mathrm{b}}$.

13

Production of heavier nuclei fusing nucleons needs a high temperature and high density environment, such an ultimate environment is realized only at Big Bang(if it happened), inner star, and Supernova. The fraction of elements in the universe is 75% hydrogen, 25% helium and the rest with other elements. Similar fractions are measured anywhere in the universe. The nuclei produced in inner stars or Super Novae are not only helium but also heavier elements. In order to explain the general abundance of light elements, BBN is inevitable.

At Big Bang, when the temperature and the density was high enough, protons and neutrons were at the equilibrium of weak interaction and they can convert to each other, where the ratio of protons to neutrons became 1 : 1. As the temperature and density became lower due to the universe expansion, the reaction velocity became slower than the expansion. When the temperature is below $\sim 1\,\mathrm{MeV}$, protons and neutrons are no longer in equilibrium. After that, neutrons one-sidedly decayed to protons, and the ratio of protons to neutrons became 4 : 1 at $\sim 100\,\mathrm{keV}$. At this temperature, the number of photons of which energy resolves deuterons $^2\mathrm{D}$ (binding energy of $^2\mathrm{D} = 2.22\,\mathrm{MeV}$) by photodegradation reaction was less than the number of $^2\mathrm{D}$. As a result, suppressed nuclear fusion came to be superior, and then nucleons fused to more stable nuclei. Since the binding energy of $^4\mathrm{He}$ ($28.3\,\mathrm{MeV}$) is much higher than that of $^2\mathrm{D}$, almost all the generated $^2\mathrm{D}$ fused to $^4\mathrm{He}$, and almost all the neutrons were fixed in $^4\mathrm{He}$. Also, $^7\mathrm{Li}$ and $^7\mathrm{Be}$ were slightly generated. As the universe expanding, the universe became too cold and too low in density to keep nuclear fusions and then the fraction of elements was fixed at this time. The fixed fraction is calculated by solving the Boltzmann equation and depends on the baryon-to-photon ratio.

The number of photons and baryons decrease equally during the universe expansion, and the baryon-to-photon ratio has been kept constant. Since the number density of photons is measured by CMB observations, the number density of baryons can be calculated using the baryon-to-photon ratio. Figure 1.1.8 shows the relation of elements fraction to the baryon-to-photon ratio. The baryon-to-photon ratios measured from observed number density of some light elements are almost consistent among these elements, and baryon density $\Omega_\mathrm{b}h^2 = 0.0214$ is obtained[9]. Considering normalized Hubble parameter $h = 0.71^{+0.04}_{-0.03}$, the baryon density is calculated as $\Omega_\mathrm{b} = 0.044 \pm 0.004$. Because this value is too small to explain the matter density $\Omega_\mathrm{m} \simeq 0.25$, the existence of non-baryon dark matter of the amount of $\Omega_\mathrm{DM} \simeq 0.20$ is supported.
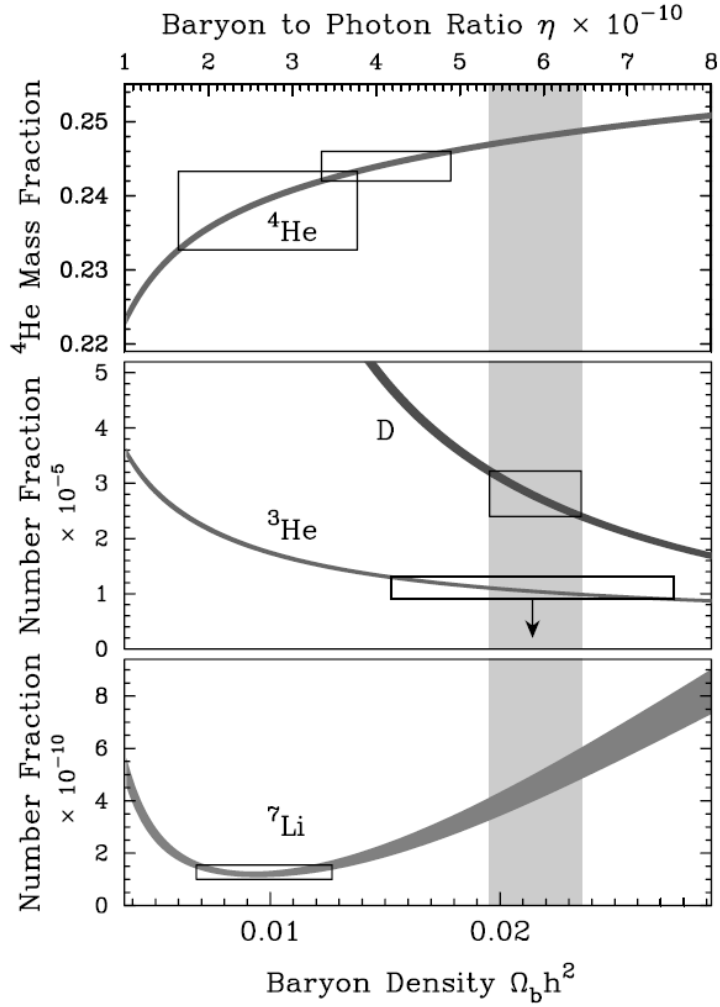
Figure 1.1.8: The relation of elements fraction to the baryon-to-photon ratio. Horizontal axis shows baryon-to-photon ratio and also written as baryon density. Vertical axis is elements fractions compared to hydrogen in the early universe. Four lines are the calculation of the standard BBN model (SBBN). The region surrounded by squares are the limit of number density from observation and corresponding baryon-to-photon ratio. Comparing the measurement to the calculation, $\Omega_b h^2 = 0.0214$ was obtained[9].

15

1.2 Particle physical dark matter : candidates

From astrophysical observations, the amount of non-baryonic dark matter was estimated to be $\Omega_{\mathrm{DM}} \simeq 0.20$. Also, the structure formation model (Section 1.1.4) strongly favors the CDM than HDM. In this section, the candidates of the dark matter are reviewed.

1.2.1 WIMP

In particle physics, the Standard Model (SM) theory is well accomplished and can explain physical phenomena at low energy scale ($\lesssim 1\,\mathrm{TeV}$). However, SM theory has several problems, and this theory is considered to be the low energy approximation of an ultimate unified theory. In this ultimate unified theory, the fundamental four interactions are considered to be unified at Planck energy scale ($\sim 10^{19}\,\mathrm{GeV}$). The existence of new theories describing the phenomena between SM energy scale and Planck scale is widely believed. Weakly Interacting Massive Particles (WIMPs) are predicted in some beyond-SMs, where the interaction must be weak and the mass is heavier than SM particles. WIMPs are good candidates of the dark matter from their nature, and strongly motivated by particle physics. There are several theories which produce WIMPs such as supersymmetry theory (SUSY), universal extra dimensions (UED), little Higgs theory (LHT), and so on. Particularly, SUSY is strongly preferred as a beyond-SM theory.

Supersymmetry theory (SUSY) is one of the these theories, which solves the hierarchy problem (the secondary divergence of Higgs mass). In addition, a unification of the coupling constants is realized as shown in Figure 1.2.1. This theory introduces new partner particles whose spins differ from those of SM particles by $1/2$ as listed in Table 1.2.1. The interaction of SUSY particles with SM particles are governed by the R-parity given as

$$R = (-1)^{3B+L+2S}, \tag{1.6}$$

where B, L and S are the baryon number, the lepton number and the spin, respectively. SM particles have odd R-parities, while SUSY particles have even R-parities. From the conservation of the R-parity, the lightest SUSY particle (LSP) must be stable because it cannot decay to SM particles without SUSY particles. LSP is the lightest gluino or chargino or neutralino, whose spins are $1/2$. If LSP is the lightest neutralino, the neutralino can be a candidate of the dark matter. Lightest neutralino ($\tilde{\chi}_1^0 \equiv \chi$) is the lightest linear combination of the photino ($\tilde{\gamma}$), the zino ($\tilde{Z}$) and the higgsinos ($\tilde{H}_1, \tilde{H}_2$). The photino and zino are expressed with the
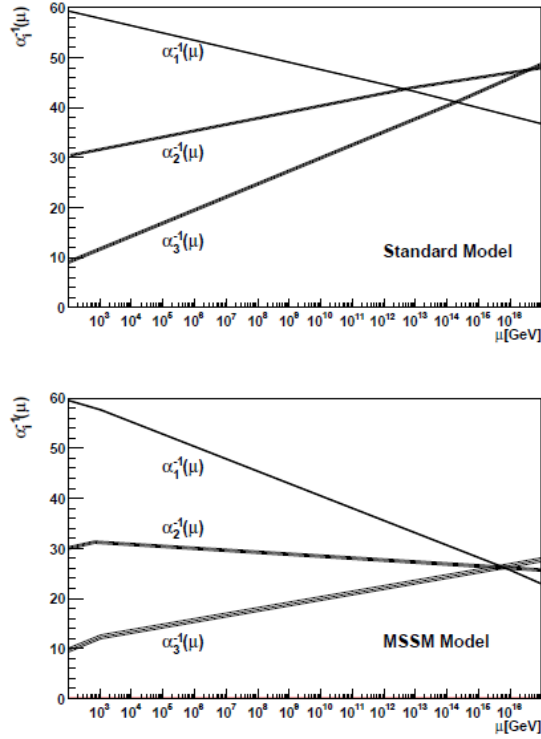
Figure 1.2.1: The relation of the coupling constants and energy in the standard model (SM) (top) and in the minimum supersymmetric standard model (SMMS) (bottom).α_1,α_2 and α_3 are the $U(1)$, $U(2)$ and $U(3)$ couplings, respectively.

superpartners of gauge bosons, the bino ($\tilde{B}$) and the wino ($\tilde{W}_3$) as

$$\begin{aligned} \tilde{\gamma} &= \cos\theta_W \tilde{B} + \sin\theta_W \tilde{W}_3 \tilde{Z} \\ &= -\sin\theta_W \tilde{B} + \cos\theta_W \tilde{W}_3. \end{aligned}$$

Thus, lightest neutralino χ is written as

$$\chi = a_1 \tilde{B} + a_2 \tilde{W}_3 + a_3 \tilde{H}_1 + a_4 \tilde{H}_2. \tag{1.7}$$

The lightest SUSY particle (LSP) is stable and satisfies the nature of dark matter if LSP is uncharged [10]. The method of neutralino search and the neutralino search experiments are explained in Chapter 2 and Chapter 3.

Universal Extra Dimension (UED) is one of the theories to provide WIMP other than SUSY. UED is the beyond SM theory to unify the gravity interaction and the electromagnetic interaction. UED argues that the universe consists of five or more dimensions. In the low energy limit (energy scale of SM), the universe is observed as four dimensions. UED requires

17

SM particles			SUSY particles		
Symbol	Name	Spin	Symbol	Name	Spin
$q = u, c, t$	up quarks	1/2	$\tilde{q}_u^1, \cdots \tilde{q}_u^6$	up squarks	0
$q = d, s, b$	down quarks	1/2	$\tilde{q}_d^1, \cdots \tilde{q}_d^6$	down squarks	0
$l = e, \mu, \tau$	leptons	1/2	$\tilde{l}_6, \cdots \tilde{l}_6$	sleptons	0
ν_e, ν_μ, ν_τ	neutrinos	1/2	$\tilde{\nu}_1, \tilde{\nu}_2, \tilde{\nu}_3$	sneutrinos	0
g	gluons	1	$\tilde{g}$	gluinos	1/2
$W^\pm$	W bosons	1	$\tilde{\chi}_1^\pm, \tilde{\chi}_2^\pm$	charginos	1/2
$H^\pm$	charged Higgs	0			
γ	photon	1	$\tilde{\chi}_1^0, \cdots \tilde{\chi}_4^0$	neutralinos	1/2
Z^0	Z boson	1			
h^0	light scalar Higgs	0			
H^0	heavy scalar Higgs	0			
A^0	pseudoscalar Higgs	0			

Table 1.2.1: SUSY particles

the Kaluza-Klein particles which conserve the K-K-parity. The lightest Kaluza-Klein particle (LKP) is thus stable and can be a candidate of the dark matter[11].

Little Higgs theory (LHT) is one of the beyond-SM theories which naturally explains the electroweak symmetry breaking. LHT requires a global symmetry at $\sim 10\text{TeV}$ scale and is broken at $\sim$ TeV scale to cancel the second divergence of Higgs mass correction in the first loop. In this theory, new particles named T-partner and T-parity are introduced. SM particles have positive T-parity, and T-partners have negative T-parity in contrast. The lightest T-partner (LTP) is stable due to the conservation of the T-parity, and one of the candidates of the dark matter[12].

1.2.2 Axion

Axion was introduced as a new neutral light pseudo-scalar boson in order to solve the CP violation problem of the strong interaction[13]. The mass of the axion is limited to $1\,\mu\text{eV} - 1\,\text{meV}$ or $2\,\text{eV} - 5\,\text{eV}$ by the evolution of a star, observations of the neutrinos from supernova explosions, cosmology and so on. A lighter mass region remains as the window for the cold dark matter[14]. In spite of the light mass, axion is considered as a candidate of the dark matter because axions were produced at the phase transition of a vacuum around inflation era and axions were not in the thermal equilibrium with other particles at the early universe.

Axions are widely searched for by the detection of photons generated by the Primakoff effect,

which is the conversion from an axion to a photon in a strong magnetic field[15]. Figure 1.2.2 shows the results of axion searches in the lighter mass region. No positive signal has been obtained and the limit of the axion-photon coupling for each mass of axion is settled[16].
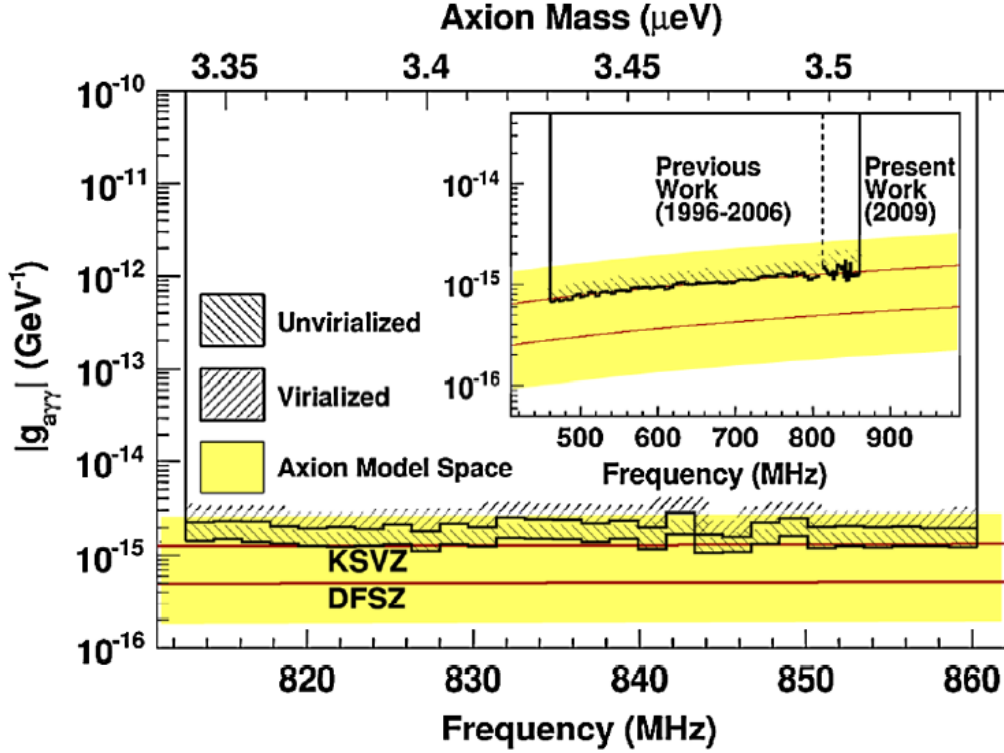
Figure 1.2.2: 90%C.L. limit of the axion-photon coupling for each mass of axion [16].

1.2.3 Q-ball

Baryon asymmetry problem is based on the fact that the amount of the antimatter is much less than that of the matter in the universe. Affleck-Dine mechanism is one of the models to generate this baryon asymmetry. Though Affleck-Dine mechanism does not match well with SM, Affleck-Dine mechanism can work well with SUSY[17]. Affleck-Dine mechanism with SUSY naturally contains the non-topological soliton called "Q-ball", and Q-ball can be the dark matter.

Q-ball is a single particle including a lot of squarks and sleptons. Since the mass per baryon number is less than the mass of proton, the Q-ball can stably exist. Baryon number of a Q-ball is $\sim 10^{24}$ and the mass is $\sim 1\,\mathrm{mg}$ in spite of a single particle. The Q-ball interacts with nucleus through the strong interaction, and emits two or three pions of $\sim 100\,\mathrm{GeV}$. Because of

19

the quite large mass, a kinetic energy of a Q-ball is so high compared to the energy loss that a Q-ball goes straight interacting with matters. Though the estimated cross section of this interaction, 100 mb, is much larger than those of other candidates of dark matter, a Q-ball can be a candidate of dark matter because of the quite low number density in the universe.

In order to detect the Q-ball, we need to detect several pions with $\sim 100\,\mathrm{GeV}$ emitted in a straight line. Water Cerenkov detectors (BAKSAN, Kamiokande) or high energy cosmic ray detectors such as telescope arrays (TA) are suitable to search for the Q-balls. Figure 1.2.3 shows the results of the Q-ball searches. Severe limits are obtained but the perfect scenario that explains both the baryon density and the dark matter density has not been denied yet.
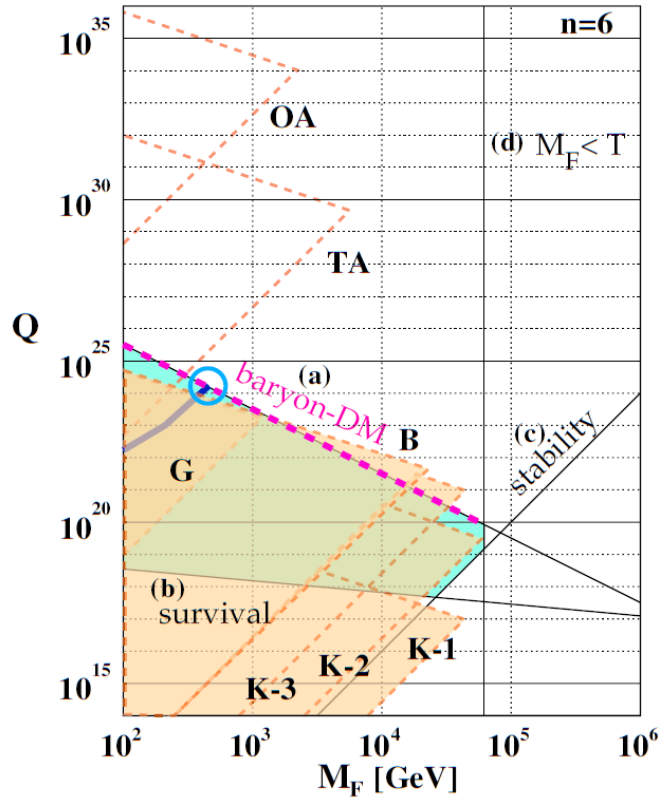
Figure 1.2.3: The limit of the baryon number Q of Q-ball for the breaking scale of SUSY M_{F} [17]. The light blue region surrounded by (a-d) lines is the area where the Q-ball allowed to exist as the dark matter. Particularly, all of the dark matter is explained by Q-ball along the pink dotted lines. The blue line is the ideal region that the baryon density reaches to the observations, and the light blue circle is the best scenario. The regions labeled B, G, K-1,2,3 are the obtained limit by BAKSAN, Gyrlyand and Kamiokande, respectively. The regions labeled TA and OA is the estimated limit by Telescope Array project and OWL-AIRWATCH, respectively.

1.2.4 Sterile neutrino

By the experimental studies on neutrino oscillation in these a few decades, it is established that there are three kind of neutrinos ν_e, ν_μ and ν_τ, and they are mixed with themselves. Now, the fourth neutrino named sterile neutrino is proposed as the final state of neutrino mixing to explain the result of LSND experiment[18]. In addition, by assuming sterile neutrino, the pulsar kick phenomenon of neutron stars cal also be explained[19]. Unlike other ordinal neutrinos, the sterile neutrino does not interact via the weak interaction. Mass of the sterile neutrino is estimated as $1 \sim 30 \, \text{keV}$. Then, sterile neutrino can be a candidate of dark matter.

Although the life time of the sterile neutrino is longer than the age of the universe, sterile neutrino is considered to decay to X-rays. The sterile neutrino search using X-ray space observatories are performed and the result are shown in Figure 1.2.4. No X-ray signal originated from sterile neutrinos has been observed and the limit of the mixing angle for each mass is obtained.
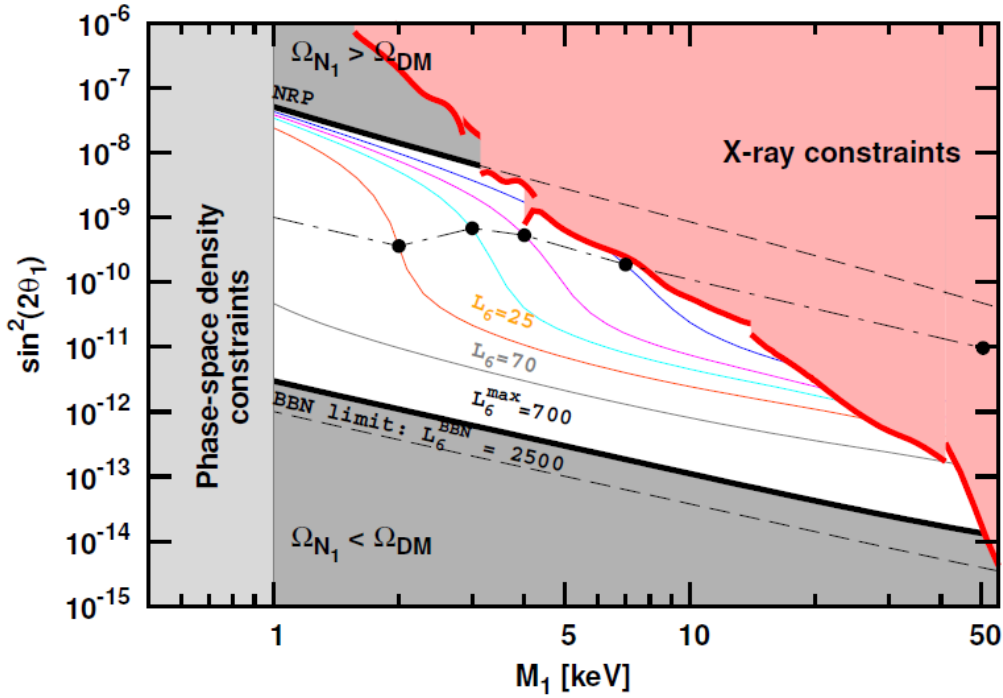
Figure 1.2.4: Obtained limits of the mixing angle θ_1 as a function of sterile neutrino mass M_1[18]. The red region is the constraint region by X-ray observations. The gray region is the constraint the sterile neutrino dark matter.

1.2.5 Other candidates

In addition to the candidates described above, there are a variety of dark matter candidates such as mirror matter[20], asymmetric dark matter[21], crypton[22], and so on. Please see the references for details.

1.3 WIMP search

There are three types of WIMP searches; direct searches (underground experiments), indirect searches (astrophysical observations) and collider experiments (production). As shown in Figure 1.3.1, Feynman diagram of these WIMP searches are same in principle with the difference in the time evolution. Direct search seeks for the WIMP-nucleus elastic scatterings, and is expected to provide direct evidences of the dark matter. Indirect searches are to find the evidence of the WIMPs by detecting gamma-ray, neutrinos and anti-particles emitted from the annihilations of WIMPs. Collider experiment aims to produce WIMPs directly by the collision of accelerated particles. These three methods are complementary to the others.
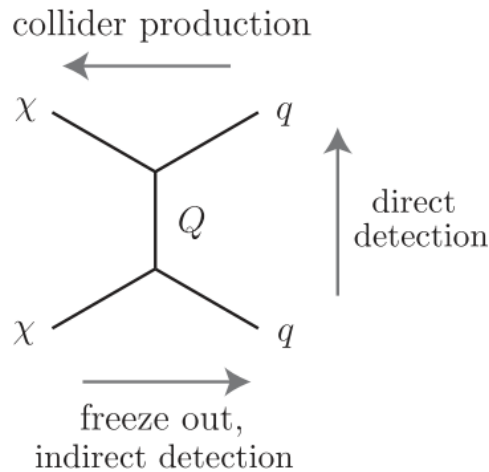
Figure 1.3.1: Feynman diagram contributing to, direct searches, indirect search, and collider production of dark matter[23]. Here, χ, q and Q represent nenutralino, SM particle and a force-mediating boson, respectively.

1.3.1 Direct search

Direct search pursues for WIMP-nucleus elastic scatterings, where the WIMPs in the halo of our galaxy are expected to be detected by the detector on the Earth. Direct search can

provide the direct evidence of the existence of the halo dark matter. However, expected event rate is very low because the cross section of a WIMP interacting with an ordinal matter is very small. Therefore these experiments need to be performed in underground facilities. At present, a lot of direct search experiments are performed around the world. More information on direct detection is in the next chapter; the method of direct detection is mentioned in Chapter 2 and direct detection experiments is reviewed in Chapter 3.

1.3.2 Indirect search

Neutralino is considered to be a majorana particle, whose antiparticle is its particle itself. Then neutralinos can annihilate with themselves[11]. The annihilation rate Γ_{ann} depends on the number density n_χ, annihilation cross section σ_{ann} and a velocity v as

$$\Gamma_{\mathrm{ann}} \propto n_\chi^2 < \sigma_{\mathrm{ann}}(v)v > . \tag{1.8}$$

At the high-gravitational-field region, such as the center of a galaxy, the Sun or the Earth, annihilations of trapped neutralinos would constantly occur. The detection of the annihilation products, gamma-rays, neutrinos and antiparticles from specific locations would provide indirect evidences of the neutralino.

Gamma-rays are generated by neutralino annihilation through process such as $\chi\chi \longrightarrow \gamma\gamma$ and $\chi\chi \longrightarrow Z^0\gamma$. The observable gamma-ray spectrum would consist of a peak corresponding to the energy of neutralino mass and a continuous component of decayed gamma-rays of produced hadrons and leptons. Since the annihilation rate depends on the SUSY parameters ($\sigma_{\mathrm{ann}}(v)$ and branching ratio) and the halo density profile (n_χ and v), the estimation of a flux and an energy spectrum is difficult. But gamma-rays from neutralino annihilation are expected to be a radiation located in high density regions such as the center of the galaxy, and the time dependence is constant. Energetic gamma ray experiment telescope (EGRET) was a gamma-ray telescope on the CGRO satellite to observe $30\,\mathrm{MeV} - 30\,\mathrm{GeV}$ gamma-rays. From the observation of the galactic plane, about 60% higher gamma-ray flux than the model calculation was detected above $1\,\mathrm{GeV}$ region[24]. This excess was found to be within the systematic uncertainty and thus a clear discovery was not achieved with EGRET. Fermi satellite is a gamma-ray telescope to observe $30\,\mathrm{MeV} - 300\,\mathrm{GeV}$ gamma-rays, with 30 times better sensitivity of EGRET. An excess around $130\,\mathrm{GeV}$ in the energy spectrum was observed at the galactic plane and galactic center with a local statistical significance 4.5σ as in Figure 1.3.2[25]. This peak might be explained that the excess originates from the dark matter annihilations. From calculated reduced χ^2 value, $130\,\mathrm{GeV}$ dark matter with $2\mathrm{DM} \to 2\gamma$ can fit the data. This result is one indication of existence of a particle-physical dark matter.
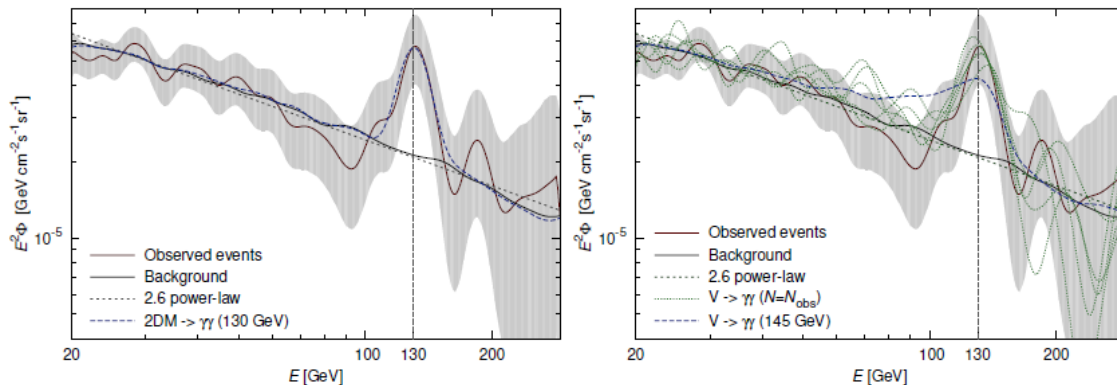
Figure 1.3.2: Energy spectrum of gamma-rays from the center of our galaxy measured by Fermi (red solid line). Gray region is 95%C.L. error band. Black dashed line is the best fit model assuming dark matter annihilation. Left and right figures are fitted with the $2DM \rightarrow 2\gamma$ channel model and $2DM \rightarrow 2V \rightarrow 4\gamma$ channel model, respectively, where V is light hypothetical finals states. Best-fit mass are $130\,\text{GeV}$ and $145\,\text{GeV}$ for left and right figure. respectively.

Neutrinos can be produced as a final state of the annihilation of neutralinos. The energy of neutrino from the neutralino annihilation is about $1/2 \sim 1/3$ of a neutralino mass. Unlike gamma-rays, the interaction of neutrino is very rare. Therefore, annihilations of neutralinos trapped in the Earth and the Sun are observed using a neutrino probe where we cannot search by gamma-rays. Since the Sun mostly consists of hydrogen, neutralino would be trapped by SD interactions (Section 2.2). Thus, the observation of neutrinos from the Sun is sensitive to spin-dependent cross section. On the other hand, since the Earth contains atoms of the large mass number, observation of neutrinos from the Earth is sensitive to SI cross section. Super-Kamiokande (SK), constructed in the Kamioka mine, is a water-Cherenkov neutrino detector with ~ 50000 ton of water surrounded by ~ 10000 of photomultipliers. The observation of neutrinos from the Sun did not show any significant excess, and the limit of SD cross section was settled[26]. Another Cherenkov neutrino detector, IceCube, has ~ 5000 of photo multipliers in the ice at the South Pole. Observations of neutrinos from the Sun and the galactic center have been performed[27].

Neutralino annihilation also products particle-antiparticle pairs. It is considered that antiparticles in nearby universe is created by the cosmic ray spallation. Thus an excess of antiparticle in the cosmic ray maybe an indirect evidence of the dark matter. Since antiparticles have charges, incoming direction cannot be observed. Thus, indirect detection by searching antiparticle is difficult to discriminate a dark matter model from other model clearly. PAMELA (a Payload for Antimatter Matter Exploration and Light-nuclei Astrophysics)[28] and AMS (Alpha Magnetic Spectrometer)[29] are cosmic ray observation experiments which can distinguish

antiparticles from normal particles by using magnetic field. PAMELA, operated from 2006 to 2009, measured positron fraction $N_{e^+}/(N_{e^-} + N_{e^+})$ and found the excess from $\sim 10\,\mathrm{GeV}$ to $100\,\mathrm{GeV}$ (detector's limit) energy region. AMS-02, on the International Space Station from 2011, obtained a consistent result with a higher precision. Both results are shown in Figure 1.3.3. The excess can be explained by the annihilation of the dark matter and also by nearby pulsars. Further observations are required to understand the origin of the excess.
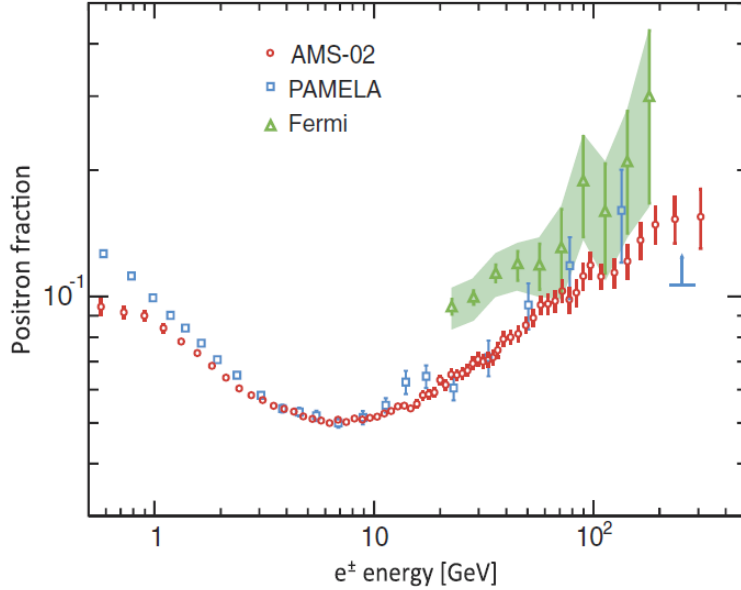
Figure 1.3.3: positron fraction $N_{e^+}/(N_{e^-} + N_{e^+})$ in the cosmic-ray measured by AMS-02, PAMELA and Fermi.

1.3.3 Collider experiment

An accelerator with a sufficiently energy has a possibility to product SUSY particles. Produced SUSY particles would immediately decay to the lightest SUSY particle (LSP). If LSP is neutralino, it is detected as a missing momentum and a missing energy. In addition, the mass and cross section of neutralino can be estimated by measuring the event rate, the missing momentum and the missing energy. Though accelerator experiments cannot argue that the neutralino is the astrophysical dark matter or not, a discovery of the neutralino and investigations of its nature is important for other dark matter searches.

Large electron-positron collider (LEP) and LEP2 is circular accelerators colliding electrons and positrons, and the operation have already been completed. The maximum center-of-mass energy of LEP2 is $200\,\mathrm{GeV}$. LEP2 did not discover the candidate event of neutralino and

obtained a lower limit of the neutralino mass as $M_D > 40\,\text{GeV}$ [30]. Large hadron collider (LHC) is a circular accelerator colliding protons, started in September 2008. The designed maximum center-of-mass energy is 14 TeV. By 2013, LHC has been operated at the energy of 8 TeV, and obtained no signal of neutralinos[31]. By 2015, LHC will be upgraded to be operated at the energy of 13 to 14 TeV. International linear collider (ILC) is a linear accelerator colliding electrons and positrons, and is at a planning stage. Since the interaction of leptons is more simple than that of hadrons, the background rate of a lepton collider is low. Thus, a lepton collider is suitable to measure more precise parameters of a neutralino. The maximum energy achieved with circular accelerators is limited by synchrotron radiation. ICL will overcome this problem by using a linear accelerator, and is expected to measure detail parameters of the neutralino[32].

Chapter 2

Method of Direct Dark Matter Search

Direct detection pursues for the detection via WIMP-nucleus elastic scatterings. Direct detection can provide the direct evidence of the existence of the dark matter in the halo of our galaxy. In this section, the theoretical framework of the direct detection focusing on the expected signal is reviewed[33].

2.1 Energy spectrum

Direct detection method is to detect the energy deposition on the nucleus via WIMP-nucleus elastic scatterings, and thus the calculation of the expected energy spectrum is the first step to estimate the signals. Because we are on the Earth, the relative velocity between the Earth and the halo of our galaxy affects the expected energy spectrum. The solar system rotates in our galaxy at a distance of $8\,\mathrm{kpc}$ from the center of the galaxy, and the Earth rotates around the Sun. Then, the velocity of the Earth relative to the galactic halo is written as

$$
\begin{aligned}
v_{\mathrm{E}}(=|\mathbf{v}_{\mathrm{E}}|) &= v_{\mathrm{sun}} + v_{\mathrm{orb}}\cos\theta_{\mathrm{orb}}\sin 2\pi y \\
&\simeq 244 + 15\sin(2\pi y)\,[\mathrm{km/sec}],
\end{aligned}
\tag{2.1}
$$

where v_{sun} is the velocity of the Sun relative to the galactic halo, v_{orb} is the orbital rotation velocity of the Earth around the Sun, θ_{orb} is the inclination of the Earth orbital plane with respect to the galactic plane and y is the time in year from March 2nd. Figure 2.1.1 shows the schematic view of the motion of the Sun and the Earth in our galaxy. Due to the rotation of the Earth around the Sun, the relative velocity of the Earth to our galaxy become the maximum in June and the minimum in December.

27
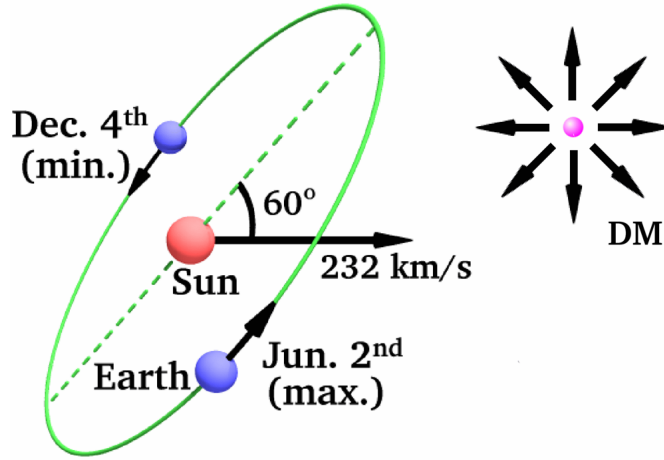
Figure 2.1.1: The schematic view of the motion of the Sun and the Earth in our galaxy.

The number density of WIMPs, dn, with the velocity of $v \sim v + dv$ is written as

$$dn = \frac{n_0}{k} f(\mathbf{v}, \mathbf{v}_\mathrm{E}) d^3 v, \tag{2.2}$$

$$n_0 \equiv \int_0^{v_\mathrm{esc}} dn, \qquad k = \int_0^{2\pi} d\phi \int_{-1}^{+1} d(\cos\theta) \int_0^{v_\mathrm{esc}} f(\mathbf{v}, \mathbf{v}_\mathrm{E}) v^2 dv,$$

where k is the normalize constant, n_0 is the total number of WIMPs in our galaxy, v_esc is the escape velocity of the galaxy, θ is the angle between $\mathbf{v}_\mathrm{E}$ and WIMP velocity, and ϕ is azimuth angle taking WIMP velocity vector as a zenith. Assuming a Boltzmann distribution, the velocity distribution of the dark matter $f(\mathbf{v}, \mathbf{v}_\mathrm{E})$ is written as

$$f(\mathbf{v}, \mathbf{v}_\mathrm{E}) = e^{-(\mathbf{v}+\mathbf{v}_\mathrm{E})^2/v_0^2}, \tag{2.3}$$

where v_0 is the velocity dispersion of our galaxy and if the galaxy rotation velocity is flat, it becomes rotation velocity. The normalize constant k is derived in case v_esc is infinite or not as

$$k = k_0 = (\pi v_0^2)^{3/2} \qquad\qquad (v_\mathrm{esc} = \infty) \tag{2.4}$$

$$k = k_1 = k_0 \left\{ \mathrm{erf}\left(\frac{v_\mathrm{esc}}{v_0}\right) - \frac{2}{\pi^{1/2}} \frac{v_\mathrm{esc}}{v_0} e^{-v_\mathrm{esc}^2/v_0^2} \right\} \quad (v_\mathrm{esc} \neq \infty), \tag{2.5}$$

where $\mathrm{erf}(x) \equiv \frac{2}{\pi^{1/2}} \int_0^x e^{-t^2} dt$ is the error function.

The differential event rate R per target mass per days is

$$dR = \frac{N_\mathrm{A}}{A} \sigma v dn, \tag{2.6}$$

where N_A is the Avogadro number (6.02×10^{26}), A is the mass number of the target nucleus, $v = |\mathbf{v} - \mathbf{v}_\mathrm{E}|$ is the dark matter velocity relative to the target, σ is the WIMP-nucleus cross section.

Strictly, σ depends on the momentum transfer. In this section, we discuss the cross section with zero momentum transfer σ_0. The cross section taking account of the momentum transfer will be discussed in the latter section 2.3. The total event rate R is derived by integrating Equation (2.6) as

$$R = \frac{N_0}{A}\sigma_0 \int v \, dn \tag{2.7}$$

The total event rate R_0 for $v_E = 0$ and $v_{esc} = \infty$ is described as

$$R_0 = \frac{2}{\pi^{1/2}} \frac{N_A}{A} \frac{\rho_D}{M_D} \sigma_0 v_0 \tag{2.8}$$

$$= \frac{361}{M_D M_N} \left(\frac{\sigma_0}{1\,\mathrm{pb}}\right) \left(\frac{\rho_D}{0.3\,\mathrm{GeV/c^2/cm^3}}\right) \left(\frac{v_0}{220\,\mathrm{km/s}}\right), \tag{2.9}$$

where ρ_D is the mass density of the dark matter, M_D is the mass of the dark matter, $M_N (= 0.932A)$ is the mass of the target nucleus. The Equation (2.9) is normalized by $\sigma_0 = 1\,\mathrm{pb}$, $v_0 = 220\,\mathrm{km/s}$, $\rho_D = 0.3\,\mathrm{GeV/c^2/cm^3}$.

The recoil energy E_R of the nucleus with a mass M_N caused by an elastic scattering of the dark matter with the kinematic energy $E \left(= \frac{1}{2}M_D v^2\right)$ in the laboratory system is

$$E_R = Er\left(1 - \cos\theta\right)/2, \tag{2.10}$$

$$r = \frac{4M_D M_N}{(M_D + M_N)^2}, \tag{2.11}$$

where θ is the scattering angle in the center of mass system, r is the reduced mass. Assuming the scattering is isotropic in the center of mass system, $\cos\theta$ distribution become flat and E_R also becomes flat in the $0 \leq E_R \leq Er$ region. Then the energy spectrum $\frac{dR}{dE_R}$ is written as

$$\frac{dR}{dE_R} = \int_{E_{min}}^{E_{max}} \frac{1}{Er} dR(E)$$

$$= \frac{1}{E_0 r} \int_{v_{min}}^{v_{max}} \frac{v_0^2}{v^2} dR(v),$$

where $E_{min} = E_R/r$ is the minimum kinetic energy of WIMP capable to give the energy E_R to a target nuclei, E_{max} is the maximum kinetic energy of WIMP in a laboratory system, E_0 is defined as $E_0 = \frac{1}{2}M_D v_0^2 = \frac{v_0^2}{v^2}E$. The energy spectrum is obtained using Equation (2.6), (2.2), and (2.3) as

$$\frac{dR}{dE_R} = \frac{R_0}{E_0 r} \frac{k_0}{k} \int_{v_{min}}^{v_{max}} \frac{1}{v} f(\mathbf{v}, \mathbf{v}_E) d^3 v. \tag{2.12}$$

By performing the integration of Equation (2.12), the specific formula of energy spectra are

obtained as

$$\frac{dR(0, \infty)}{dE_{\mathrm{R}}} = \frac{R_0}{E_0 r} e^{-E_{\mathrm{R}}/E_0 r}, \tag{2.13}$$

$$\frac{dR(0, v_{\mathrm{esc}})}{dE_{\mathrm{R}}} = \frac{k_0}{k_1} \left[\frac{dR(0, \infty)}{dE_{\mathrm{R}}} e^{-E_{\mathrm{R}}/E_0 r} - \frac{R_0}{E_0 r} e^{-v_{\mathrm{esc}}^2/v_0^2} \right], \tag{2.14}$$

$$\frac{dR(v_{\mathrm{E}}, \infty)}{dE_{\mathrm{R}}} = \frac{R_0}{E_0 r} \frac{\pi^{1/2}}{4} \frac{v_0}{v_{\mathrm{E}}} \left[\mathrm{erf} \left(\frac{v_{\mathrm{min}} + v_{\mathrm{E}}}{v_0} \right) - \mathrm{erf} \left(\frac{v_{\mathrm{min}} - v_{\mathrm{E}}}{v_0} \right) \right], \tag{2.15}$$

$$\frac{dR(v_{\mathrm{E}}, v_{\mathrm{esc}})}{dE_{\mathrm{R}}} = \frac{k_0}{k_1} \left[\frac{dR(v_{\mathrm{E}}, \infty)}{dE_{\mathrm{R}}} - \frac{R_0}{E_0 r} e^{-v_{\mathrm{esc}}^2/v_0^2} \right]. \tag{2.16}$$

Figure 2.1.2 shows the normalized energy spectrum.
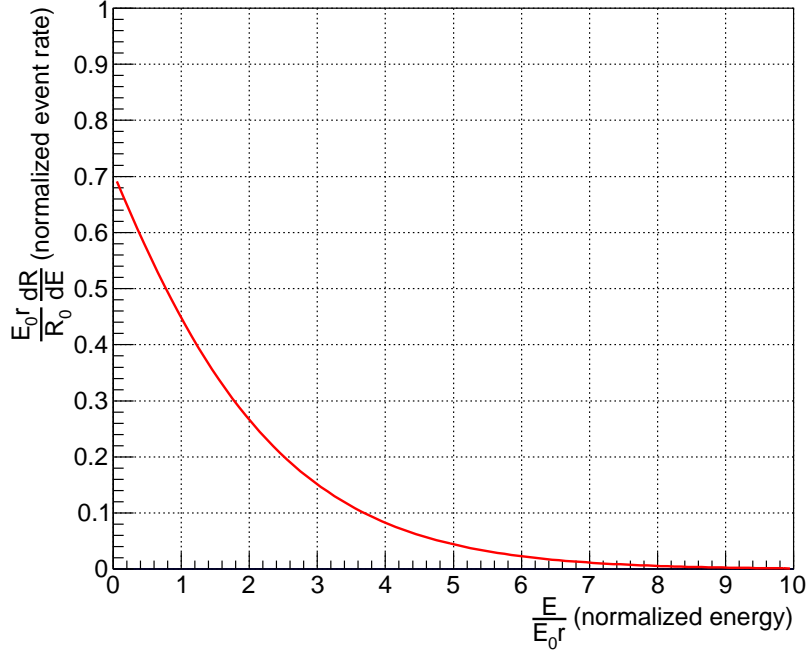
Figure 2.1.2: The normalized energy spectrum of nucleus caused by an elastic scattering of the WIMP. ^{19}F is assumed for the target.

2.2   Cross section

In the previous section, the total rate R_0 was shown to be proportional to the WIMP-nucleus cross section. The cross section can be calculated by assuming certain sets of parameters in the MSSM model [10, 34, 35]. In this subsection, the elastic scattering cross section of SUSY neutralino and nucleus is discussed.

30

2.2.1 Lagrangian

The MSSM Lagrangian framework leads to the following low-energy effective Lagrangian, $\mathcal{L}_{\text{eff}}$, which is suitable for describing elastic neutralino-quark interactions[34].

$$
\begin{aligned}
\mathcal{L}_{\text{eff}} & = \bar{\chi}\gamma^\mu\gamma^5\chi\bar{q}_i\gamma_\mu\left(\alpha_{1i}+\alpha_{2i}\gamma^5\right)q_i & (2.17)\\
& + \alpha_{3i}\bar{\chi}\chi\bar{q}_i q_i \\
& + \alpha_{4i}\bar{\chi}\gamma^5\chi\bar{q}_i\gamma^5 q_i \\
& + \alpha_{5i}\bar{\chi}\chi\bar{q}_i\gamma^5 q_i \\
& + \alpha_{6i}\bar{\chi}\gamma^5\chi\bar{q}_i q_i,
\end{aligned}
$$

where χ and q denote neutralino and quarks. The Lagrangian should be summed over quark generations, and the subscript i refers to up-type $i=1$ and down-type $i=2$ quarks. The terms with coefficients α_{1i}, α_{4i}, α_{5i} and α_{6i} depend on the velocity and are suppressed because the velocity is non-relativistic in an elastic neutralino-quark scattering. Coefficients α_{2i} and α_{3i} contribute to the Spin-Independent(SI) and Spin-Dependent(SD) interactions, respectively, and Feynman diagrams of each interaction are shown in Figure 2.2.1.

2.2.2 Spin Independent (SI) cross section

The cross section of SI interaction is written as

$$
\sigma_{\chi-\text{N}}^{\text{SI}} = \frac{4\mu_{\chi-\text{N}}^2}{\pi}\left[Zf_{\text{p}}+(A-Z)f_{\text{n}}\right]^2, \tag{2.18}
$$

where Z and A are the atomic number and mass number of a target, respectively. $\mu_{\chi-\text{N}}$ is the reduced mass of the neutralino mass M_{D} and a target mass M_{N},

$$
\mu_{\chi-\text{N}} = \frac{M_{\text{D}}M_{\text{N}}}{M_{\text{D}}+M_{\text{N}}}. \tag{2.19}
$$

f_p and f_n are proton-neutralino and neutron-neutralino SI couplings, respectively. They are written as the sum of the neutralino-quarks SI couplings, $f_{T_q}^{(\text{p})}$ and $f_{T_q}^{(\text{n})}$ as

$$
\frac{f_{\text{p}}}{M_{\text{p}}} = \sum_{q=\text{u,d,s}} f_{T_q}^{(\text{p})}\frac{\alpha_{3q}}{M_q} + \frac{2}{27}f_{\text{TG}}^{(\text{p})}\sum_{q=\text{c,t,b}}\frac{\alpha_{3q}}{M_q} \tag{2.20}
$$

$$
\frac{f_{\text{n}}}{M_{\text{n}}} = \sum_{q=\text{u,d,s}} f_{T_q}^{(\text{n})}\frac{\alpha_{3q}}{M_q} + \frac{2}{27}f_{\text{TG}}^{(\text{n})}\sum_{q=\text{c,t,b}}\frac{\alpha_{3q}}{M_q}, \tag{2.21}
$$

where M_{p}, M_{n} and M_q are the mass of the proton, the neutron and quarks, respectively. The numerical value of the $f_{T_q}^{(\text{p})}$, $f_{T_q}^{(\text{n})}$, $f_{\text{TG}}^{(\text{p})}$ and $f_{\text{TG}}^{(\text{n})}$ are calculated from the mass of quarks and
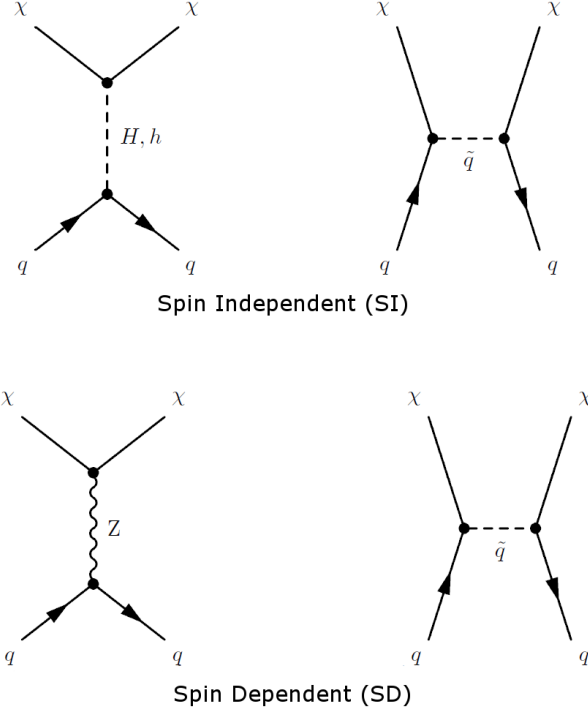
Figure 2.2.1: Feynman diagrams of neutralino-quark elastic scattering. Upper set is SI and lower set is SD, respectively.

chiral symmetry applied to baryons, as

$$f_{T_u}^{(p)} = 0.020 \pm 0.004, \ f_{T_d}^{(p)} = 0.026 \pm 0.005, \ f_{T_s}^{(p)} = 0.118 \pm 0.062,$$
$$f_{T_u}^{(n)} = 0.014 \pm 0.003, \ f_{T_d}^{(n)} = 0.036 \pm 0.008, \ f_{T_s}^{(n)} = 0.118 \pm 0.062,$$
$$f_{TG}^{(p)} = 1 - \sum_{q=u,d,s} f_{T_q}^{(p)},$$
$$f_{TG}^{(n)} = 1 - \sum_{q=u,d,s} f_{T_q}^{(n)}.$$

In most of the cases, $f_{T_q}^{(p)} \simeq f_{T_q}^{(n)}$, therefore $\sigma_{\chi-N}^{SI} \propto \mu_{\chi-N}^2 A^2$ is practically derived. Thus, the cross section of SI interaction is written by using neutralino-proton SI cross section; $\sigma_{\chi-p}^{SI}$,

$$\sigma_{\chi-N}^{SI} = \sigma_{\chi-p}^{SI} \frac{\mu_{\chi-N}^2}{\mu_{\chi-p}^2} A^2. \tag{2.22}$$

Equation 2.22 indicates that a target element with large A is effective for SI-interacting neutralinos. Figure 2.2.2 shows the SI cross sections normalized by neutralino-proton SI cross section for some target nucleus.

32
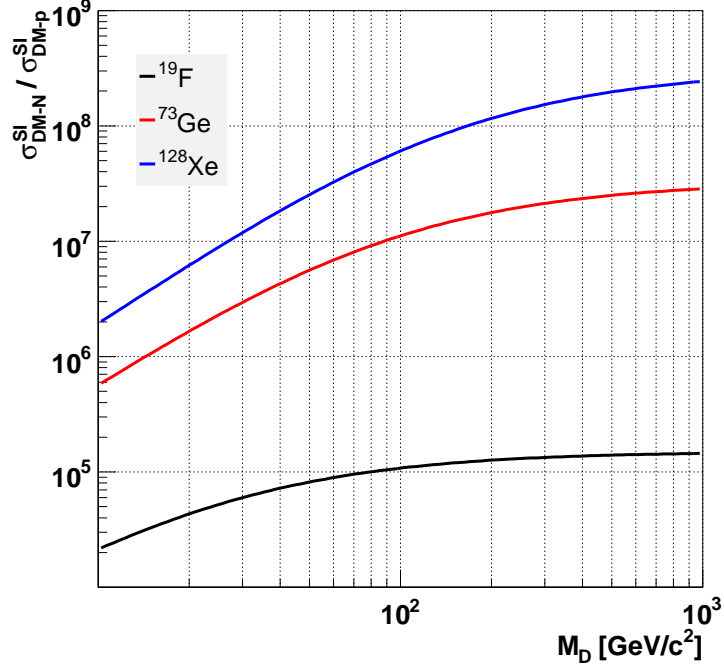
Figure 2.2.2: SI cross sections normalized by neutralino-proton SI cross section, $\sigma_{\chi-N}^{\mathrm{SI}}/\sigma_{\chi-p}^{\mathrm{SI}}$ as a function of neutralino mass. Black, red and blue line shows target difference as $^{19}\mathrm{F}$, $^{73}\mathrm{Ge}$ and $^{128}\mathrm{Xe}$.

2.2.3 Spin Dependent (SD) cross section

The cross section of SD interaction is written as

$$\sigma_{\chi-N}^{\mathrm{SD}} = \frac{32}{\pi} G_{\mathrm{F}}^2 \mu_{\chi-N}^2 \Big(a_{\mathrm{p}} \langle S_{\mathrm{p}} \rangle + a_{\mathrm{n}} \langle S_{\mathrm{n}} \rangle \Big)^2 \frac{J+1}{J}, \tag{2.23}$$

where $G_{\mathrm{F}}(= 1.166 \times 10^{-5}\,\mathrm{GeV}^{-2}(\hbar c)^3)$ is the Fermi coupling constant, $\langle S_{\mathrm{p}} \rangle$ and $\langle S_{\mathrm{n}} \rangle$ are expectation values of spin of proton and neutron in the nucleus, J is the total spin of the nucleus. a_{p} and a_{n} consist of the sum of quark components as

$$a_{\mathrm{p}} = \sum_{q=\mathrm{u,d,s}} \frac{\alpha_{2q}}{\sqrt{2}G_{\mathrm{F}}} \Delta_q^{(\mathrm{p})}, \tag{2.24}$$

$$a_{\mathrm{n}} = \sum_{q=\mathrm{u,d,s}} \frac{\alpha_{2q}}{\sqrt{2}G_{\mathrm{F}}} \Delta_q^{(\mathrm{n})}, \tag{2.25}$$

where $\Delta_q^{(\mathrm{p})}$ and $\Delta_q^{(\mathrm{n})}$ are the quark spin contents of the nucleon, and are calculated [34] as

$$\Delta_{\mathrm{u}}^{(\mathrm{p})} = \Delta_{\mathrm{d}}^{(\mathrm{n})} = 0.78 \pm 0.02,$$
$$\Delta_{\mathrm{d}}^{(\mathrm{p})} = \Delta_{\mathrm{u}}^{(\mathrm{n})} = -0.48 \pm 0.02,$$
$$\Delta_{\mathrm{s}}^{(\mathrm{p})} = \Delta_{\mathrm{s}}^{(\mathrm{n})} = -0.15 \pm 0.02.$$

33

Using Lande factor $\Lambda = \frac{a_{\rm p}\langle S_{\rm p}\rangle + a_{\rm n}\langle S_{\rm n}\rangle}{J}$, the cross section of SD interaction is written as

$$\sigma_{\chi-{\rm N}}^{\rm SD} = \frac{32}{\pi}G_{\rm F}^2\mu_{\chi-{\rm N}}^2\Lambda^2 J(J+1). \tag{2.26}$$

The spin-dependent interaction can only occur for nuclei with nonzero spin. Only nuclei with an odd number of either protons or neutrons can have nonzero spin. As for such nuclei, Λ is approximated using $S_{\rm odd}$ determined from measured magnetic momentum $\mu_{\rm mag}$, as

$$\Lambda \approx \frac{a_{\rm odd}S_{\rm odd}}{J},$$

$$S_{\rm odd} \approx \frac{\mu_{\rm mag} - g_{\rm odd}^l J}{g_{\rm odd}^s - g_{\rm odd}^l},$$

where subscript "odd" refers an unpaired nucleon; p(proton) or n(neutron). $g_{\rm odd}^l$ and $g_{\rm odd}^s$ are the orbital and spin nucleon g-factor; $g_{\rm p}^l = 1$, $g_{\rm n}^l = 0$, $g_{\rm p}^s = 5.586$ and $g_{\rm n}^s = -3.826$. The list of the spin J, measured $\mu_{\rm mag}$ and the calculated $\Lambda^2 J(J+1)/a_{\rm odd}(\equiv \lambda^2 J(J+1))$ are in Table 2.2.1 for some target nucleus. For experimental use, the SD cross section is written using $\sigma_{\chi-{\rm p}}^{\rm SD}$ as

$$\sigma_{\chi-{\rm N}}^{\rm SD} = \sigma_{\chi-{\rm p}}^{\rm SD}\frac{\mu_{\chi-{\rm N}}^2}{\mu_{\chi-{\rm p}}^2}\frac{\lambda^2 J(J+1)}{0.75}. \tag{2.27}$$

Values of $\sigma_{\chi-{\rm N}}^{\rm SD}/\sigma_{\chi-{\rm p}}^{\rm SD}$ and $\sigma_{\chi-{\rm N}}^{\rm SD}/\sigma_{\chi-{\rm n}}^{\rm SD}$ for some target nucleus are shown in Figure 2.2.3 and Figure 2.2.4, respectively.

Isotope	J	Abundance(%)	$\mu_{\rm mag}$	$\lambda^2 J(J+1)$	unpaired nucleon
^{1}H	1/2	100	2.793	0.750	proton
^{7}Li	3/2	92.5	3.256	0.244	proton
^{11}B	3/2	80.1	2.689	0.112	proton
^{15}N	1/2	0.4	-0.283	0.087	proton
^{19}F	1/2	100	2.629	0.647	proton
^{23}Na	3/2	100	2.218	0.041	proton
^{127}I	5/2	100	2.813	0.007	proton
^{133}Cs	7/2	100	2.582	0.052	proton
^{3}He	1/2	1.0×10^{-4}	-2.128	0.928	neutron
^{17}O	5/2	0.0	-1.890	0.342	neutron
^{29}Si	1/2	4.7	-0.555	0.063	neutron
^{73}Ge	9/2	7.8	-0.879	0.065	neutron
^{129}Xe	1/2	26.4	-0.778	0.124	neutron
^{131}Xe	3/2	21.2	0.692	0.055	neutron
^{183}W	1/2	14.3	0.118	0.003	neutron

Table 2.2.1: The spin J, measured $\mu_{\rm mag}$ and the calculated $\lambda^2 J(J+1)$ for some target nucleus.
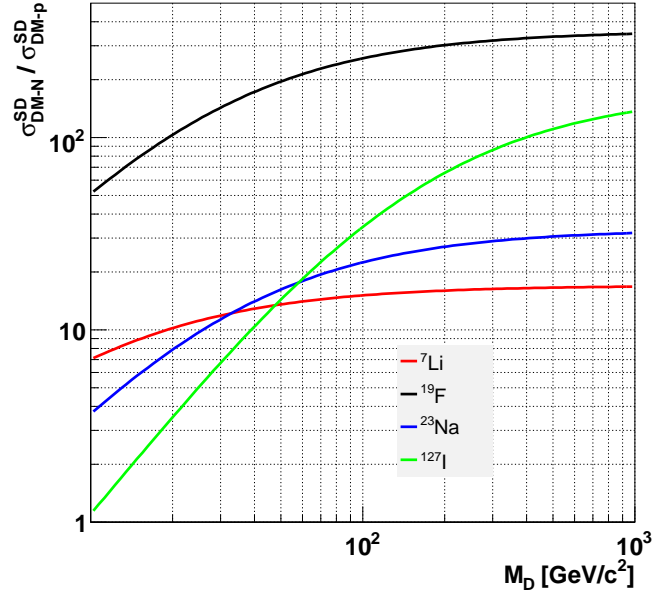
Figure 2.2.3: $\sigma^{\text{SD}}_{\chi-\text{N}}/\sigma^{\text{SD}}_{\chi-\text{p}}$ as a function of neutralino mass. Red, black, blue and green line shows target isotope difference as ^{7}Li, ^{19}F, ^{23}Na and ^{127}I, respectively.
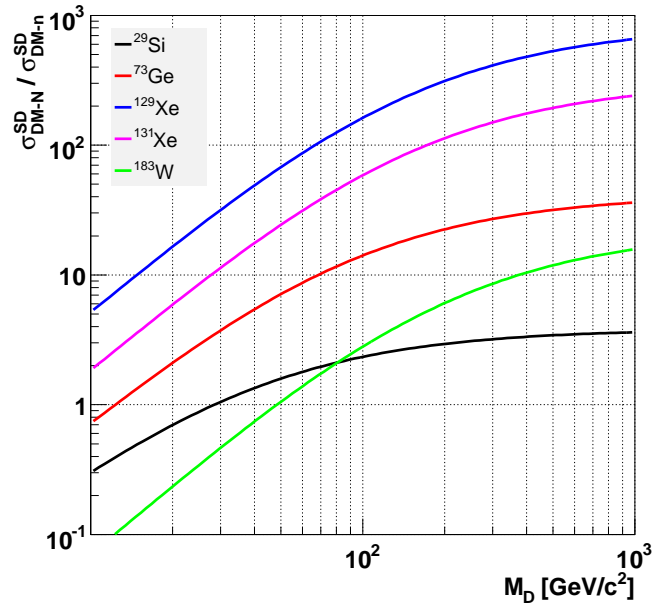
Figure 2.2.4: $\sigma^{\text{SD}}_{\chi-\text{N}}/\sigma^{\text{SD}}_{\chi-\text{n}}$ as a function of neutralino mass. Black, red, blue, pink, green line shows target isotope difference as ^{29}Si, ^{73}Ge, ^{129}Xe, ^{131}Xe and ^{183}W, respectively.

2.3 Form factor

When the de Broglie wavelength h/q with the momentum transfer q is no longer large compared to the nuclear radius, where h is the Planck constant and $q = \sqrt{2M_N E_R}$ is the momentum of the recoil nuclei for a recoil energy of E_R. The effective cross section begins to fall for large q cases. This effect is referred to as a "form factor", F, F is a function of the dimensionless quantity, qr_n, where r_n is an effective nuclear radius. The effective neutralino-nucleus cross section is corrected with this form factor as

$$\sigma(qr_n) = \sigma_0 F^2(qr_n),\tag{2.28}$$

where σ_0 is the cross section at a zero momentum transfer. In the first Born (plane wave) approximation, the form factor is given by Fourier transformation of the density distribution of the 'scattering centres', $\rho(r)$, as

$$
\begin{aligned}
F(qr_n) &= \int \rho(r) exp(i\mathbf{q} \cdot \mathbf{r})\mathbf{dr} \\
&= \frac{4\pi}{q} \int_0^\infty r\sin(qr)\rho(r)dr.
\end{aligned}
$$

For the SI interaction, since neutralino would interact with any of the nucleon, the nuclei can be approximated as a solid sphere. In this case, the form factor is written using Bessel function $j_i(x) = (\sin(x) - x\cos(x))/x^2$ as

$$F(qr_n) = 3\frac{j_1(qr_n)}{qr_n}\exp\left(-\frac{(qs)^2}{2}\right),\tag{2.29}$$

where $r_n \simeq 1.14A^{1/3}$ fm, and $s \simeq 0.9$ fm representing the nuclear skin thickness. Figure 2.3.1 shows the SI form factors of some isotopes as a function of the recoil energy E_R. Expected energy spectra of SI interaction with ^{19}F target is shown in Figure 2.3.2, where the form factor is taken into account.

For the SD interaction, since neutralino would interact with the surplus nucleon, the nuclei can be approximated as a thin shell, and this assumption is called the odd-group model. In this case, the form factor is written using Bessel function $j_0 = \sin(x)/x$ as

$$F(qr_n) = j_0(qr_n),\tag{2.30}$$

where $r_n \simeq 1.0A^{1/3}$ fm. Figure 2.3.3 shows the SD form factors of some isotopes as a function of the recoil energy E_R. Expected energy spectra of SD interaction with ^{19}F target is shown in Figure 2.3.4, where the form factor is taken into account.
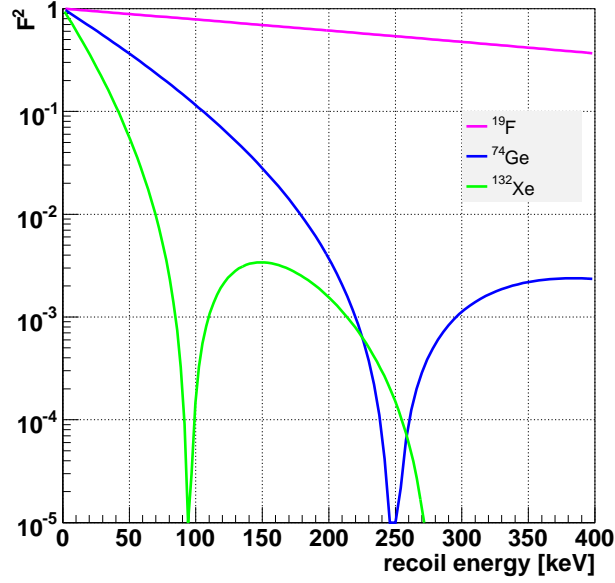
Figure 2.3.1: The SI form factors of some isotopes as a function of the recoil energy E_{R}. Pink, blue and green lines show target isotopes of ^{19}F, ^{74}Ge and ^{132}Xe, respectively.
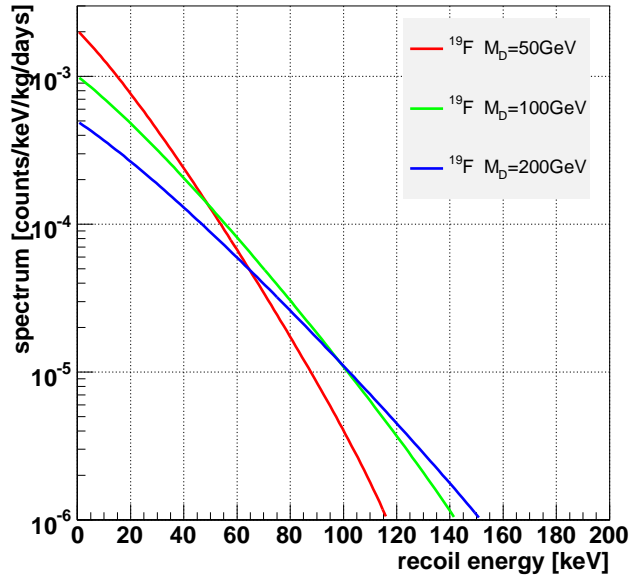
Figure 2.3.2: The expected energy spectra of SI interaction with ^{19}F target, where $\sigma^{\mathrm{SI}}_{\chi-\mathrm{p}} = 10^{-6}$ pb is assumed. Red, green and blue lines show the cases for the neutralino mass of $M_{\mathrm{D}} = 50$, 100 and $200\,\mathrm{GeV/c^2}$, respectively.
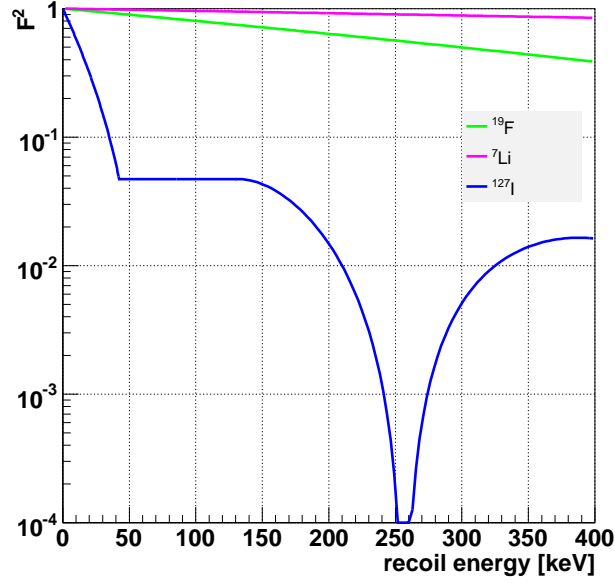
Figure 2.3.3: The SD form factors of some isotopes as a function of the recoil energy E_R. Green, pink and blue lines show target isotopes of ^{7}Li, ^{19}F and ^{127}I, respectively.
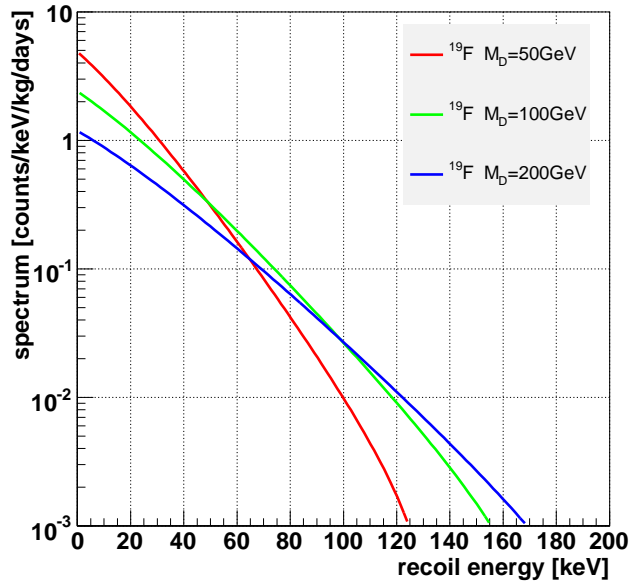
Figure 2.3.4: The expected energy spectra of SD interaction with ^{19}F target, where $\sigma^{\mathrm{SD}}_{\chi-\mathrm{p}} = 1\,\mathrm{pb}$ is assumed. Red, green and blue lines show the cases for the neutralino mass of $M_\mathrm{D} = 50$, 100 and $200\,\mathrm{GeV/c^2}$, respectively.

2.4 Dark matter signal

We need to observe a distinct signature in order to claim a clear detection of the dark matter because the expected spectrum itself has featureless exponential shape as shown in Figure 2.3.2 and Figure 2.3.4. Distinct signatures can be caused by the nuclear-dependence of the neutralino-necleus reactions, the relative motion of Solar system to the galactic halo, and that of the Earth to the galactic halo. They can be observed as the signatures listed below.

- Nuclear target dependence of the event rate

- Annual modulation of the event rate and the shape of the spectrum

- Directional dependence of the event rate

These signals are discussed in the following subsections.

2.4.1 Nuclear target dependence

The shape of the expected energy spectrum dR/dE_{R} depends on the isotopes for the following reasons. First, the mass number A affects the reduced mass as Equation (2.11), thus the expected event rate becomes high for the target mass close to the assumed neutralino mass. Second, the mass number and the reduced mass affect the SI cross section as Equation (2.22), thus the expected event rate becomes higher for larger mass number isotopes. Third, the $\lambda^2 J(J+1)$ term and the reduced mass affect the SD cross section as Equation (2.27), thus some isotopes with the large $\lambda^2 J(J+1)$ term, such as ^{19}F, ^{3}He and so on, have large SD cross sections. Fourth, the mass number A affects the form factor as Equation (2.29) and Equation (2.30), thus the effective cross section become small for large mass number isotopes. Figure 2.4.1 and Figure 2.4.2 are the expected energy spectra dR/dE_{R} of various targets for the SI-interacting and the SD-interacting neutralino, respectively. Here $M_{\mathrm{D}} = 100\,\mathrm{GeV}/c^2$, $\sigma^{\mathrm{SI}}_{\chi-\mathrm{p}} = 1 \times 10^{-6}\,\mathrm{pb}$ and $\sigma^{\mathrm{SD}}_{\chi-\mathrm{p}} = 1\,\mathrm{pb}$ are assumed. From Figure 2.4.1 and Figure 2.4.2, it can be judged that the difference of the event rate between isotopes can be a distinct signal of dark matter. It should be noted, however, the background also depends on the isotopes, thus it is difficult to claim a dark matter detection strongly by using only this signal.

2.4.2 Annual modulation

The annual modulation of the event rate is caused by the Earth's motion around the Sun as described in Equation (2.1). The velocity of the Earth relative to our galaxy, v_{E},
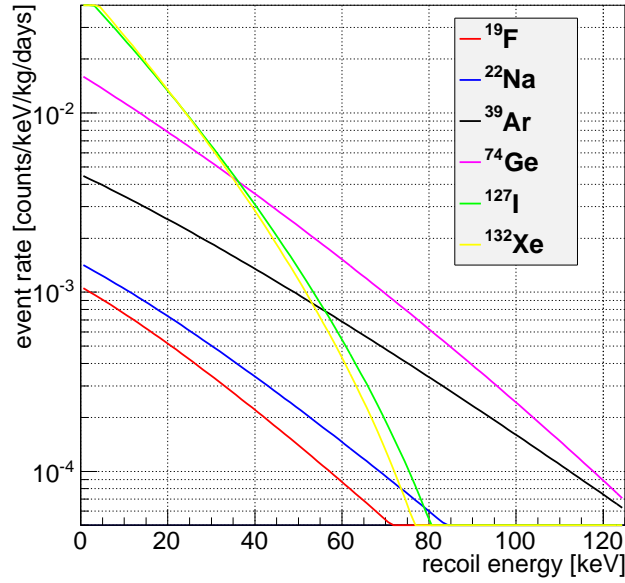
Figure 2.4.1: The expected energy spectrum dR/dE_{R} of various targets for the SI-interacting neutralino with a mass of $M_{\mathrm{D}} = 100\,\mathrm{GeV}/c^2$ and $\sigma_{\chi-\mathrm{p}}^{\mathrm{SI}} = 1 \times 10^{-6}\,\mathrm{pb}$.
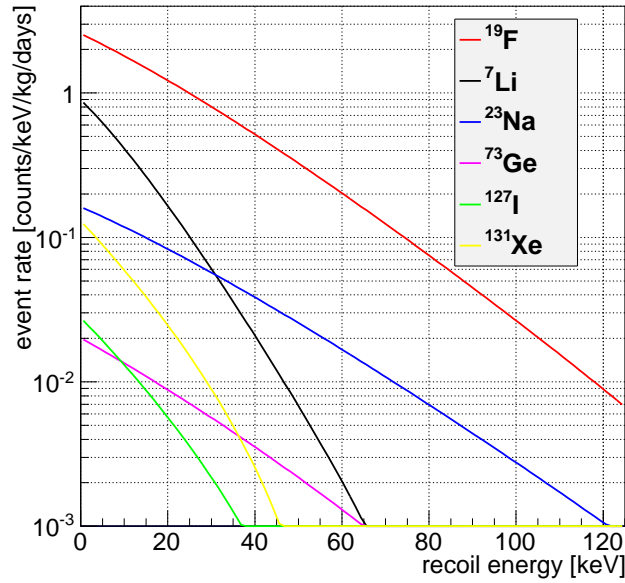
Figure 2.4.2: The expected energy spectrum dR/dE_{R} of various targets for the SD-interacting neutralino with a mass of $M_{\mathrm{D}} = 100\,\mathrm{GeV}/c^2$ and $\sigma_{\chi-\mathrm{p}}^{\mathrm{SD}} = 1\,\mathrm{pb}$.

become maximum in June 2nd and minimum in December 4th, and the order of modulation size is less than $O(v_{\mathrm{orb}}/v_{\mathrm{sun}}) \sim 5\%$. Figure 2.4.3 illustrates the expected modulation of the energy spectrum between June and December, where the target is ^{19}F for the SD interaction, $M_{\mathrm{D}} = 100\,\mathrm{GeV}$, and $\sigma^{\mathrm{SD}}_{\chi-\mathrm{p}} = 1\,\mathrm{pb}$. In order to detect such a tiny annual modulation, we need to take large statistics using a large mass detector such as solid or liquid detector. The experimental result of annual modulation will be discussed in section 3.1.1.
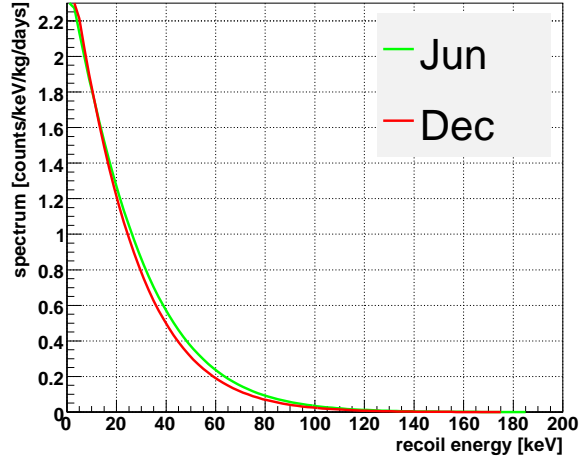
Figure 2.4.3: The expected modulation of energy spectrum between June and December, where the target is ^{19}F for the SD interaction, $M_{\mathrm{D}} = 100\,\mathrm{GeV}$, $\sigma^{\mathrm{SD}}_{\chi-\mathrm{p}} = 1\,\mathrm{pb}$.

2.4.3 Directionality

The most convincing signal of the dark matter would be seen in the directional distribution of the recoil nucleus. Since the Cygnus constellation is seen in the forward direction of the Solar system's motion, dark matters would seem to be coming from the Cygnus direction like "WIMP-wind". Since the Cygnus direction is varying per hour and per day, the systematic error due to the daily and seasonal environmental changes will be canceled.

In the laboratory system, expected angular spectrum of recoil nucleus is written as

$$\frac{d^2 R}{dE_{\mathrm{R}} d\cos\theta} \simeq \frac{1}{2} \frac{R_0}{E_0 r} \exp\left[-\frac{(v_{\mathrm{E}} \cos\theta - v_{\mathrm{min}})^2}{v_0^2} \right], \tag{2.31}$$

where angle θ is formed by the WIMP-wind direction and the recoil nuclei direction[36]. Figure 2.4.4 shows the expected angle-energy distribution, where the target is ^{19}F for the SD interaction, $M_{\mathrm{D}} = 100\,\mathrm{GeV}$, and $\sigma^{\mathrm{SD}}_{\chi-\mathrm{p}} = 1\,\mathrm{pb}$. Figure 2.4.5 shows the expected $\cos\theta$ distribution obtained by selecting the events with recoil energy of $100 - 120\,\mathrm{keV}$ in Figure 2.4.4.

41

Since an isotropic background makes flat $\cos\theta$ distribution, asymmetric $\cos\theta$ distribution in Figure 2.4.5 can be a strong evidence of the dark matter detection.
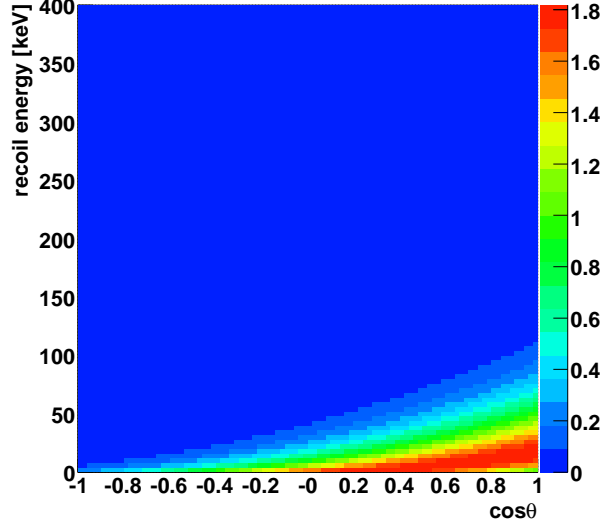
Figure 2.4.4: The expected angle-energy distribution, where the target is ^{19}F for the SD interaction, $M_{\mathrm{D}} = 100\,\mathrm{GeV}$, $\sigma^{\mathrm{SD}}_{\chi-\mathrm{p}} = 1\,\mathrm{pb}$, θ is the angle formed by the WIMP-wind direction and recoil nuclei direction. The color bar represent the event rate with an unit of [count/keV/kg/days/ $\cos\theta$].
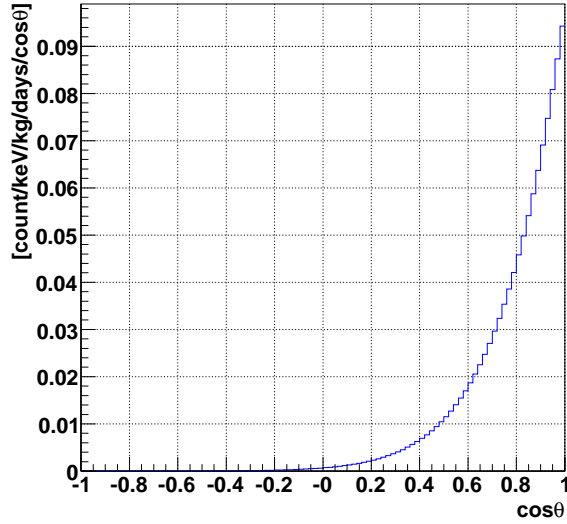
Figure 2.4.5: The expected $\cos\theta$ distribution $(100 - 120\,\mathrm{keV})$, where the target is ^{19}F for the SD interaction, $M_{\mathrm{D}} = 100\,\mathrm{GeV}$, $\sigma^{\mathrm{SD}}_{\chi-\mathrm{p}} = 1\,\mathrm{pb}$, θ is the angle formed by the WIMP-wind direction and the recoil nuclei direction.

Chapter 3

Review of Direct Dark Matter Search

A number of experiments have been carried out to detect WIMPs by observing neutralino-nucleus elastic scatterings. In direct search experiments, detectors are designed to detect recoil energy of typically less than $100\,\mathrm{keV}$ via photons, phonons or charges. In general, direct dark matter detectors should have following three characteristics.

- **Low energy threshold**
  The shape of the expected energy spectrum is exponential-like (Section 2.1). Then, the threshold energy is lower, the more signal is expected. A relevant energy region is considered to be below $100\,\mathrm{keV}$.

- **Large mass**
  Since the direct detection of the dark matter is a rare event search, a large target mass is required to accumulate sufficient statistics in a reasonable observation time. Typical required mass is from kilogram to ton for annual modulation detection method.

- **Low background**
  Typical techniques of low radioisotope background such as a material selection and shielding are important to WIMP detectors. Basically, the detector is settled in the underground laboratories to reduce the background induced by cosmic-rays. In addition, particle identifications using adittional signals are useful to discriminate backgrounds.

Direct dark matter search experiments are roughly categorized into two types in terms of the signals obtained; the conventional type and the direction-sensitive type. Whereas a conventional detector measures only the energy of the nuclear recoil, a direction-sensitive type

also obtains the directional information of nuclear recoil track which can provide a strong evidence of the dark matter detection (Section 2.4.3). A gaseous detector with high position resolution is required the direction-sensitive search in order to detect a short track less than 1 mm in atmospheric pressure gas. Almost all groups in the direct dark matter search field adopt "conventional method" which needs large mass detectors. On-going direct search experiments are listed in Table 3.0.1. Direct detection experiments are reviewed in this chapter.

Experiments	Detector (material)	signal	ref
Conventional type			
DAMA/LIBRA	Solid scintillator (NaI(Tl))	photon	[37, 38, 39, 40]
NAIAD	Solid scintillator (NaI(Tl))	photon	[41]
KIMS	Solid scintillator (CsI(Tl))	photon	[42]
DAMA/LXe	Liquid scintillator (Xe)	photon	[43]
XMASS	Liquid scintillator (Xe)	photon	[44]
XENON100	Liquid scintillator (Xe)	photon, charge	[45, 46]
LUX	Liquid scintillator (Xe)	photon, charge	[47]
WARP	Liquid scintillator (Ar)	photon, charge	[48]
CDMS	Bolometer (Si,Ge)	phonon, charge	[49]
CoGeNT	Bolometer (Ge)	phonon, charge	[50]
CRESST	Bolometer (CaWO$_4$)	phonon, photon	[51]
DAMIC	CCD (Si)	charge	[52]
COUPP	Bubble chamber (CF$_3$I)	charge	[53]
SIMPLE	Bubble chamber (C$_2$ClF$_5$)	charge	[54]
PICASSO	Bubble chamber (C$_4$F$_{10}$)	charge	[55]
Direction-sensitive type			
DRIFT	Gasous TPC (CS$_2$)	charge	[56]
DM-TPC	Gasous TPC (CF$_4$)	charge	[57]
NEWAGE	Gasous TPC (CF$_4$)	charge	[58]
MIMAC	Gasous TPC (CF$_4$)	charge	[59]
NIT-group	Emulsion (AgBr, C,N,O)	charge	[60]
DNA-group	DNA Tracking Chamber (Au)	charge	[61]

Table 3.0.1: Direct dark matter search experiments.

3.1 Conventional experiment

Almost all direct dark matter search experiments use solid or liquid detectors to obtain a large target mass. The recoil energy is converted to photon, heat and ionization. From the difference of the signals, the detectors are categorized as follows; solid scintillators and liquid noble gas scintillators for detecting only the photon, liquid noble gas scintillators for

detecting the photon and ionization, semiconductor bolometers for detecting the ionization and heat, crystal bolometers for detecting photon and heat, bubble chambers for detecting the ionization. The results are summarized in Figure 3.1.1. Details on the conventional detector experiments are described in the following subsections.

3.1.1   Solid scintillator

Scintillators have advantages in constructing large mass detectors and well-studied their properties. Many types of scintillators, such as NaI(Tl), CsI(Tl), have been used for dark matter searches.

DAMA group conducted a dark matter search with a highly radio-pure 100 kg NaI(Tl) setup for seven years and claimed to have detected an annual modulation signature due to the dark matter[40]. Allowed parameter regions of WIMPs are shown as enclosed regions in Figure 3.1.1. They also reported new results from another seven years observation with a highly radio-pure 250 kg NaI(Tl) setup (DAMA/LIBRA), which reproduced the DAMA annual modulation signature as shown in Figure 3.1.2[37]. The DAMA/LIBRA experiment accumulated the largest exposure (1.17 ton $\cdot$ year) and claimed a positive signature of the dark matter. However, there is also the opinion that this annual modulation signal is arised from systematic error due to a seasonal fluctuating background becacuse several experiments have obtained lower cross section limits. Experiments using NaI in other sites[62, 63] are one method to confirm the DAMA's signal. In addition, a direction-sensitive experiment can provide a distinct signal of dark matter without seasonal systematic error.

Other experiments using solid scintillators have been carried out. NAIAD[41] using 55 kg of NaI(Tl) accumulated a 44.9 kg $\cdot$ year of exposure showed a sensitivity comparable to DAMA without positive results. CaF$_2$ scintillators do not show a good rejection power by the pulse shaping cut, while they have a potential advantage to the SD sensitivity because fluorine has a large $\lambda^2 J(J + 1)$. Shimizu et al.[64] reported a WIMP-search result with highly radiopure CaF$_2$ crystals. KIMS[42] using 34.8 kg of CsI(Tl) set a better SD limits with a 3490 kg $\cdot$ days of exposure.

3.1.2   Liquid Noble-gas scintillator

Liquid noble gases are excellent scintillators, and furthermore, simultaneous ionization signals can be collected with an existence of a certain electric field. Particularly, liquid xenon (LXe) have a good intrinsic properties; large mass number, high density, high radio purity, and high light output. Though the mass number of liquid argon (LAr) is less than that of LXe,

SI 90% C.L. upper limits and allowed region

SD 90% C.L. upper limits and allowed region
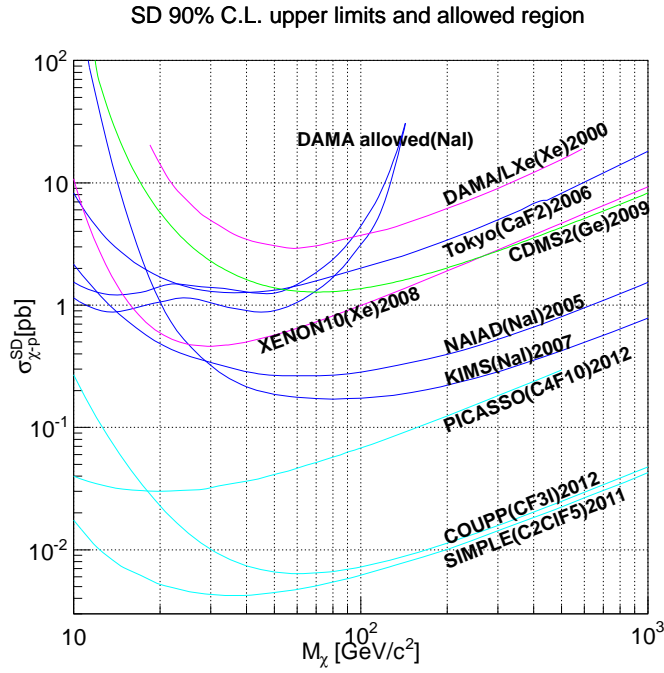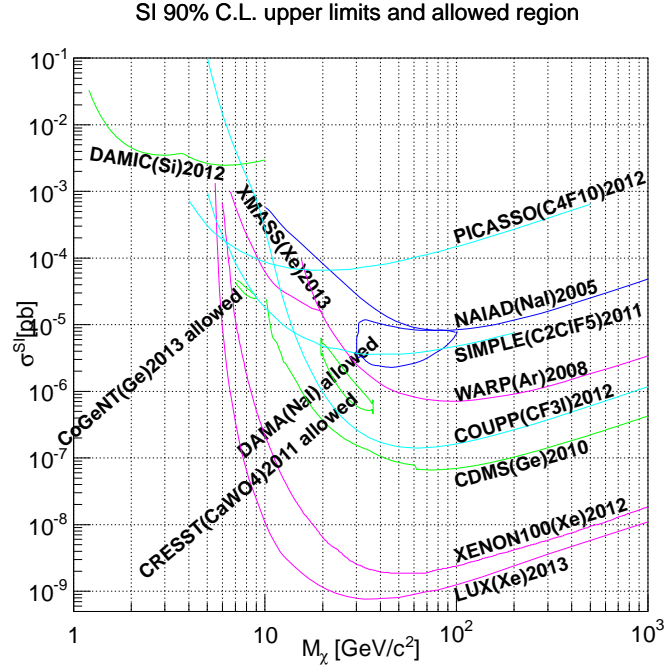
Figure 3.1.1: Results of direct dark matter search experiments. Upper and lower figures are searches of SI and SD χ-p interacting WIMPs, respectively See Table 3.0.1 for references. Region enclosed by line is allowed region (DAMA). Other upper regions of lines are excluded regions. Color indicates the type of detector; blue for solid scintillator, purple for liquid noble gas detector, green for semiconductor detector, and sky blue for bubble chamber.
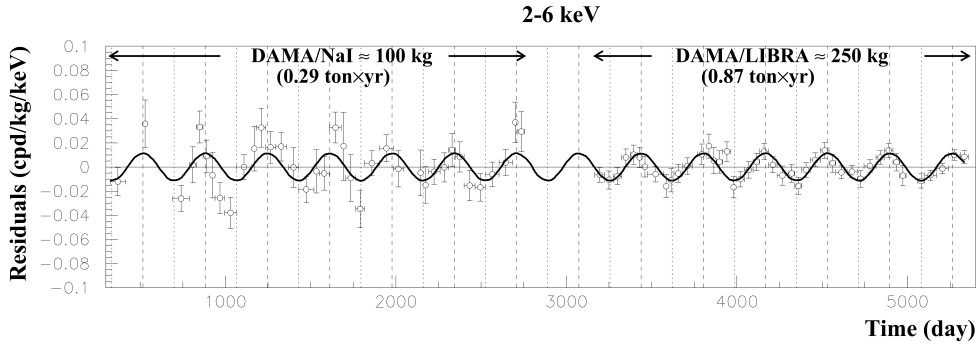
2-6 keV

Figure 3.1.2: The observed annual modulation of the residual event rate of $2 - 6\,\mathrm{keV}$ energy range acquired over 13 annual cycles by DAMA and DAMA/LIBRA with a total exposure of $1.17\,\mathrm{ton\cdot year}$[37]. The horizontal axis shows the days from DAMA/NaI started. Solid line is the best fit sine curve.

LAr has the advantage of being low cost. There are two types of liquid noble-gas dark matter detectors. One is a single phase detector which detects only a scintillation signal by photon detectors. Single phase detectors are constructed as simple as possible to reduce the background from detector itself. Environmental gamma-ray background can be rejected by the self shielding, and a pulse shaping analysis is used for the nuclear recoil discrimination. The other is a two phase detector which has a gas phase in addition to the liquid phase and detects not only the scintillation signal but also the ionization signal. The ionization signal is detected as a gas amplification scintillation signal in the gas phase caused by the primary electron drifted out of the liquid phase. The ionization signals for nuclear recoils are quenched much more than the primary scintillation signals, while the ionization signals for electron recoils are not quenched so much. Therefore, the ratio of the ionization signal and the primary scintillation signal provides a powerful electron discrimination power.

DAMA/LXe[43] and XMASS are the single phase detectors using LXe. DAMA/LXe using $6.5\,\mathrm{kg}$ of liquid $^{129}\mathrm{Xe}$ performed the dark matter search with a $2500\,\mathrm{kg\cdot days}$ exposure. As two phase detectors using LXe, there are LUX[47] and XENON[45]. LUX using $118\,\mathrm{kg}$ of LXe performed a dark matter search with a $10065\,\mathrm{kg\cdot days}$ exposure and obtained the best limit for the SI interacting WIMP in the mass range of $10 - 1000\,\mathrm{GeV}$. WARP collaboration has built and deployed a $3.2\,\mathrm{kg}$ LAr detector at LNGS and performed a dark matter search with an exposure of $96.5\,\mathrm{kg\cdot days}$[48].

3.1.3 Semiconductor detector (bolometers, CCD)

In the direct search using bolometers, the nuclear recoil energy is detected via phonons (temperature rising). The heat capacity of a dielectric crystal is proportional to T^3 at the

low temperature, thus at the mK temperature, the small energy deposition from a nuclear recoil can yield a measurable increase of a target crystal. Since the electron-hole pairs is also generated at the same time in the semiconductor bolometers, electron background can be discriminated by using the difference of ionization/phonon ratio between electrons and nucleus. In addition, some groups have developed "scintillating bolometers" which detect scintillation photons together with heat as an alternative method for the electron event rejection.

CDMS-II experiment operated towers of Ge and Si crystals with a thickness of 1 cm cooled down to 40 mK[49]. The mass of the Ge and Si crystals were 250 g and 100 g, respectively. Since the depth of event can be measured from the difference of detecting time of phonon and charge, CDMS detector can reject surface electron events. They accumulated an exposure of 612 (140.2) kg · days with Ge (Si) detectors, after the event selection, 2(3) events remained for the Ge(Si)-run, but it can be explained by the background and their statement is "Though this result favors a WIMP interpretation over the known background-only-hypothesis, we do not believe this result rises to the level of discovery." and further investigation is needed. CoGeNT project uses 443 g of p-type point contact Ge detector with a low-threshold of 0.4 keV, and performed a dark matter search with an exposure of ~ 200 kg · days[50] . In the low energy region, the annual modulation of event rate was observed for over one year at $\sim 2.8\sigma$, and obtained the allowed region at low mass region as shown in the upper panel of Figure 3.1.1. CRESST-II experiment uses 10 kg of $CaWO_4$ crystals and read two types of signals, a phonon signal and coincidently produced scintillation light for electron discrimination[51]. After an exposure of 730 kg · days, due to the excess of the event rate as expected for background, CRESST-II set the allowed region as shown in the upper panel of Figure 3.1.1. In order to explain the "positive" results described above, a low mass dark matter (~ 5 GeV) was supposed. However, the low mass region is difficult to discuss because the sensitivity changes rapidly due to the energy threshold. DAMIC experiment uses low noise CCD with a very low energy threshold of 40 eV, and is dedicated to the search for low-mass WIMP[52]. They performed a dark matter search using a CCD of 1 g with an exposure of 1.5 kg · day, and obtained the best limit in the low-mass region.

3.1.4 Bubble chamber

Bubble chambers are the detector made of superheated liquids. Bubble chambers are kept in a delicate metastable superheated state, and ionizing radiation particle makes a local vapor phase with the energy deposition along its path. Rapidly growing bubbles are photographed and the chamber is then reset by a fast recompression to the metastable liquid phase. These devices have advantages of the electron discrimination, a large mass, and a target selection for

the SD WIMP searches. But they have disadvantage of being a threshold-type detector, or no way to to detect the nuclear recoil energy. The superheated liquid can be tuned to respond exclusively to particles with a large stopping power, so that muon and electron events all fall well below the bubble nucleation threshold.

COUPP[53], SIMPLE[54], PICASSO[55] experiments applied a superheated droplet detector for the direct dark matter search using piezoelectric sensors as the trigger. COUPP performed a dark matter search using $4.0\,kg$ of CF_3I bubble chamber with an exposure of $553\,kg \cdot days$. SIMPLE performed a dark matter search using $0.215\,kg$ of C_2ClF_5 bubble chamber with an exposure of $13.67\,kg \cdot days$. PICASSO performed a dark matter search using $0.72\,kg$ of ^{19}F in C_4F_{10} bubble chamber with an exposure of $114\,kg \cdot days$. Since ^{19}F large $\lambda^2 J(J+1)$ term is used for a target of these detectors, they have strong limit for SD interaction.

3.2 Direction-sensitive experiment

Direction-sensitive experiments are to measure the incoming direction of WIMPs with detectors to measure the direction of nuclear recoil tracks. Typical length of the nuclear track with an energy of $100\,keV$ is less than $1\,mm$ in the gas at $1\,atm$ pressure. Thus, low pressure gaseous detectors are used in many cases. Detectors using emulsion or DNA which have both directionality and large-mass target have also been studied. Furthermore, by measuring the recombination of the drift electron, high pressure noble-gas detector may provide some directional information[65].

3.2.1 Gaseous detector

Low pressure gaseous time-projection-chambers, commonly coupled with micro-patterned gaseous detectors (MPGDs), namely μ-TPCs, are widely studied for direction-sensitive dark matter searches. The requirement for the use of low pressure gas implies large volume detectors of more than $1\,m^3$ will eventually be needed. Although the target mass density is $\sim 1/1000$ times less than that of conventional detectors, the directional signal can be a strong evidence of the detection of the dark matter.

Typical feature of gaseous detectors

μ-TPC obtains a track of a charged particle in the following sequences. The detector gas is ionized along the path of a charged particle, ionized electrons drift along the electric field that is applied along the z-axis in the gas, undergo gas amplification if necessary, then reach

the 2-dimensional detector. Using x and y determined by the 2-dimensional detector and z determined by the time when the electron reaches to the 2-dimensional detector. A three dimensional track is obtained.

A target gas should have a large cross-section of WIMP-nucleus scatterings and a small cross-section of the neutron interaction because it is impossible to discriminate the WIMP recoil from the neutron recoil in principle. Since hydrogen has a large cross-section to neutron, a gas which contains one or more hydrogens (e.g. CH_4, C_2H_6) should be avoided. The noble gases such as Xe and Ar are often used in a gas detector, in particular, the sensitivity of SI interaction is high for Xe due to the large mass number. However, the diffusion of electron during drift in the noble gas is very large and it requires fine optimizations to construct a large detector measuring fine tracks. MAGBOLTZ[66] calculations of the diffusion constant for several gas are shown in Figure 3.2.1. A negative ion time projection chamber (NITPC), the primary electron is rapidly captured by electron negative gases such as CS_2 and drift as the negative ions drift along an electric field, has potential to realize a very small diffusion. It is because drift ions remain in or near thermal equilibrium with the gas, and diffusions are suppressed to the thermal levels. CF_4 gas, although it is not an electron negative gas, has small electron diffusions because the electron drift velocity in CF_4 gas is high as shown in Figure 3.2.2. CF_4 gas is easy to handle because it is inert and harmless, while CS_2 gas is ignitable and harmful. We note that CS_2 gas has an advantage to the SI interaction search with large mass number of ^{32}S and CF_4 gas has an advantage to the SD interaction search with a large $\lambda^2 J(J+1)$ term. The properties of CF_4 gas are summarized in Table 3.2.1.

a chemical formula	CF_4
name	carbon tetrafluoride
appearance	colorless, odorless, inert and nonpoisonous
molecular weight	$88.01\,\mathrm{g/mol}$
density	$3.76\,\mathrm{g/l}\,(15°C, 1\,\mathrm{atm})$
melting point	$89.55°K$
boiling point	$145.35°K$
W value	$54eV$

Table 3.2.1: Properties of CF_4 gas.

Direction-sensitive detector should have a position resolution better than a typical nuclear track length of interest. The lengths of nuclear tracks in several types of gas calculated by SRIM[67] as a function of the initial energy are shown in Figure 3.2.3. In the lower pressure gas, longer tracks are expected and thus a lower energy threshold is realized. But low pressure gas detector needs a large volume and also often causes the unstability of the operation.
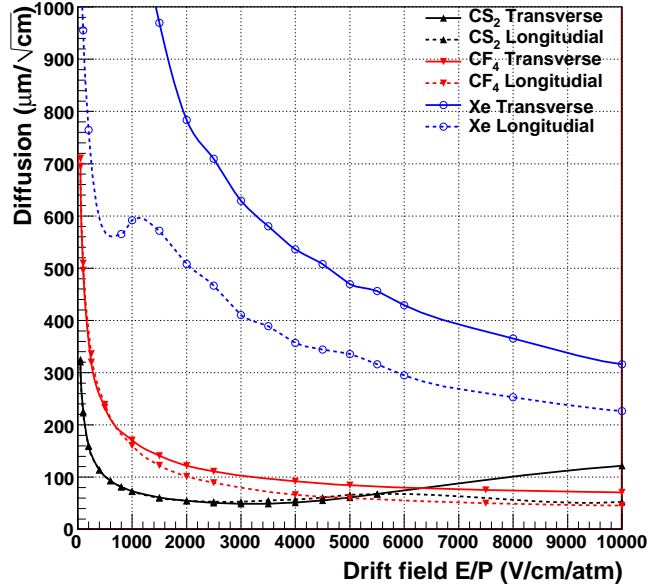
Figure 3.2.1: Gas diffusions of electrons or negative ions as a function of the electric field at a temperature of 300K calculated by MAGBOLTZ. Dotted and Solid line are longitudinal and transverse diffusion, respectively. Color shows the molecular; red, blue and black correspond to CF_4, Xe and CS_2, respectively.

We need to overcome these difficulties in order to detect the very distinct signals of the dark matter.

It is important to consider a nuclear quenching factor for low energy nuclear recoils. Nuclear quenching factor, $F_q = E_{ionized}/E_{total}$, is the ratio between total energy loss and energy used for ionization. Nuclear quenching factors for several gas detectors were summarized in [68]. The nuclear quenching factors of ^{4}He, ^{12}C and ^{19}F ions in CF_4 gas were calculated by SRIM as shown in Figure 3.2.4. These values have nucleus-, energy- and also gas pressure-, dependence as shown in the figure. They are used when we convert the measured (ionized) energy to the recoil (total) energy in dark matter search experiments.

Experiments with gaseous detectors

We review the experiments with gaseous detectors and development status in the following paragraph.

DRIFT experiment pioneered the study of the directional detection of the dark matter with $1\,\mathrm{m}^3$ of gas detectors. In particularly, they have been leading the field with the background
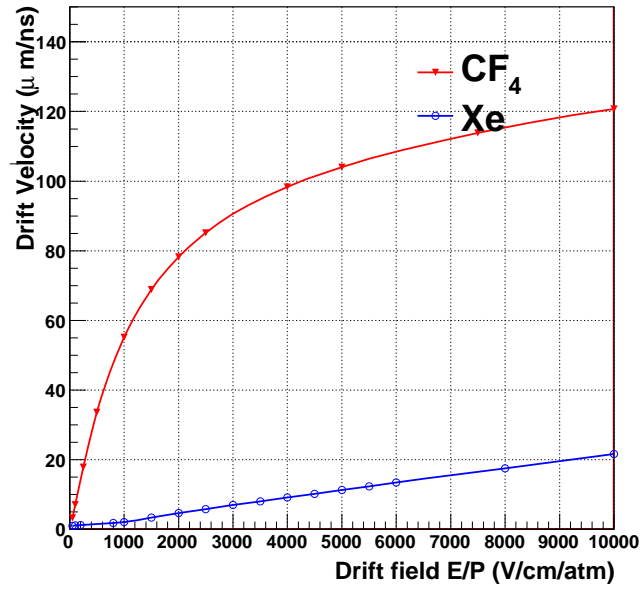
Figure 3.2.2: Drift velocities of electrons as a function of electric field calculated by MAGBOLTZ for CF_4(red) and Xe(blue).
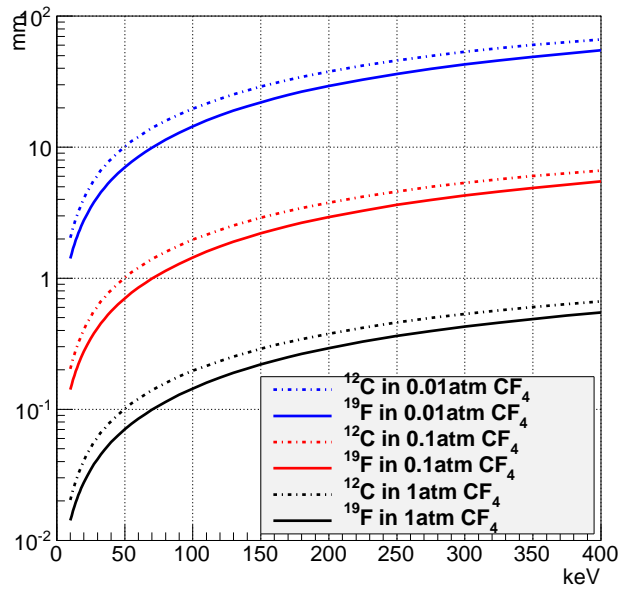
Figure 3.2.3: Track length of recoil ^{12}C(dotted line) and ^{19}F(solid line) in CF_4 gas calculated by SRIM with each pressure (blue:0.01atm, red:0.1atm, black:1.0atm).

52
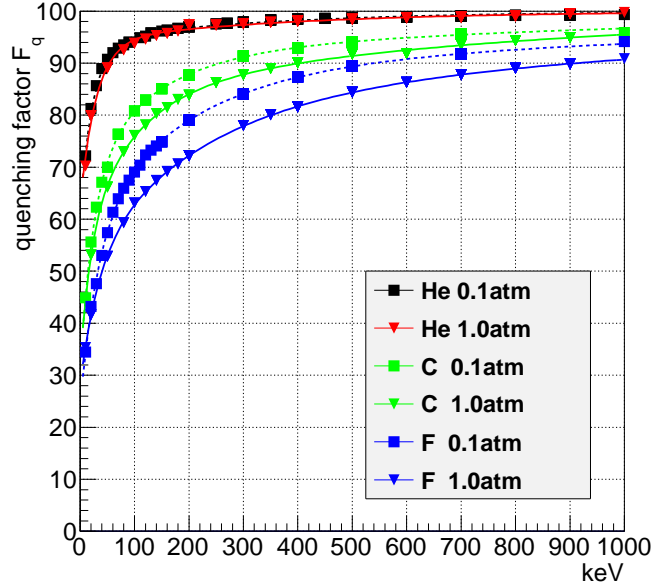
Figure 3.2.4: Quenching factor of various nucleus in CF_4 gas calculated by SRIM[67]. Each line shows different nuclei-pressure combination as shown in the legend.

reduction techniques[56]. They performed a dark matter search with DRIFT-IId detector for 47.4-days live time with $139\,g$ of a mixture of $30\,torr\,CS_2$ and $10\,torr\,CF_4$ gas. They conducted a fine-tuned cut analysis without direction information and obtained comparable limits to solid detectors, $1.8\,pb$ for a WIMP mass of $100\,GeV/c^2$ (Figure 3.2.5). They are also starting R&Ds to use MPGD readouts in order to overcome their potential weakness of the readout pitch of $2\,mm$.

DMTPC collaboration proposed a new method to detect the recoil tracks using a CCD-readout TPC[57]. They demonstrated that the projected images of nuclear recoil tracks could be precisely taken via scintillation photons produced during the avalanche process in CF_4 gas. Although only 2 dimensional projected track is obtained instead of 3 dimensional track due to the mechanism of the readout, their technique is very notable for the detection of the track sense. In 2011, they reported the surface dark matter search result, and improved the SD direction-sensitive limit to $2.0 \times 10^3\,pb$ for $115\,GeV/c^2$ dark matter (Figure 3.2.5).

MIMAC project[59] and D3 project [69] are also developing the gaseous tracker. MicroMEGAS[70] is used for MIMAC, and GEMs[71] with an ATLAS FE-I3 pixel chip[72] are used for D3.

NEWAGE with CF_4 gas and a fine pitch gaseous detectors has obtained first direction-sensitive limits in 2007, and improved to $5400\,pb$ for WIMP mass of $150\,GeV/c^2$ in 2010

(Figure 3.2.5)[58]. Properties of the current and developing detector of each project are in Table 3.2.2. NEWAGE has advantages in the readout pitch and the effective volume against DRIFT and DMTPC, respectively.
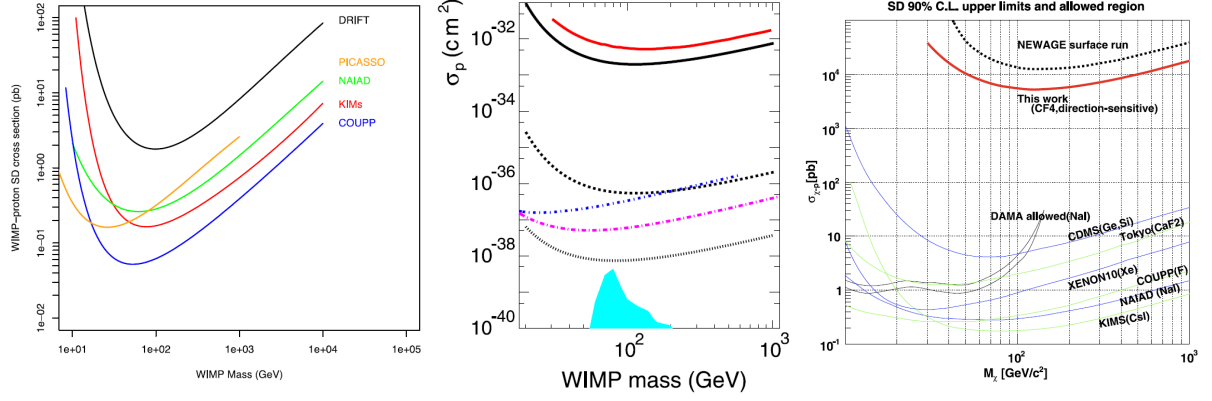
Figure 3.2.5: Results of direction-sensitive direct dark matter search experiments. In left figure, black solid line shows the result of DRIFT(2012)(without direction-sensitive analysis)[56]. In the central figure, black solid line shows the result of DM-TPC(2011)[57]. In right figure, red solid line shows the result of NEWAGE(2010))[58]. For more information, see references.

detector	gas	pressure	volume (cm^3)	device	readout pitch	track	head-tail	ref
NEWAGE-0.3a	CF$_4$	0.2 atm	$23 \times 28 \times 31$	μ-PIC	400 μm	3D	no	[58]
NEWAGE-0.3b'	CF$_4$	0.1 atm	$30 \times 30 \times 41$	μ-PIC	400 μm	3D	no	this thesis
DRIFT-IId	75%CS$_2$ 25%CF$_4$	40 torr	$100 \times 100 \times 100$	MWPC	2 mm	3D	1D	[56]
DRIFT-III	CS$_2$	40 torr	$100 \times 100 \times 100$	MWPC	2 mm	3D	1D	
DM-TPC	CF$_4$	50 torr	$14.6 \times 14.6 \times 19.7$	CCD	256 μm	2D	2D	[57]
DM-TPC 2	CF$_4$	50 torr	$\phi 25 \times 25$	CCD	256 μm	2D	2D	
MIMAC	70%CF$_4$ 28%CHF$_3$ 2%C$_4$H$_{10}$	50 mbar	$10 \times 10 \times 25$	micro MEGAS	424 μm	3D	no	

Table 3.2.2: Properties of gaseous detectors for direction-sensitive dark matter searches.

3.2.2 Emulsion

Nuclear emulsions. though they are solid detector, can potentially be used for direction sensitive dark matter experiments because of their good position resolutions. Emulsion has AgBr in gelatin, and tiny cluster of Ag is generated along the pass of a charged particle. Then, by developing the cluster of Ag, a track of charged particle is observed by microscope. Although emulsions have no time resolution, they have advantage in scalability. Nano imaging tracker (NIT) have been developed to detect the fine track such as $<\sim \mu$m at Nagoya university[60],

and it is suitable for a direction-sensitive dark matter search. In addition, an underground experiment at Gran Sasso is scheduled.

3.2.3 DNA Tracking Chamber

Detectors made of DNA (deoxyribonucleic acid) could provide nanometer resolution for tracking and energy threshold of $0.5\,\text{keV}$[61]. The structure of DNA tracking chamber is that thousands of strings of single stranded DNA (all with known base sequences) are hung in a plate of Au side by side like a curtain. When a charged particle comes into this detector, DNAs are cut along the path of charged particles. DNAs that were cut are amplified and read by using well-known techniques of molecular biology. Of course DNA detector needs vigorous R&D, it can be an ultimate detector with the highest position resolution.

3.2.4 High pressure Xe detector

Nygren proposed a new concept based on columnar recombination in dense xenon gas, sensing nuclear recoil direction relative to a TPC drift field[65]. The central advance is that kind of directionality information is obtained through a comparison, event-by-event, of the ionization signal and recombination signal that are produced prior to drifting the track ionization. The optimum xenon density may be about ten bars, much higher than that of low pressure gas detectors, and large mass experiment can be performed.

Chapter 4

Detector

NEWAGE (NEw general WIMP search with an Advanced Gaseous tracker Experiment) is one of the direction-sensitive direct dark matter search experiments. As mentioned in Section 2.4.3, directional information is certainly a strong evidence of the discovery of the dark matter. NEWAGE adopts a three dimensional gaseous tracking detector μ-TPC whose readout is a μ-PIC, one of the micro patterned gaseous detectors (MPGDs). The μ-PIC has two advantages; fine tracking and scalability. The finer pitch of μ-PIC ($400\,\mu$m) than that of MWPC ($2\,$mm), realizes a higher direction sensitivity. The large size μ-PIC can be madeat a low cost because it is made by print circuit board technology. CF_4 is selected for the target gas because the gas diffusion is small and fluorine has a relatively large SD cross section. There has been no direction-sensitive detector with a sensitivity reaching to the MSSM region yet. Final goal of NEWAGE is to detect a strong evidence and to study the properties of the dark matter by reaching the MSSM region, in particular as shown in Figure 4.0.1[73].

Previous measurements were performed in Kamioka with NEWAGE-0.3a detector which improved the direction-sensitive limit of spin-dependent WIMP-proton cross section down to $5400\,$pb for $150\,$GeV[58]. In that experiment, the gas pressure was set to $0.2\,$atm, the energy threshold was $100\,$keV with an angular resolution of $46°$ and an old data acquisition protocol (DAQ-mode1, show Section 4.2) was used. We developed a new detector, NEWAGE-0.3b', to improve the cross section limit by more than one order of magnitude by reducing the background and increasing sensitivity with a lower energy threshold.

In this chapter, details of NEWAGE-0.3b' detector are described. The structure of the detector is described in Section 4.1, and the data aquitision system is explained in Section 4.2. The simulator is written in Section 4.3, and the typical performances are described in Section 4.4.
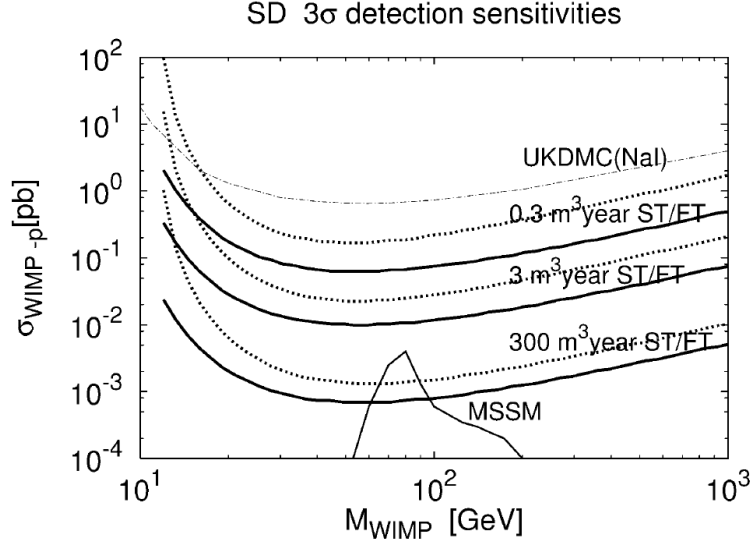
Figure 4.0.1: Sensitivity goals of the NEWAGE project. Thick and dotted lines show expected 3σ asymmetry detection sensitivities by the ST(semi-tracking) and FT(full-tracking) modes, respectively. Details are described in [73]. An experimental result of NAIAD (thin dashed dotted line labeled UKDMC) and MSSM predictions (thin line labeled MSSM) are also shown [41, 74].

4.1 NEWAGE-0.3b' detector

A new detector, NEWAGE-0.3b', was designed and developed to improve the sensitivity by one order of magnitude. NEWAGE-0.3b' consists of a micro time projection chamber (μ-TPC), its electronics system, and the gas circulation system (Figure 4.1.1).
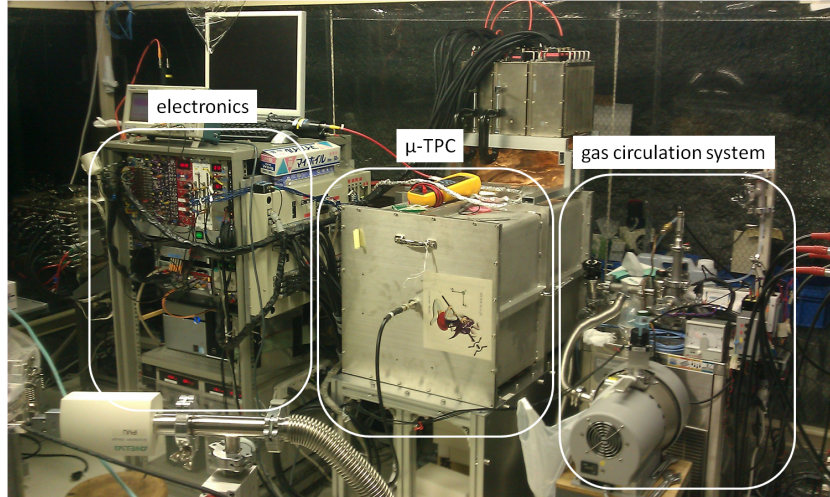
Figure 4.1.1: The photograph of whole system of NEWAGE-0.3b' in Kamioka underground laboratory.

57
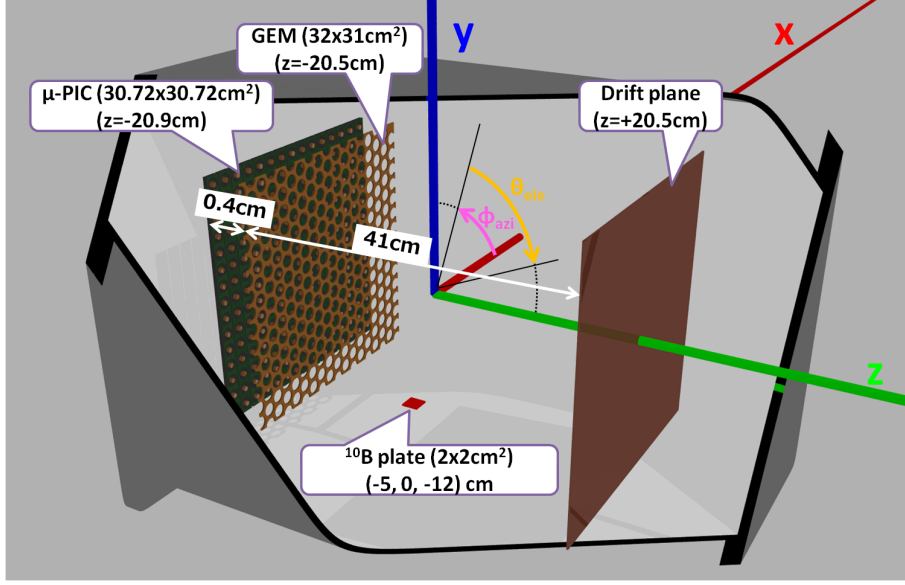
Figure 4.1.2: The schematic image of the μ-TPC named NEWAGE-0.3b'. The coordinate system, with its origin at the center of the detection volume, is also shown. Red, blue and green lines shows the x, y and z axis. A glass plate with a thin layer of ^{10}B is set at $(-5, 0, -12)$ cm for the energy calibration.

A schematic view of the μ-TPC and the internal structure are shown in Figure 4.1.2 and Figure 4.1.3, respectively. μ-TPC consists of a micro pixel chamber (μ-PIC) which is a two-dimensional fine-pitch imaging device[75], a gas electron multiplier (GEM)[71], and $30 \times 30 \times 41\,\mathrm{cm}^3$ of detection volume. x, y and z axis are defined in Figure 4.1.2, and the unit is cm in this thesis unless otherwise mentioned.

A μ-PIC is manufactured using printed circuit board (PCB) technology. PCB technology realizes an economical large-size detector production, which is one of the most important requirements for the fabrication of a dark matter detector. The $30.72 \times 30.72\,\mathrm{cm}^2$-sized μ-PIC has 768×768 pixels with a pitch of $400\,\mu$m, which are connected by 768 anode strips and 768 cathode strips. The anode and cathode strips are orthogonally formed and thus we obtain the two-dimensional position of a hit pixel. The photographs and schematic the structure of the μ-PIC are shown in Figure 4.1.4. The μ-PIC works as a main gas-amplifier and as readout electrodes. In order to obtain a sufficient gas gain, a GEM is settled 4 mm above the μ-PIC as a sub-amplifier. The effective area of the GEM is $31 \times 32\mathrm{cm}^2$ covering the whole area of the μ-PIC. The GEM area is segmented into 8 sub-areas to reduce discharge damages. The substrate of the GEM is LCP of $100\,\mu$m thick and the hole size and pitch are $70\,\mu$m and $140\,\mu$m, respectively. The drift length is 41cm, which was determined by the optimization between the target-increase advantage and the angular-resolution determination with a longer drift length.
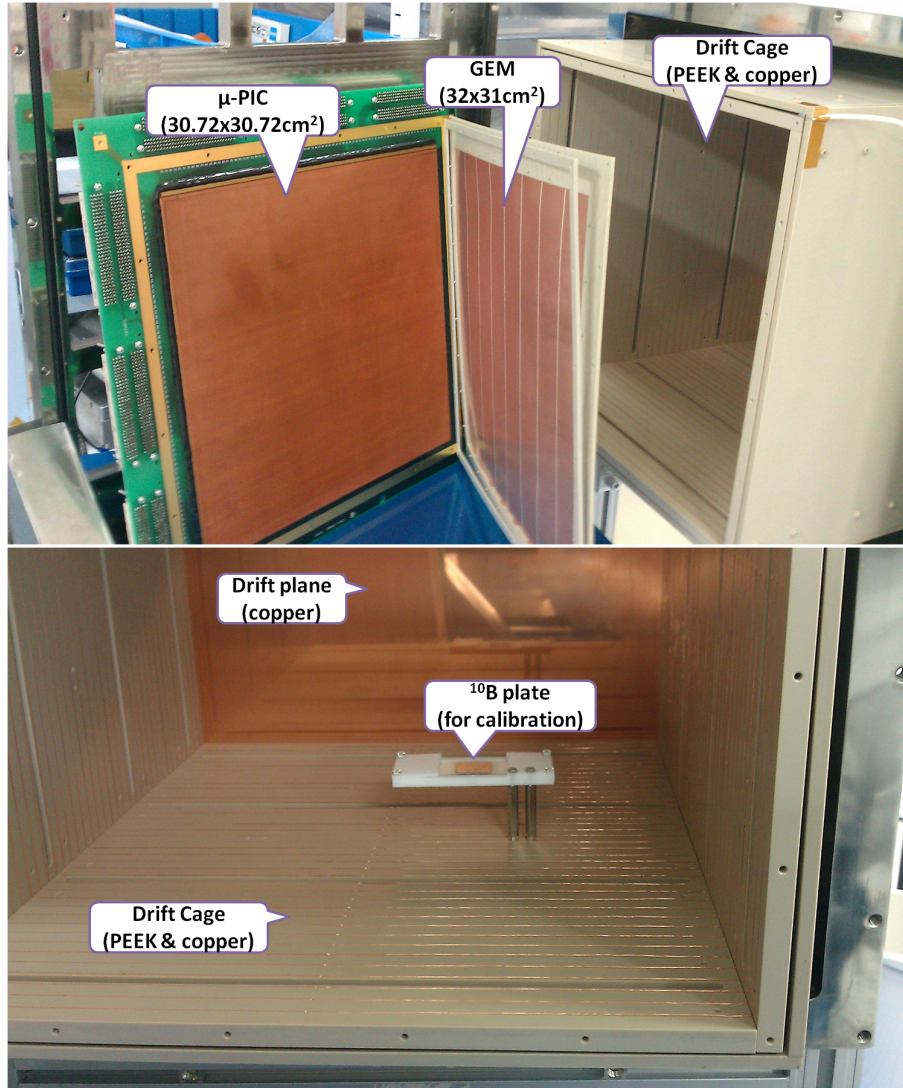
Figure 4.1.3: The μ-PIC and the GEM during their installation (upper) and inner structure of TPC including the ^{10}B-evapolated glass plate (lower).

The electric field is formed by the drift plane and wires on the side walls of the drift region with a spacing of $1\,\text{cm}$. Applied voltages for the μ-PIC, the GEM and the drift plane are listed in Table 4.1.1, where a stable operation with a combined (μ-PIC$\times$GEM) gas gain of 2500 was obtained. A glass plate with a thin layer of ^{10}B is installed at the position of $(-5, -12, 0)\,\text{cm}$ for the energy calibration. The size of the ^{10}B layer is $2 \times 2\,\text{cm}$ and the designed thickness is $0.6\,\mu\text{m}$. The μ-TPC is placed on a $2.5\,\text{cm}$ thick stainless-steel vacuum vessel filled with CF_4 gas at $0.2\,\text{atm}$. As mentioned in Section 3.2.1, CF_4 gas is suitable for a direction-sensitive spin dependent dark matter search.
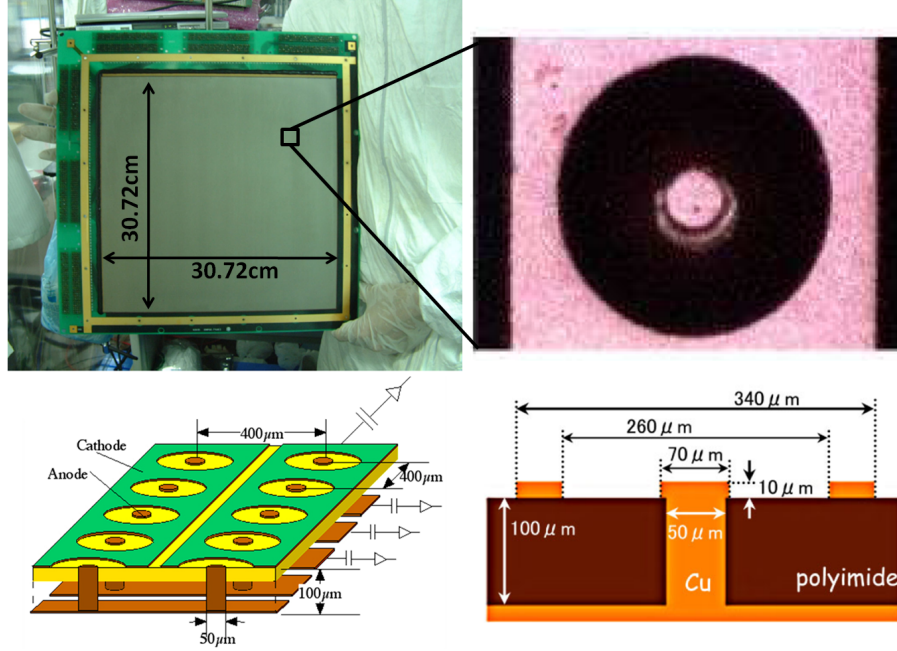
Figure 4.1.4: The photograph of μ-PIC (left top) and the schematic view of μ-PIC (left bottom). Upper right figure shows the enlarged photograph by microscope. Bottom right figure shows the cross-section view of the μ-PIC structure.

	voltage	current
μ-PIC	510 V	$\sim 10\,\mathrm{nA}$
GEM-top	$-530\,\mathrm{V}$	$< 1\,\mu\mathrm{A}$
GEM-bottom	$-280\,\mathrm{V}$	$< 1\,\mu\mathrm{A}$
DRIFT	$-3.91\,\mathrm{kV}$	$20.2\,\mu\mathrm{A}$

Table 4.1.1: Supplied voltages for μ-PIC, GEM-top, GEM-bottom, and drift plane.

A gas circulation system with cooled charcoal was developed for NEWAGE-0.3b'. The schematic drawing is shown in Figure 4.1.5. The aims of this system are to reduce radon, which is a serious background source for dark matter searches, and to keep the gas quality (gas gain and drift velocity) during long time use (more than one month). The gas in the vessel passes through the charcoal, where 100 g of charcoal (the product name is TSURUMICOAL 2GS) absorb radon and impurities as well. The pump (XDS5 Scroll Pump (EDWARDS)) is an oil-free pump, and works with a low pressure gas at 0.1 atm. A needle-type valve was used to control the flow rate at 500 ml/min. A stable cooling at 230 K was realized by controlling a heater, while the cooler(CT-910 Cool Man Trap (SIBATA)) was always operated at its maximum cooling power.
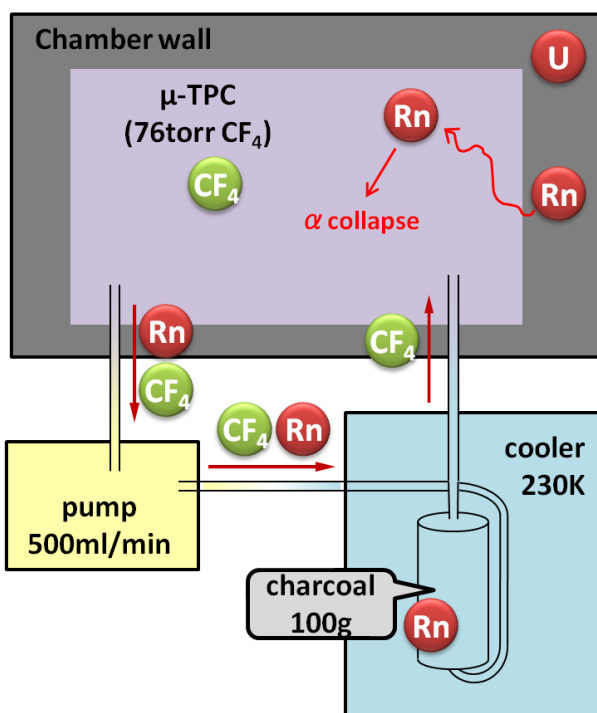
Figure 4.1.5: The schematic image of the gas circulation system for lowering radon backgrounds and keeping the gas quality.

4.2 Data acquisition system (DAQ)

A data acquisition system (DAQ) with a dedicated electronics for the μ-PIC readout was adopted for the NEWAGE-0.3b' detector[76]. The schematic structure of the DAQ is shown in Figure 4.2.1. Two types data, namely "track" by the memory board and "charge" by the flashADC, are mainly recorded by the DAQ system.

The DAQ has two types of trigger modes. One is the "self-trigger mode", where the TPC analog signals from 768 anode strips are grouped down to 16 channels and any one of their hits is used as the trigger. In this trigger mode, the absolute z position is not measured, but only the relative position is measured. The self-trigger mode is used otherwise mentioned in this thesis. The other is "external-trigger mode", for a measurement using a ^{252}Cf source. The signal of a prompt gamma ray or a neutron from ^{252}Cf detected by a plastic scintillator set nearby the source is used as a trigger. In this mode, the absolute z position of the tracks are measured. The drift velocity and the angular resolutions are measured with the external-trigger mode.

Two types of DAQ-mode for "track" data with a different measured parameters as listed in Table 4.2.1 were used for this work. DAQ-mode5 records the addresses and time-over-
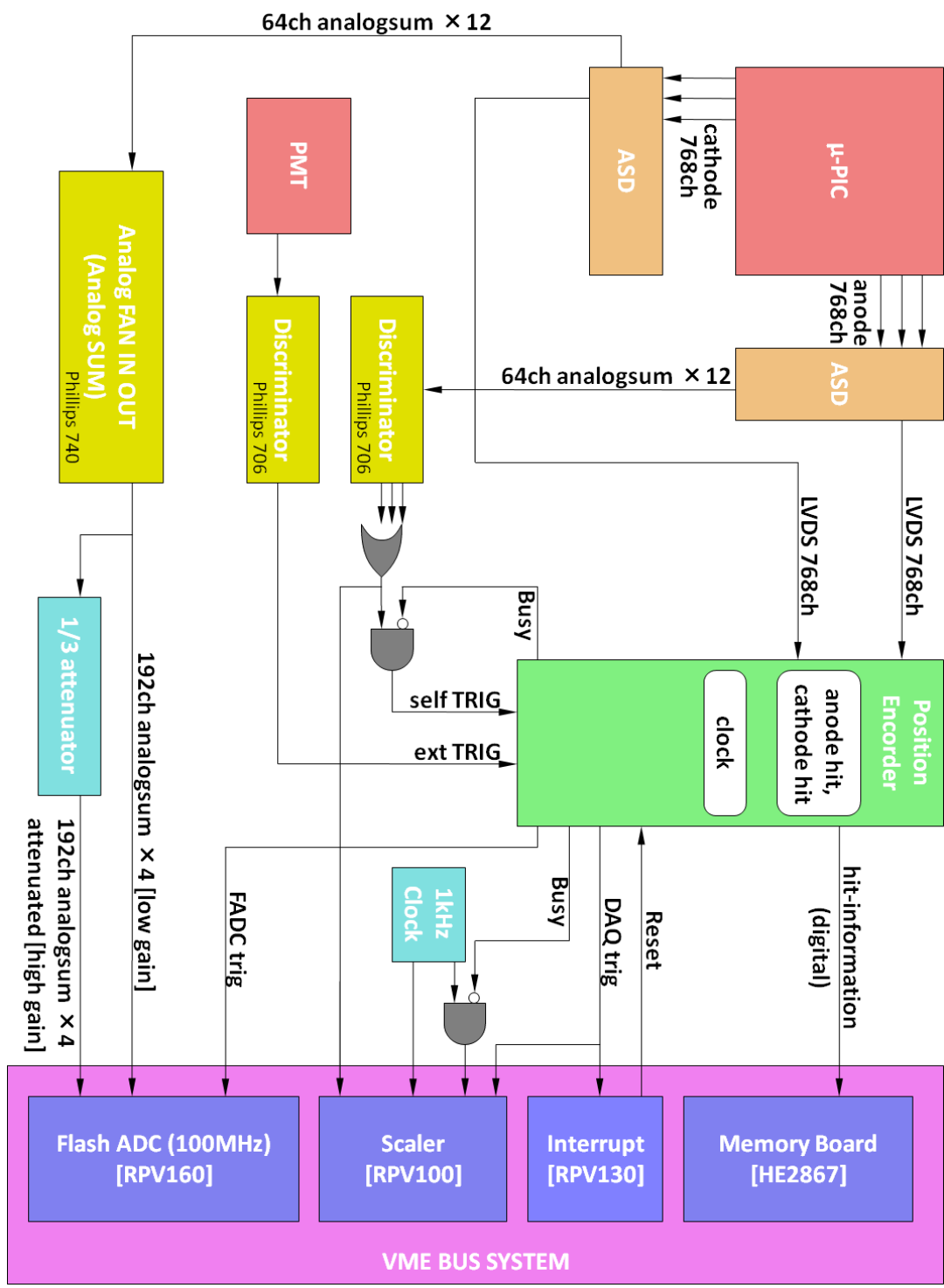
Figure 4.2.1: Data acquisition system (DAQ) of NEWAGE-0.3b' detector.

DAQ mode	mode1	mode5
x-y coincidence	take	not take
strip address to record at each clock	$X_{\min}$, $X_{\max}$, $Y_{\min}$, $Y_{\max}$	all
Time over threshold (TOT)	not take	take

Table 4.2.1: The list of the DAQ mode.
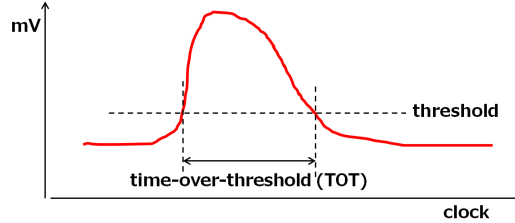
Figure 4.2.2: The schematic image of time-over-threshold (TOT). Red line shows the waveform of a strip.

threshold of all hit strips (TOTs). TOT is the time duration of the waveform corresponding to the energy deposit as shown in Figure 4.2.2. Here we use DAQ-mode5 with self-trigger mode. DAQ-mode1 records by reducing the size of data by taking x-y coincidence and limiting the number of output addressed for the "track" information. DAQ-mode1 was thus used for the external-trigger mode because the dead time of DAQ-mode5 is too long to operate with the external-trigger mode.

For "charge" information, analog signal of 768 cathodes are amplified and grouped down to 4 channels, then these waveforms are recorded by a 100 MHz flash ADC. From the summed waveforms (FADC-sum), the energy deposition of a charged particle is evaluated.

4.3 Simulator

A Monte Carlo simulation was used to evaluate the detector performance. The full process, starting from the generation of incoming particles, followed by the interaction of the particles in the detector, the electron drift in the gas volume, the gas amplification nearby the detection plane, the amplification and the discrimination by the preamplifier, the data reduction in the FPGAs, and the data acquisition, was simulated.

A simulation package named Geant4[77], originally developed for high-energy physics experiments and now being used widely in related fields, was used for the generation, transportation and interaction of the incoming particles. Gamma-rays, electrons, neutrons, and α particles were generated inside and outside of the detector for the performance evaluation (Section 4.4)

and the background estimation(Section 6). The version and physics lists used in the simulator are listed in Table 4.3.1.

The electron drift and the gas amplification parts were simulated mainly based on MAG-BOLTZ package[66]. MAGBOLTZ is a package to simulate the transportation of electrons in gas mixtures. Electron clouds generated by a reaction in the detector volume are diffused during the drifting towards the detection plane. The electron diffusion in the CF_4 at 0.1 atm gas was simulated in our code. The diffusion size orthogonal($\sigma_{\mathrm{transverse}}$) and parallel($\sigma_{\mathrm{longitudial}}$) to the drift direction were $0.27\,\mathrm{mm}/\sqrt{\mathrm{cm}}$ and $0.19\,\mathrm{mm}/\sqrt{\mathrm{cm}}$, respectively. The electrons were diffused, amplified in the GEM and around the μ-PIC pixels, then detected by the μ-PIC detector. Positions and timings of the detected electrons were recorded.

After the charge detection, the data acquisition system was simulated by our original code. The signal were amplified and discriminated by the preamplifires with the specifications listed in Table 4.3.2. Then the DAQ system was simulated and the "track" and "charge" information were recorded by the same format as the real data.

version		G4.9.2.p03
physics lists	electromagnetic process	G4LowEnergyRayleigh
		G4LowEnergyPhotonElectric
		G4LowEnergyCompton
		G4LowEnergyGammaConversion
		G4LowEnergyIonisation
		G4LowEnergyBremsstrahlung
		G4eIonisation
		G4eBremsstrahlung
		G4eplusAnnihilation
		G4hLowEnergyIonisation
		G4EnergyLossTables
		G4hIonisation
	hadronic process	G4LElastic
		G4LEProtonInelastic
		G4NeutronHPElastic
		G4NeutronHPElasticData
		G4NeutronHPInelastic
		G4NeutronHPCapture

Table 4.3.1: The version and physics lists used for the simulation.

parameter	value
rise time	6 ns
decay time	70 ns
preamp gain	0.898 V/pC
mainamp gain	×7

Table 4.3.2: The parameters of ASD used in the detector response included simulator.

4.4 Detector performance

The performance of NEWAGE-0.3b' detector was precisely studied. Some of these performances were monitored during the dark matter run and summarized about its in Section 5.1.

4.4.1 Drift velocity

The electron drift velocity in the μ-TPC is needed to convert the arrival timing (clock) to the $z$position. We measured the nuclear recoil events in the μ-TPC using fast neutrons from ^{252}Cf source placed at $(0, 0, 47.5)$. In order to determine the starting time of drift, we used external-trigger mode with a plastic scintillator as the external trigger detecting gamma rays generated by fission of ^{252}Cf which simultaneously emits several fast neutrons. Because the trigger rate of external-trigger is very high, we used DAQ-mode1 which works with less dead time. Figure 4.4.1 shows the measured drift time distribution of nuclear recoils. The edge structure at $4.3\,\mu$sec corresponds to the event occurred just below the drift plane. The drift velocity was calculated to be $9.5\,\mathrm{cm}/\mu$sec since electrons took $4.3\,\mu$sec to drift 41 cm.
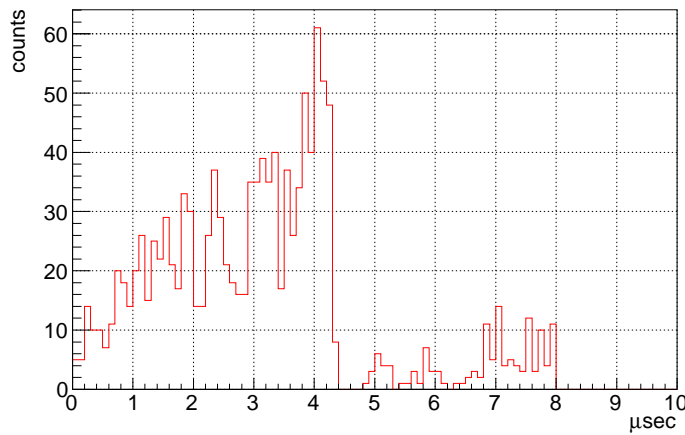
Figure 4.4.1: Drift time distribution of nuclear recoils in a drift velocity measurement.

65

4.4.2 Energy calibration and energy resolution

Since our purpose is to detect the recoil nuclei by dark matter, we calibrated the energy scale of μ-TPC using α particles instead of γ-rays and β-rays to measure the detector response to the nuclear tracks, because that is the case we expect in the dark matter nucleus scatterings. A glass plate on which ^{10}B is deposited in 2×2 cm is placed at the position of $(-5, -12, 0)$ cm for the calibration (see Figure 4.1.2). By irradiating the ^{10}B plate with thermalized neutrons from ^{252}Cf surrounded by polyethylene, α particles are generated in the μ-TPC by the following reactions,

$$^{10}\text{B} + \text{n} \longrightarrow ^4\text{He} + ^7\text{Li} + 2.79\,\text{MeV}(6\%) \tag{4.1}$$

$$^{10}\text{B} + \text{n} \longrightarrow ^4\text{He} + ^7\text{Li} + 2.31\,\text{MeV} + \gamma(0.48\,\text{MeV})(94\%). \tag{4.2}$$
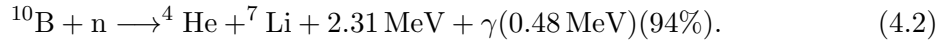
Since the cross section of reaction (4.2) is ~ 15 times larger than that of (4.1), neutron capture reaction of ^{10}B emits prompt gamma-rays with $478\,\text{keV}$ in most cases, and the ^{7}Li nuclei and α particle share $2.7 - 0.478\,\text{MeV}$, thus the generated α particle has $1.5\,\text{MeV}$ of kinetic energy. Because of the thickness (designed value was $0.6\,\mu\text{m}$) of the deposited ^{10}B, the $1.5\,\text{MeV}$ α particles make the shape of an edge rather than a peak. Figure 4.4.2 shows the result of the energy calibration. By comparing the simulation (blue line) and measurement (red points), we determined the energy scale.
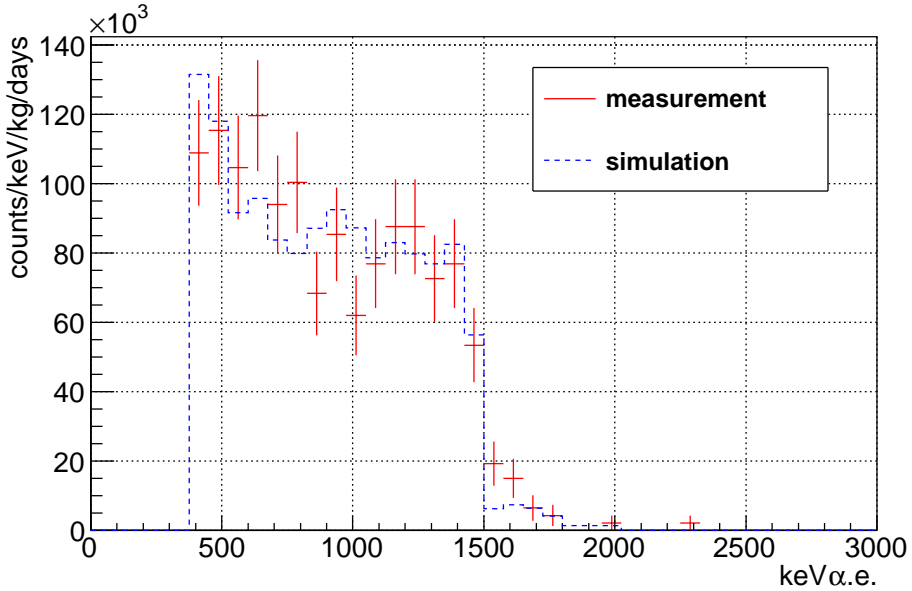
Figure 4.4.2: The result of an energy calibration using α particles from $^{10}\text{B}(\text{n}, \alpha)^7\text{Li}$. Blue line is simulated energy spectrum and red points are measured one.
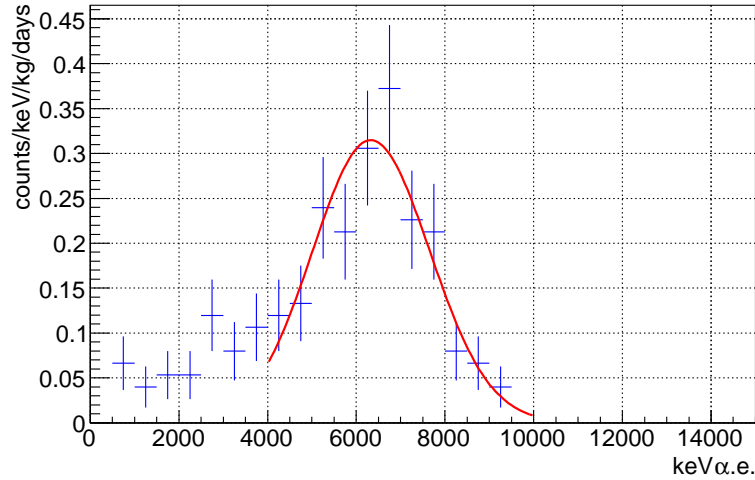
Figure 4.4.3: The measured energy spectrum of α particles due to the radon progeny (blue histogram). Red line is the fitted line in case of ^{220}Rn.

In order to check the linearity, we checked the energy scale of $\sim 6\,\mathrm{MeV}$ in addition to the ^{10}B calibration. The radon decay events within the TPC gas make peaks around $6\,\mathrm{MeV}$. Figure 4.4.3 shows the measured energy spectrum of α particles due to the radon progeny. There are two types of radon as ^{220}Rn and ^{222}Rn. The energy of α particles from ^{220}Rn and its progeny are $6.288\,\mathrm{MeV}$, $6.779\,\mathrm{MeV}$, $6.051\,\mathrm{MeV}$ and $8.785\,\mathrm{MeV}$, and that of ^{222}Rn are $5.490\,\mathrm{MeV}$, $6.003\,\mathrm{MeV}$ and $7.687\,\mathrm{MeV}$. Therefore, both radon makes peaks at $\sim 6\,\mathrm{MeV}$. Since the fraction of the ^{220}Rn and ^{222}Rn is not known, both cases were examined and the differences were treated as a systematic error. The linearity up to $6\,\mathrm{MeV}$ was thus confirmed within the systematic error as shown in Figure 4.4.4. Though the energy calibration in the lower energy region is important, direct measurement with a gas gain of 2500 is difficult. A linearlity check with a small-sized detector operated at higher gas gain with an ^{55}Fe source was performed and we rely on this measurement for the low energy linearlity[78].

We obtained the energy resolution from the width of the radon peak as $\sigma_{\mathrm{uni}} = 20 \pm 5\%$. The position dependence of the gas gain and the disappearance of electrons during the drift are considered as the factors that make this energy resolution. Detail on the radon study is described in Section 6.1.1. The electric noise component in the energy resolution was evaluated with the flashADC data. The off-timing-of-trigger waveforms were processed by the same manner as the on-timing data. Since the time-window for charge calculation depends on the energy, several energies were assumed to estimate the noise resolution. Figure 4.4.5 shows the result of the energy resolution due to the electric noise. Obtained energy resolution was $\sigma_{\mathrm{noise}} = 2\,\mathrm{keV}$ for $50\,\mathrm{keV}$.
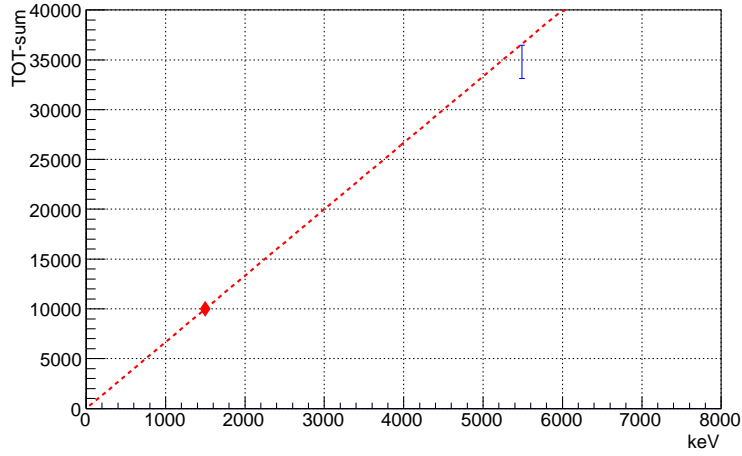
Figure 4.4.4: The relation of energy and FADC-sum. Red point is determined from ^{10}B calibration, and red line is the extension of this point. Blue point is obtained from radon fitting. The error bar is the systematic error due to the difference of ^{220}Rn and ^{222}Rn.
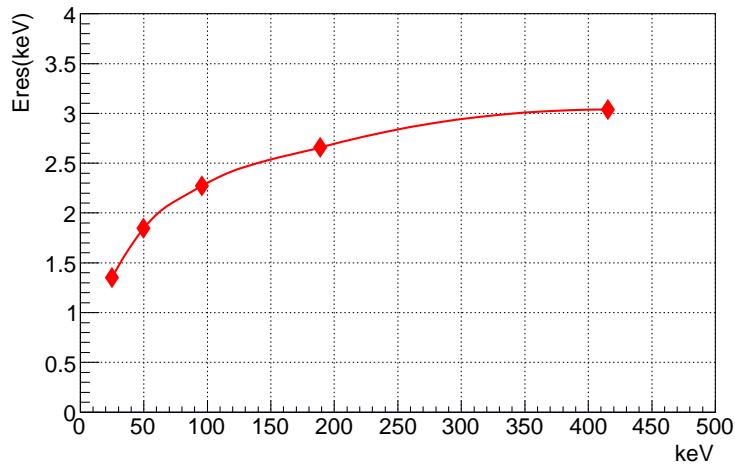
Figure 4.4.5: Estimated energy resolution (σ keV) due to the electric noise. The energy dependence is due to the width of waveforms.

4.4.3 Event selection

Several event selections are applied to the raw data to reduce several kinds of known background. Fiducial-cut, selecting $28 \times 24 \times 41\,\mathrm{cm}^3$ "fiducial volume" in the detection volume $30.72 \times 30.72 \times 41\,\mathrm{cm}^3$, is applied in the dark matter analysis in order to reject the charged particles from the walls and the ^{10}B plate. This fiducial-cut are applied for all measurements except for the ^{10}B calibration.

Another three types of cut is applied mainly to reduce gamma-ray background which is one of the serious background for the dark matter search experiments. For these cuts, three parameters, "track-length", "TOT-sum", and "roundness", were introduced. We explain these parameters using the event samples in Figure 4.4.6-4.4.9. The track-length is the measured range of rise-points (blue points in sample) which are the arrival points of electrons and have track-shape information. TOT-sum is the sum of the TOTs of all of the strips. Here, the length between blue and black points for each strip corresponds to the time-over-threshold (TOT). And thus the total number of blue, red, and black points is regarded as the TOT-sum of a event. Roundness is defined by following equations.

$$\text{roundness}_\text{x} = \frac{\sum^{N_\text{x}}(z_\text{risex} - a_\text{x}x - b_\text{x})^2}{N_\text{x}}, \qquad \text{roundness}_\text{y} = \frac{\sum^{N_\text{y}}(z_\text{risey} - a_\text{y}y - b_\text{y})^2}{N_\text{y}},$$
$$\text{roundness} = min(\text{roundness}_\text{x}, \text{roundness}_\text{y}), \qquad (4.3)$$

where N_x and N_y are the number of hit of x and y strips, respectively, z_risex and z_risey are the lowest z corresponding the blue points shown in Figure 4.4.6-4.4.9, (a_x,b_x) and (a_y,b_y) are the best-fit straight line parameters by fitting (x, z_risex) and (y, z_risey) (blue points), respectively.

We checked the energy dependence of the track length, TOT-sum, and roundness for nuclear events by ^{252}Cf and gamma-ray events by ^{137}Cs as shown in Figure 4.4.10-4.4.12. Since the energy loss of an electron is much smaller than that of a nuclei, electron events should be long and scratched. Then, we defined three cuts to discriminate nuclear events of ^{252}Cf-run from electron events of ^{137}Cs-run as followings.

- **length-cut** : track-length[cm] $> 0.6 + 0.004 \times$ E[keV]
  for the rejection of long events. (for example Figure 4.4.7)

- **TOT-sum-cut** : TOT-sum< 50
  for the rejection of scratched events. (for example Figure 4.4.8)

- **roundness-cut** : roundness < 0.05
  for the rejection of the events remained in ^{137}Cs-run shown in Figure 4.4.12. (for example Figure 4.4.9)

The nuclear event shown in Figure 4.4.6 survives these three cuts. These cuts effectively reduce gamma-ray events, while keeping certain efficiency for the nuclear tracks as shown in Figure 4.4.10-4.4.12. In addition, in order to study the effect of roundness-cut, we measured the roundness as a function of the drift length by using external-trigger mode as shown in
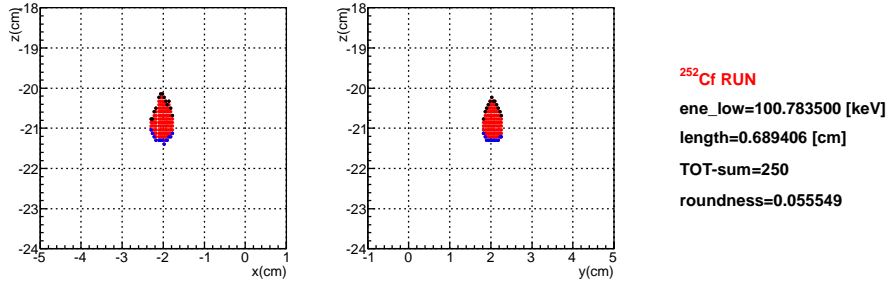
Figure 4.4.6: Track sample measured with ^{252}Cf. Left and right panel shows the $x-z$ and $y-z$ projection of the digitized track acquired by DAQ-mode5. Blue and black points shows the rise-time points and fall-time points. This event survives the length-cut, TOT-sum-cut and roundness-cut.
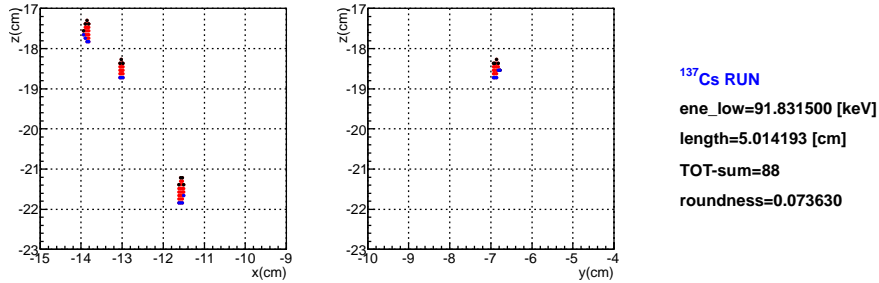
Figure 4.4.7: Track sample measured with ^{137}Cs, cut by length-cut.
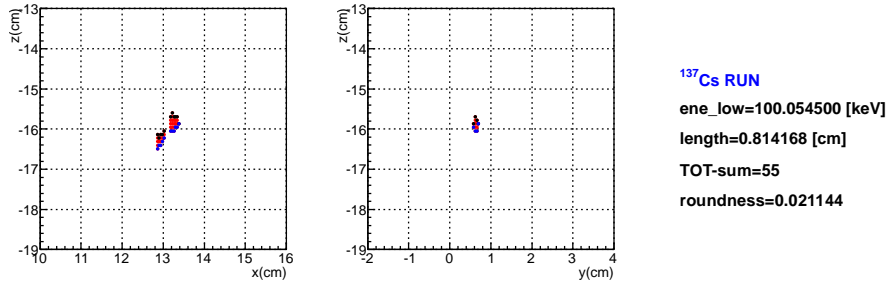
Figure 4.4.8: Track sample measured with ^{137}Cs, cut by TOT-sum-cut.
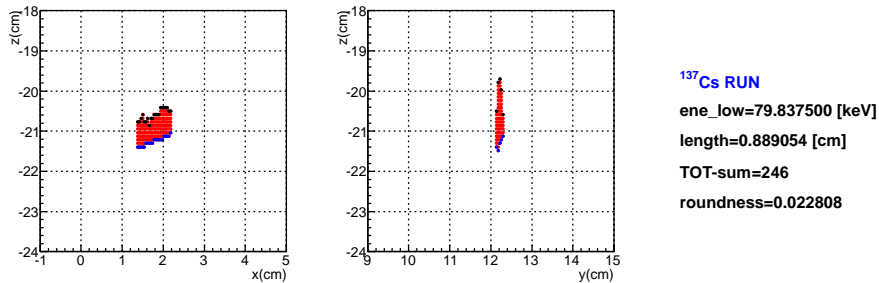
Figure 4.4.9: Track sample measured with ^{137}Cs, cut by roundness-cut.

70
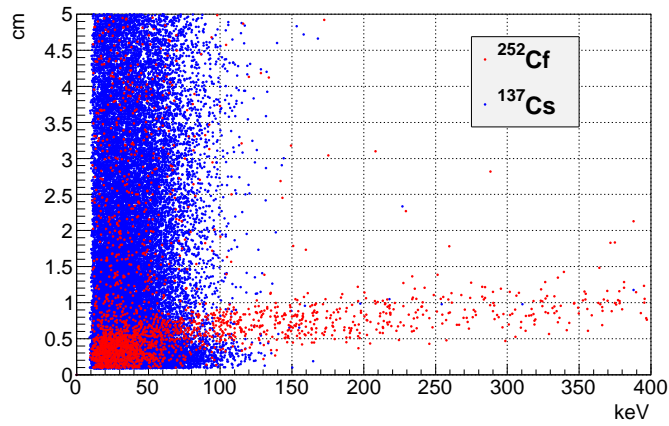
Figure 4.4.10: Energy dependence of the track-length. Red and blue points are measured with ^{252}Cf and ^{137}Cs, respectively.
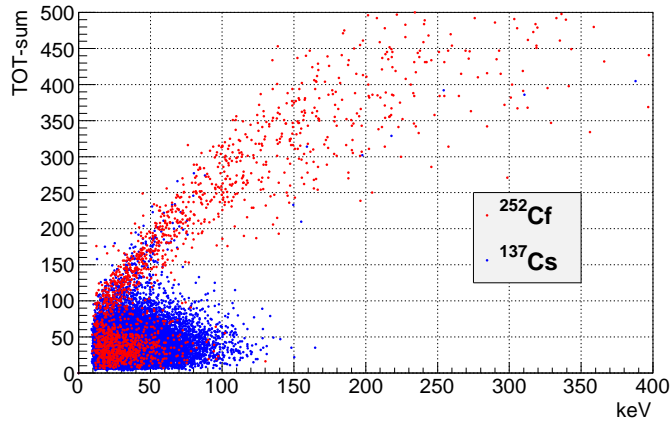
Figure 4.4.11: Energy dependence of the TOT-sum after the length-cut. Red and blue points are same to above figure.
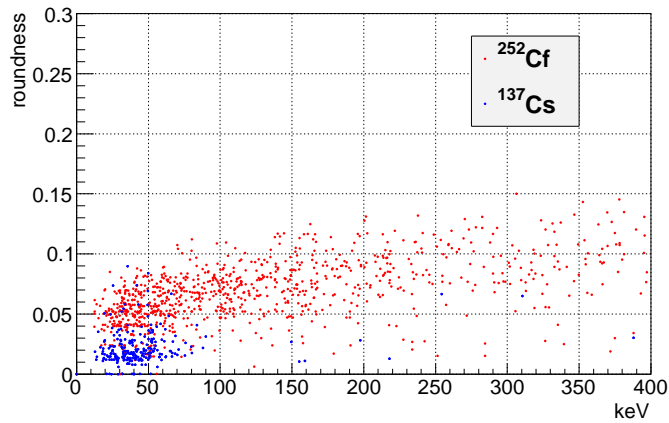
Figure 4.4.12: Energy dependence of the roundness after the length-cut and TOT-sum-cut. Red and blue points are same to above figure.

71
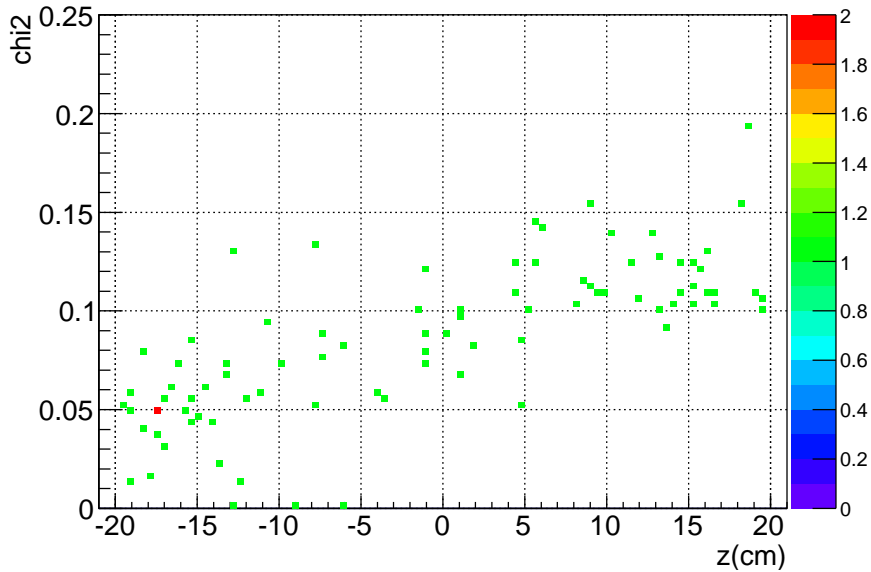
Figure 4.4.13: The measured roundness as a function of drift length.

Figure 4.4.13. From this figure, roundness-cut is found to work as a weak "z-fiducial-cut". The event shown in Figure 4.4.9 might be the background α particle (see also Section 6).

By applying these three cuts, we measured the detection efficiency for the nuclear events and the rejection power for gamma-ray events. The measured detection efficiency of the nuclear recoil events is shown in Figure 4.4.14. We defined the efficiency by dividing the measured energy spectrum after all cuts by the simulated one. An ideal simulation results, not including the detector responses was used as the denominator. In order to cancel the position dependence and measure an overall response of the detector, an averaged spectrum of 6 measurements by placing a ^{252}Cf to 6 places; $(25.5\,\mathrm{cm}, 0\,\mathrm{cm}, 0\,\mathrm{cm})$, $(-25.5\,\mathrm{cm}, 0\,\mathrm{cm}, 0\,\mathrm{cm})$, $(0\,\mathrm{cm}, 25.5\,\mathrm{cm}, 0\,\mathrm{cm})$, $(0\,\mathrm{cm}, -25.5\,\mathrm{cm}, 0\,\mathrm{cm})$, $(0\,\mathrm{cm}, 0\,\mathrm{cm}, 47.5\,\mathrm{cm})$ and $(0\,\mathrm{cm}, 0\,\mathrm{cm}, -47.5\,\mathrm{cm})$ was used. Since the energy deposition of nuclear events (^{19}F and ^{12}C) are sufficiently large , intrinsic detection efficiency of nuclear recoil events should basically be 100%. The discrimination of the threshold and the cut efficiency decrease the efficiency for low energy range. The efficiency does not reaches the intrinsic one in the high energy due to the track-length cut and roundness-cut. We obtained the detection efficiency of nuclear events as 40% at $50\,\mathrm{keV}$.

The detection efficiency of electron events, or the gamma-ray rejection power, was evaluated by irradiating the detector with gamma-rays from a ^{137}Cs source and comparing the data with the simulation results. The detection efficiency for a given energy bin was calculated by dividing the measured event rate with the simulated event rate of the electron with that

energy. Evaluated detection efficiency in the energy bin $50 - 100\,\text{keV}$ was 2.5×10^{-5}. The energy dependence of the electron detection efficiency is shown in Figure 4.4.15.
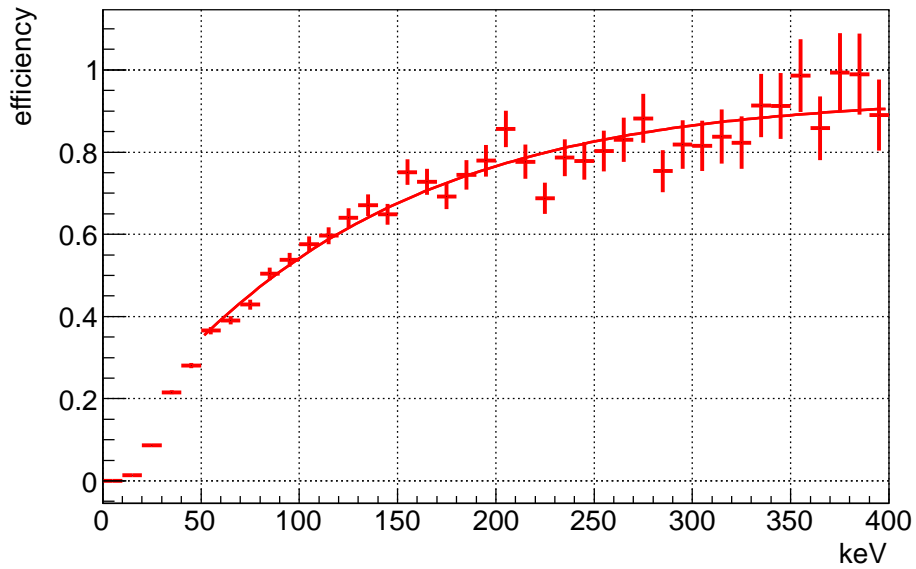
Figure 4.4.14: The detection efficiency of nuclear events.
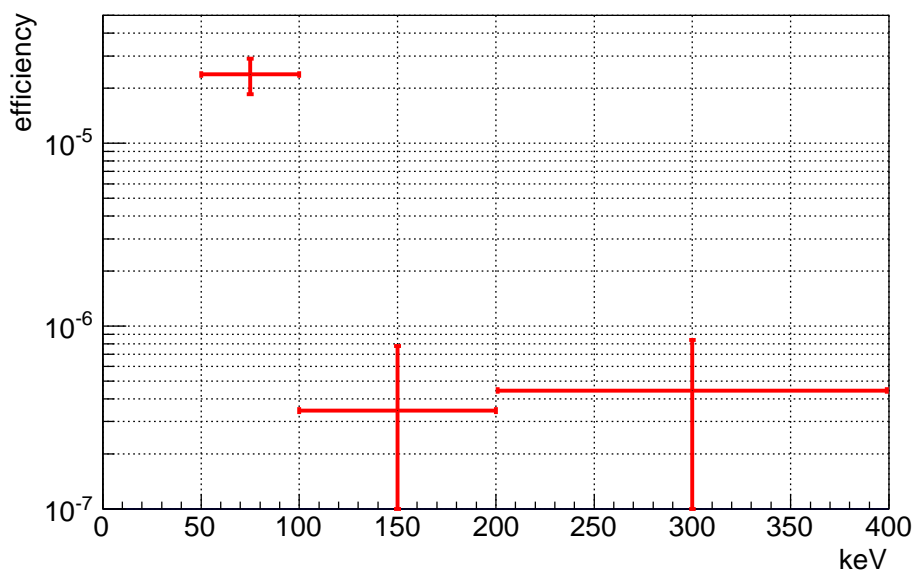
Figure 4.4.15: The detection efficiency of the electron event, or gamma-ray rejection power.

4.4.4 Angular resolution

Angular resolution is the most important parameter for a direction-sensitive detector. We measured the angular resolution of the nuclear tracks using the fast neutrons from a ^{252}Cf source[79]. We evaluated the angular resolution by the comparison of measured and simulated distributions of the recoil angle. The recoil angle is defined in Figure 4.4.16. In order to measure the actual interaction's position, we used the DAQ-mode1 with an external-trigger mode.

First, we measured the direction dependence of the detection efficiency, or the response to isotropic radiation, for nuclear tracks. We irradiated the detector with fast neutrons from the ^{252}Cf source placed at $(25.5\,\text{cm}, 0\,\text{cm}, 0\,\text{cm})$, $(-25.5\,\text{cm}, 0\,\text{cm}, 0\,\text{cm})$, $(0\,\text{cm}, 25.5\,\text{cm}, 0\,\text{cm})$, $(0\,\text{cm}, -25.5\,\text{cm}, 0\,\text{cm})$, $(0\,\text{cm}, 0\,\text{cm}, 47.5\,\text{cm})$ and $(0\,\text{cm}, 0\,\text{cm}, -47.5\,\text{cm})$. We confirmed that we can emulate isotropic recoil (standard deviation is 23%) with a weighted sum of these six measurements by Geant4 simulations. Then we calculated the elevation angle and the azimuth angle as shown in Figure 4.4.17, where these angle are schematically shown in Figure 4.1.2.
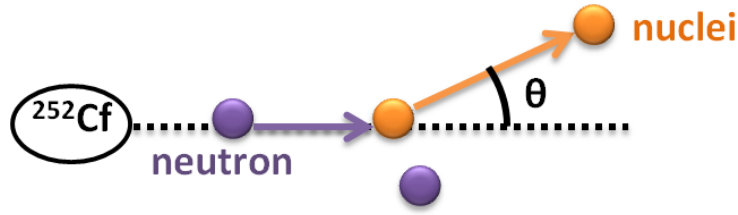
Figure 4.4.16: The schematic view of nuclear recoil. θ is the recoil angle.
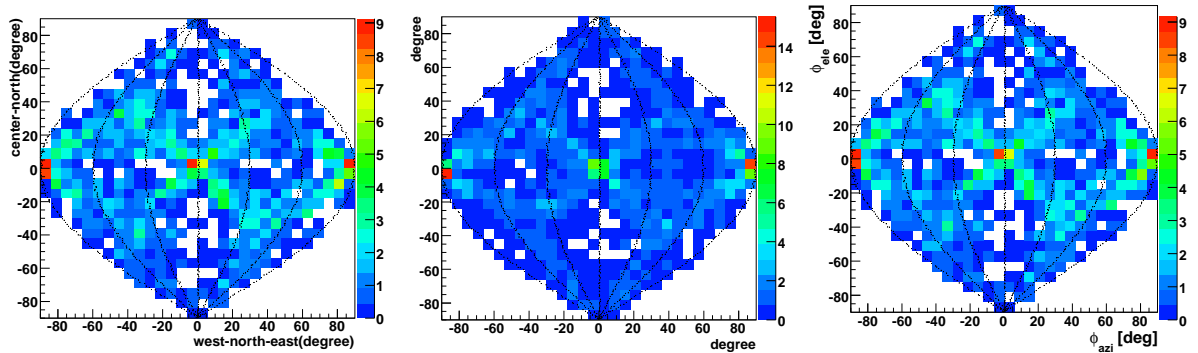
Figure 4.4.17: Direction-dependent efficiency, or the response to isotropic irradiation, for angular resolution measurement range measured with DAQ-mode1 and external-trigger mode. The energy range of left, center, and right figures are $50-100\,\text{keV}$, $100-200\,\text{keV}$, and $200-400\,\text{keV}$, The vertical axis is the elevation angle and the horizontal axis is the azimuth angle. Color scale is counts normalized by the mean value.
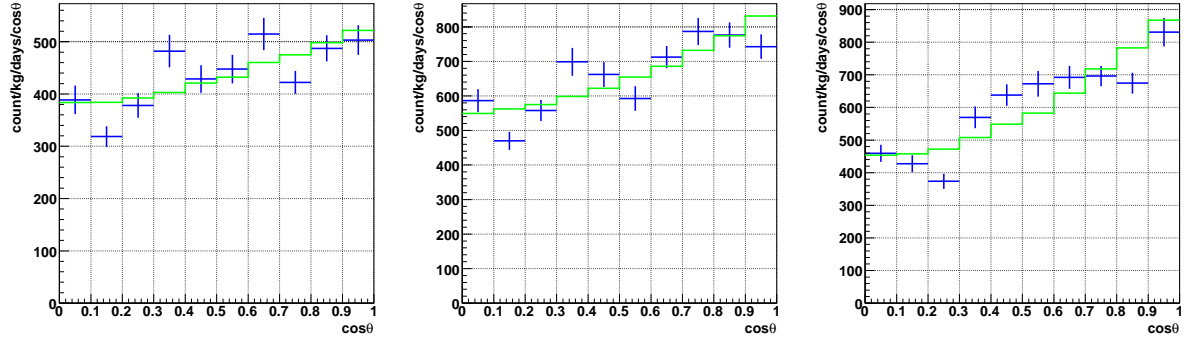
Figure 4.4.18: $|\cos\theta|$ distribution of the scattering angle in nuclear recoil events that occur by irradiation with neutrons from ^{252}Cf. The energy range of left, center, and right figures are $50 - 100\,\text{keV}$, $100 - 200\,\text{keV}$, and $200 - 400\,\text{keV}$, respectively. Measured and simulated distributions are shown by blue and green histograms respectively.
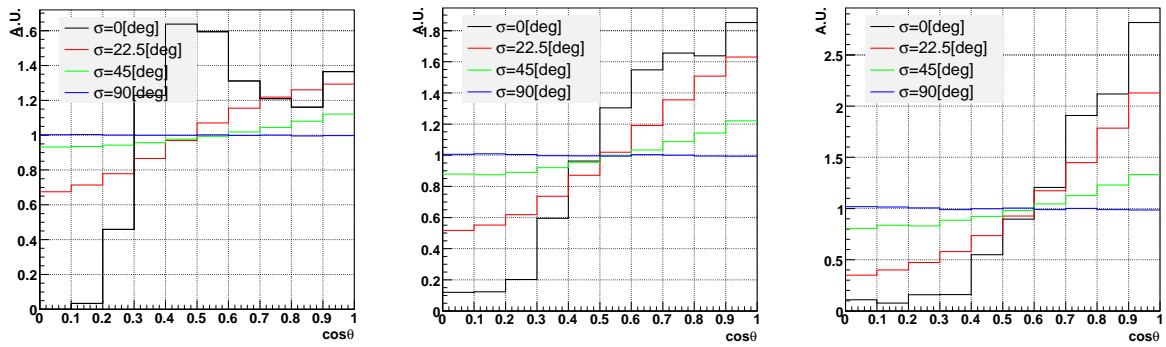
Figure 4.4.19: Simulated $|\cos\theta|$ distributions assuming angular resolutions of $0°$(black), $22.5°$(red), $45°$(green), $90°$(blue). The energy range of left, center, and right figures are $50 - 100\,\text{keV}$, $100 - 200\,\text{keV}$, and $200 - 400\,\text{keV}$, respectively.
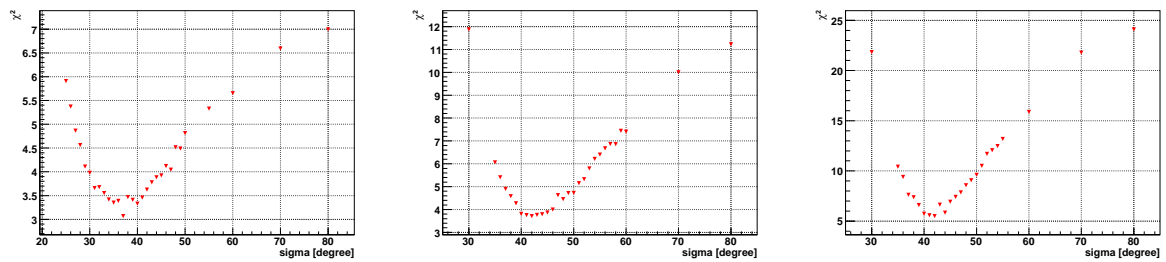
Figure 4.4.20: χ^2 values obtained between measured and simulated $|\cos\theta|$ distributions as a function of angular resolution. The energy range of left, center, and right figures are $50 - 100\,\text{keV}$, $100 - 200\,\text{keV}$, and $200 - 400\,\text{keV}$, respectively.

75

As a next step, we measured the recoiled nuclear tracks by neutrons from the ^{252}Cf source, at six positions, given above. Measured events were weighted by the direction-dependent efficiency and thus corrected $|\cos\theta|$ is obtained The observed $|\cos\theta|$ distribution is shown by the blue histogram in Figure 4.4.18. To determine the angular resolution, we simulated the neutron-nucleus scatterings assuming several angular resolutions as shown in Figure 4.4.19, and compared them to the measured distributions. We calculated a χ^2 of $|\cos\theta|$ distribution for each simulated angular resolution, and the χ^2 values plotted against the angular resolutions are shown in Figure 4.4.20. We obtained the minimum $\chi^2(\equiv \chi^2_{min})$ point using a fitted polynomial function. We then set 1σ error for the angular resolution as the range determined from $[\chi^2_{min} : \chi^2_{min} + 1]$ [80].

We measured the angular resolutions in each energy ranges. The result is shown in Figure 4.4.21. By using the low pressure gas of 0.1 atm, we were able to measure the angular resolution in the $50 - 100$ keV energy range in addition to other energy ranges.
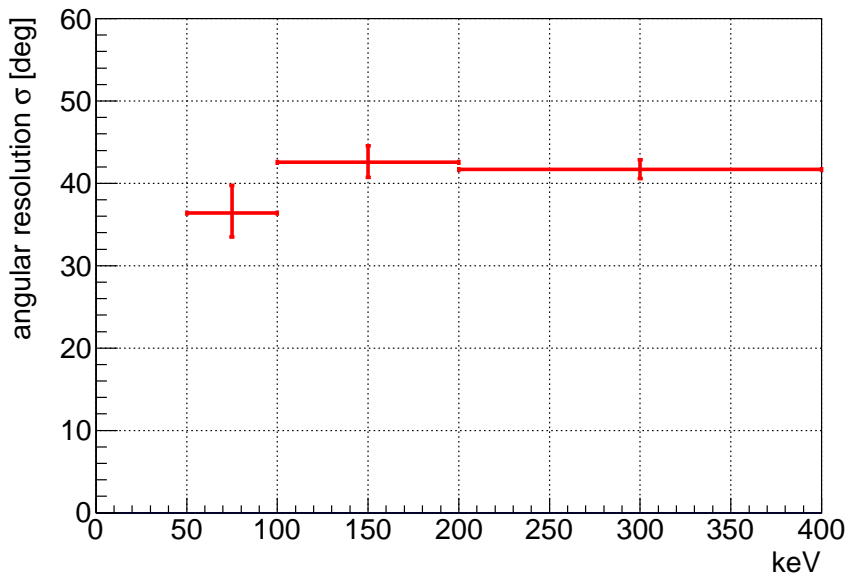
Figure 4.4.21: Obtained angular resolution for each energy.

4.4.5 Direction dependent efficiency

We measured the overall direction-dependent efficiency in the $50 - 100$ keV range by using the DAQ-mode5 with a self-trigger. The detector was irradiated with the neutrons from the ^{252}Cf source placed at $(25.5\,\text{cm}, 0\,\text{cm}, 0\,\text{cm})$, $(-25.5\,\text{cm}, 0\,\text{cm}, 0\,\text{cm})$, $(0\,\text{cm}, 25.5\,\text{cm}, 0\,\text{cm})$, $(0\,\text{cm}, -25.5\,\text{cm}, 0\,\text{cm})$, $(0\,\text{cm}, 0\,\text{cm}, 47.5\,\text{cm})$ and $(0\,\text{cm}, 0\,\text{cm}, -47.5\,\text{cm})$. We confirmed that we

can emulate isotropic recoil (standard deviation is 23%) with a weighted sum of these six measurements by Geant4 simulations. Figure 4.4.22 shows the calculated distribution of the elevation angle θ_{ele} and the azimuth angle ϕ_{ele}. We can see that the efficiency is high around $(\theta_{\mathrm{ele}}, \phi_{\mathrm{azi}}=0°, 0°)$ and $(0°, \pm 90°)$. Since $\phi_{\mathrm{azi}} = 0°$ and $\phi_{\mathrm{azi}} = \pm 90°$ represent the direction of the anode/cathode strips as shown in Figure 4.1.2, it is seen that the recoil direction tends to be detected as that along the anode/cathode strips. Also, there are higher points along the diagonal lines from the direction of the anode and the cathode strips. This is because the current tracking algorithm tends to measure the diffused tracks in such directions. Measured direction-dependent efficiency is used for weighting the expected direction distribution of recoil nuclear track scattered by the dark matter for the direction analysis.
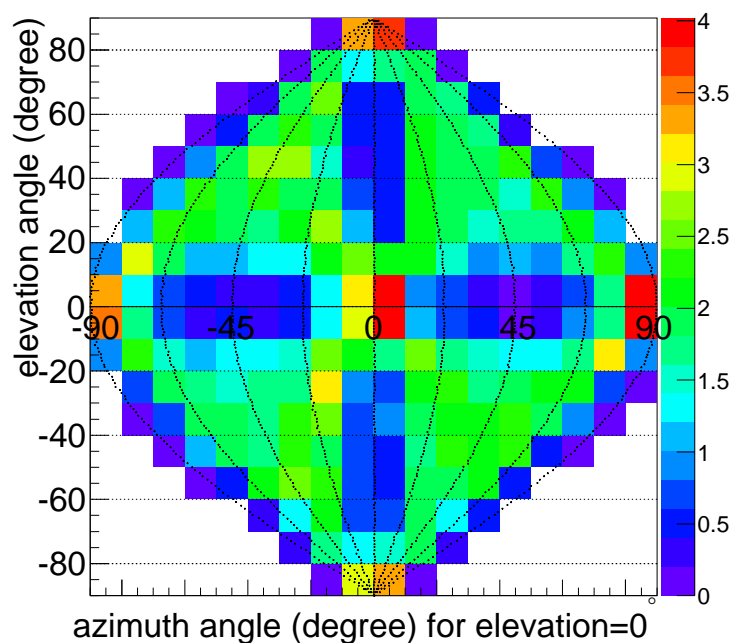
Figure 4.4.22: Direction-dependent efficiency in the $50-100\,\mathrm{keV}$ range measured with DAQ-mode5 and the self trigger. The vertical axis is the elevation angle and the horizontal axis is the azimuth angle. Color scale is normalized counts by the mean value.

Chapter 5

Experiment

A direction-sensitive dark matter detector,NEWAGE-0.3b', was developed to improve the sensitivity by one order of magnitude as described in the previous chapter. The detector was set in the Kamioka underground laboratory in March, 2013, and a direction sensitive dark matter search experiment was performed from July, 2013. The measurement properties and the results are described in this chapter.

5.1 Dark matter search at Kamioka mine

A direction-sensitive dark matter search experiment was performed with the NEWAGE-0.3b' detector in an underground laboratory in Kamioka mine. The NEWAGE-0.3a' detector was placed in Laboratory B, Kamioka Observatory located at $2700 \, \mathrm{m}$ water equivalent (w.e.) underground (36.25' N, 137.18' E). The fluxes of environmental backgrounds; cosmic-ray muons, neutrons, and gamma-rays, in Kamioka are listed in Table 5.1.1. Since the μ-TPC is set in a vacuum vessel, environmental radon gas is blocked and can be ignored.

particle	flux in Kamioka	flux in surface	ref
cosmic-ray muons	$\sim 6 \times 10^{-8} \, /\mathrm{cm}^2/\mathrm{sec}/\mathrm{sr}$	$\sim 1 \times 10^{-3} \, /\mathrm{cm}^2/\mathrm{sec}/\mathrm{sr}$	[81]
thermal neutrons $(< 0.5 \, \mathrm{eV})$	$8.26 \times 10^{-6} \, /\mathrm{cm}^2/\mathrm{sec}$	$1.4 \times 10^{-3} \, /\mathrm{cm}^2/\mathrm{sec}$	[82]
non-thermal neutrons $(> 0.5 \, \mathrm{eV})$	$1.15 \times 10^{-5} \, /\mathrm{cm}^2/\mathrm{sec}$	$1.3 \times 10^{-2} \, /\mathrm{cm}^2/\mathrm{sec}$	[82]
fast neutrons $(> 500 \, \mathrm{keV})$	$2.06 \times 10^{-6} \, /\mathrm{cm}^2/\mathrm{sec}$		[82]
gamma-rays	$\sim 4 \times 10^{-3} \, /\mathrm{cm}^2/\mathrm{sec}$		[83]

Table 5.1.1: The flux of backgrounds in Kamioka underground laboratory.

Any radiation shield was not set mainly for an easy access to the detector. Also it was expected from previous measurements that the environmental background is still lower than

the internal background even without any shield. The μ-PIC plane of the μ-TPC was placed vertically and the z-axis is aligned to the direction of S30°E. The run properties are summarized in Table 5.1.2. The first sub-run started by the gas filling on July 17th, followed by the dark matter run from July 20th to August 11th with a 17.1 live-days. The second sub-run, started on October 17th, accumulated data from October 19th to November 12th resulting a 14.5 live-days dark matter exposure. The target gas was CF_4 at 0.1 atm in the fiducial volume of $275\,\mathrm{cm}^3$. Thus exposure of the sub-runs are $0.177\,\mathrm{kg \cdot days}$ and $0.150\,\mathrm{kg \cdot days}$, making a total exposure of $0.327\,\mathrm{kg \cdot days}$. The time dependencies of the drift velocity and the gas gain were measured as listed in Table 5.1.3, by the same method described in Section 4.4. The energy and track length are obtained using these calibration factors from the measured raw data.

RUN ID	gas filling	period	live time	mass	exposure
RUN14-1	2013/07/17	$2013/7/20 - 8/11$	17.1 days	10.36 g	$0.177\,\mathrm{kg \cdot days}$
RUN14-2	2013/10/17	$2013/10/19 - 11/12$	14.5 days	10.36 g	$0.150\,\mathrm{kg \cdot days}$
RUN14			31.6 days		$0.327\,\mathrm{kg \cdot days}$

Table 5.1.2: Conditions of underground measurement RUN14.

	measured date	gain	V_{drift} [cm/μsec]
	RUN14-1		
cal-run	7/18-20	2500	8.9
DM-run	7/20-8/11		
cal-run	8/20-21	2500	8.5
	RUN14-2		
cal-run	10/17-19	2500	9.5
DM-run	10/19-10/26		
cal-run	11/1-2	2500	9.5
DM-run	11/2-12		
cal-run	11/12-14	2350	9.5

Table 5.1.3: Measured values of gas gain and drift velocity during RUN14.

The data was cut by the fiducial-cut first, then the three cuts defined in Section 4.4.3 were applied. Figure 5.1.1-5.1.4 show the energy dependence of the length, the TOT-sum and the roundness of the event after each cut. Figure 5.1.4 shows the final sample for the dark matter analysis and its spectrum is shown in Figure 5.1.5 by the red histogram. Energy spectra at each cut step are also shown in Figure 5.1.5 and is used for analysis of dark matter limit. The effect of the length-cut and the TOT-sum-cut is remarkable for low energy region, where gamma-rays are mainly rejected. The roundness-cut affects the whole energy range, particularly in
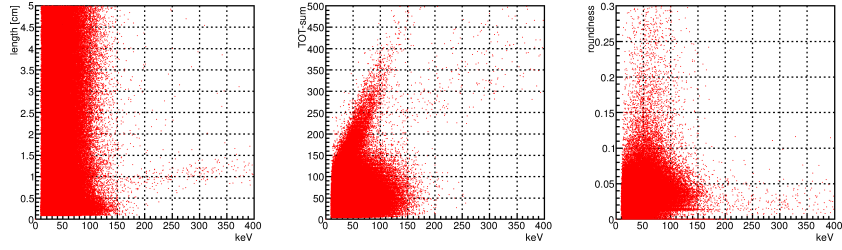
Figure 5.1.1: Energy dependence of the length (left), the TOT-sum (center), and the roundness (right). The events are cut by only fiducial-cut. These events correspond to the black line in Figure 5.1.5.
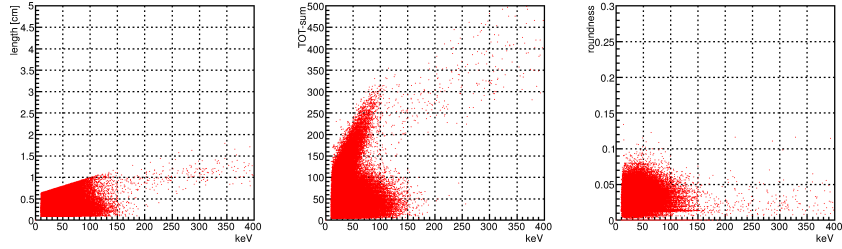
Figure 5.1.2: Energy dependence of the length (left), the TOT-sum (center), and the roundness (right). The events are cut by fiducial-cut and length-cut. These events correspond to the purple line in Figure 5.1.5.
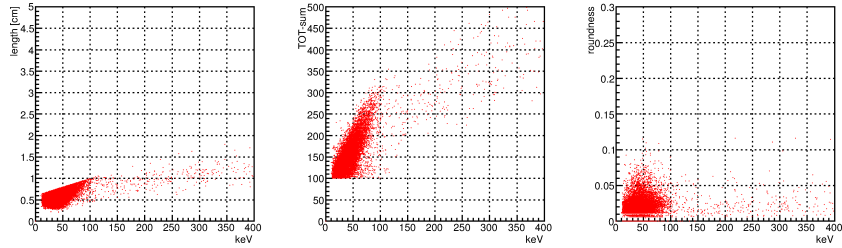
Figure 5.1.3: Energy dependence of the length (left), the TOT-sum (center), and the roundness (right). The events are cut by fiducial-cut, length-cut and TOT-sum-cut. These events correspond to the blue line in Figure 5.1.5.
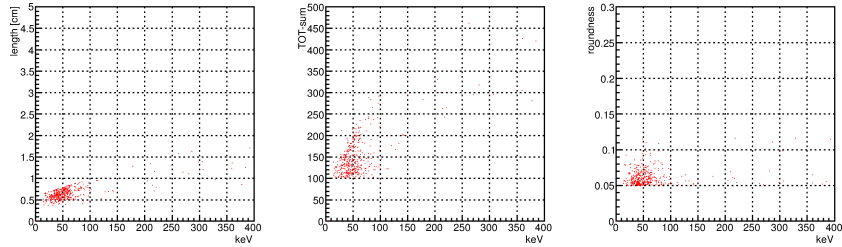
Figure 5.1.4: Energy dependence of the length (left), the TOT-sum (center), and the roundness (right). The events are final sample with the fiducial-cut, length-cut, TOT-sum-cut and roundness-cut. These events correspond to the red line in Figure 5.1.5.

$100 - 400$ keV range. It suggests the existence of background from $-z$ (μ-PIC or GEM) and roundness-cut is effective to cut such events. Details of the background study is described are Section 6.
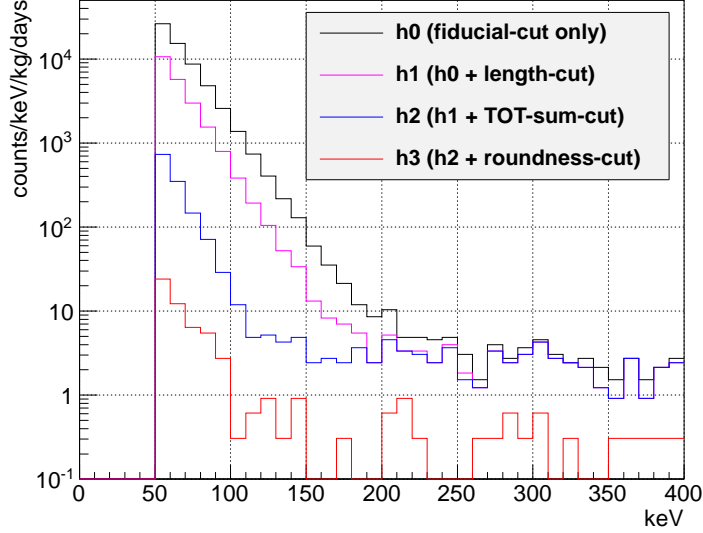
Figure 5.1.5: Obtained energy spectra in Kamioka RUN-14. Black line is the spectrum with only the fiducial-cut. As show in the legend, pink, blue, and red histograms are the energy spectra at each cut-step described in Section 4.4.3, and correspond to the events shown in Figure 5.1.1-5.1.4.

By taking into account the detection efficiency (Figure 4.4.14), we obtained the "final" energy spectrum of RUN14 shown in Figure 5.1.6 together with the result from previous measurement, RUN5. We plotted the energy spectrum from 50 keV for RUN14 because the angular resolution down to 50 keV was measured as described in Section 4.4.4. Compared to the RUN5, the background rate of RUN14 is reduced by $\sim 1/10$ in the energy range of $100 - 400$ keV. Obtained nuclear direction plots and corresponding $|\cos\theta_{\mathrm{cygnus}}|$ distribution for the $50 - 400$ keV energy range are shown in Figure 5.1.7 and Figure 5.1.8, respectively. The $|\cos\theta_{\mathrm{cygnus}}|$ distributions of the lowest 6 bins, $50 - 60$ keV to $100 - 110$ keV are shown separately in Figure 5.1.9. The angle θ_{cygnus} is the angle between the WIMP-wind direction and the measured direction of a recoil nucleus. If we are observing the dark matter, the strong signal from the Cygnus direction is expected. Obtained direction distribution was roughly isotropic, and it can be said that the background is still dominating the results.
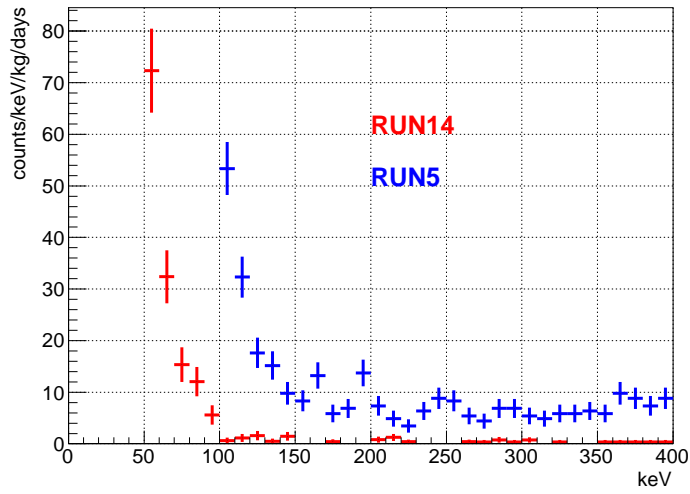
Figure 5.1.6: Obtained energy spectrum in Kamioka RUN-14 (red points). Blue points are the results of previous measurements RUN-5[58, 83]. Detection efficiency was taken into account.
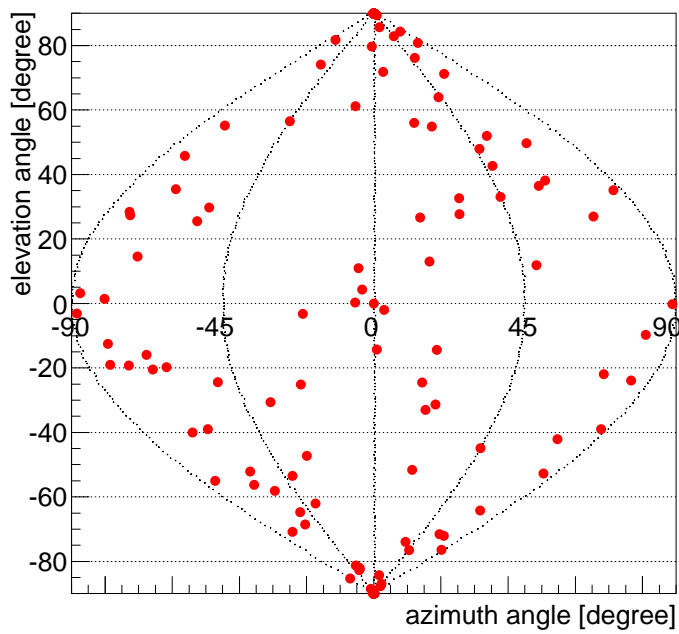
Figure 5.1.7: Obtained direction of the nuclear tracks of RUN-14 in the energy range of $50 - 400\,\mathrm{keV}$

82
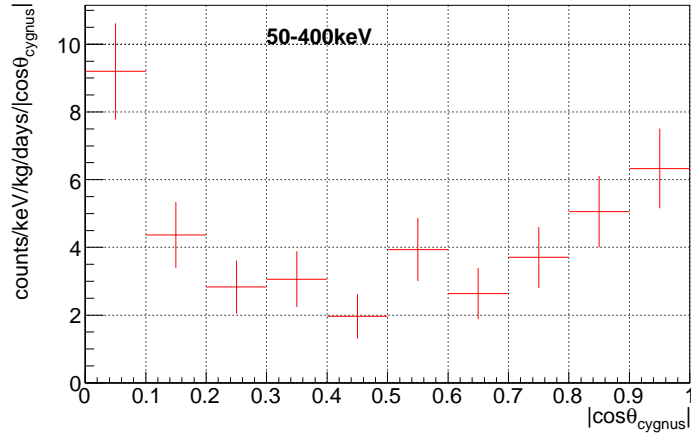
Figure 5.1.8: Obtained $|\cos\theta_{\mathrm{cygnus}}|$ distribution of RUN-14 in the energy range of $50 - 400\,\mathrm{keV}$
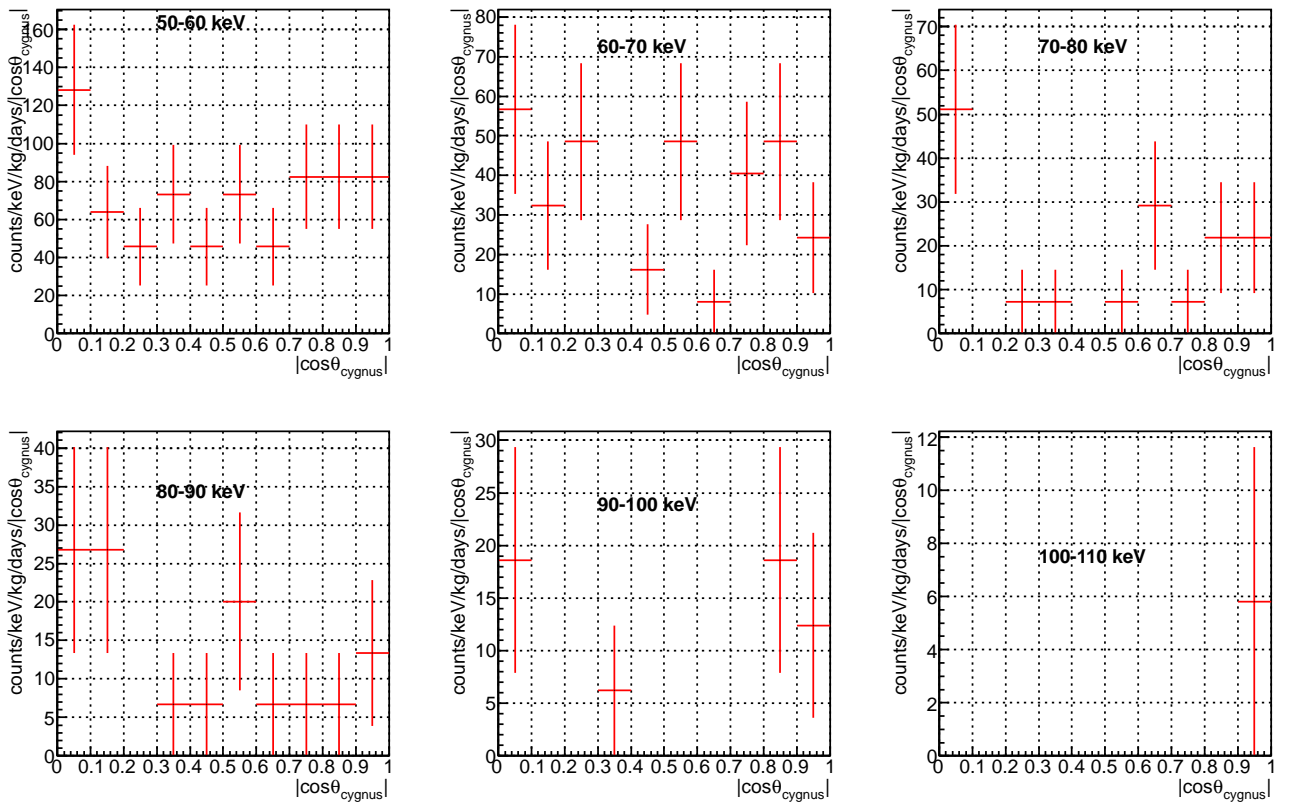
Figure 5.1.9: Obtained $|\cos\theta_{\mathrm{cygnus}}|$ distribution of RUN-14 of the lowest 6 bins.

83

5.2 Dark matter limits

We derived the limits of the SD cross-section $\sigma_{\chi-\mathrm{p}}^{\mathrm{SD}}$ by a direction-sensitive method by comparing the measured $|\cos\theta_{\mathrm{cygnus}}|$ distribution with a calculated one. In the calculation, we used the astrophysical parameters, nuclear parameters, and detector responses listed in Table 5.2.1. The calculation includes nuclear quenching factor shown in Figure 3.2.4 and detector responses: energy resolution, angular resolution and direction-dependent efficiency described in Section 4.4. Because of the small statistics, measured and calculated $|\cos\theta_{\mathrm{cygnus}}|$ shown in Figure 5.1.9 distributions were rebined into 2-bin as shown in Figure 5.2.1. We obtained the direction-sensitive exclusion limits by the following procedure.

STEP 1 Prepare the measured $|\cos\theta_{\mathrm{cygnus}}|$ distributions of the energy bin of interest (the lowest bin is $50 - 60\,\mathrm{keV}$, bin width is $10\,\mathrm{keV}$, at least one event in the bin).

STEP 2 Renormalize the measured $|\cos\theta_{\mathrm{cygnus}}|$ distribution. The unit changes from [counts/keV/kg/days] to [count] by using the live time, fiducial mass, and the detection efficiency.

STEP 3 Calculate the expected $|\cos\theta_{\mathrm{cygnus}}|$ distribution by WIMPs by taking the projection of calculated angle-energy distribution (Figure 2.4.4). Here, the WIMP mass is assumed and the quenching factor, the energy resolution and the astrophysical and nuclear parameters listed in Table 5.2.1 are taken account of. Then the distribution is smared with the angular resolution of $40°$ and direction-dependent efficiency (Figure 4.4.22) by Monte Carlo method assuming random ϕ_{cygnus}, the azimuth angle when the cygnus direction is a zenith direction.

STEP 4 Renormalize the expected $|\cos\theta_{\mathrm{cygnus}}|$ distribution. The unit changes from [counts/keV/kg/days] to [count] by using the live time and the fiducial mass.

STEP 5 Compare the measured and expected $|\cos\theta_{\mathrm{cygnus}}|$ distribution by scanning the cross section $\sigma_{\chi-\mathrm{p}}^{\mathrm{SD}}$. To evaluate the χ^2 value with the Poisson error, we used count-base distribution obtained in STEP 2 and STEP 4. If the minimum $\chi^2/\mathrm{d.o.f.}$ is larger than $\chi^2/\mathrm{d.o.f.}$ of 90%C.L. exclusion level (*i.e.* 2.7 for d.o.f. $= 1$), the cross section is taken as a direction-sensitive dark matter limit. If the minimum $\chi^2/\mathrm{d.o.f.}$ is less than $\chi^2/\mathrm{d.o.f.}$ of 90%C.L. exclusion level, we evaluated the 90%C.L. upper limit by increasing the cross-section when the χ^2 value becomes more than $\chi^2/\mathrm{d.o.f.}$ of 90%C.L. exclusion level.

STEP 6 Repeat STEP 3-5 by changing WIMP mass.

STEP 7 Repeat STEP 1-6 by changing the energy bin, and take the minimum cross-sections for each WIMP mass.

WIMP velocity distribution	Maxwellian
Maxwellian velocity dispersion	$v_0 = 220\,\mathrm{km/sec}$
Escape velocity	$v_0 = 650\,\mathrm{km/sec}$
Local halo density	$\rho_{\mathrm{DM}} = 0.3\,\mathrm{GeV/c^2/cm^3}$
Spin factor of $^{19}\mathrm{F}$	$\lambda^2 J(J+1) = 0.647$
Energy resolution at $50\,\mathrm{keV}$	$7.8\,\mathrm{keV}$
Angular resolution at $50-100\,\mathrm{keV}$	$40°$
direction-dependent efficiency at $50-100\,\mathrm{keV}$	Figure 4.4.22

Table 5.2.1: Astrophysical parameters, nuclear parameters, and detector responses used to derive the WIMP-proton limit.

Figure 5.2.1 show the example of measured and calculated $|\cos\theta_{\mathrm{cygnus}}|$ distributions, again normalized into $[\mathrm{counts/keV/kg/days/}|\cos\theta_{\mathrm{cygnus}}|]$ unit. The left figure is the case of excluding the best-fit calculated $|\cos\theta_{\mathrm{cygnus}}|$ distribution for $50\,\mathrm{GeV}$ of WIMP mass with sufficient statistics of $50-60\,\mathrm{keV}$ energy bin. The right figure is the case of low of statistics, thus the upper limit of cross section was evaluated by increasing the cross section when the $\chi^2/\mathrm{d.o.f.}$ value becomes more than that of 90%C.L. exclusion level. Since the steeper energy spectrum is expected for the lower WIMP mass as shown in Figure 2.3.4, the lower energy range limit the low-mass WIMP. In this measurement, the energy bin of $50-60\,\mathrm{keV}$ limits the low-mass WIMPs ($\leq 70\,\mathrm{GeV}$), and the that of $100-110\,\mathrm{keV}$ limits the high-mass WIMPs ($\geq 100\,\mathrm{GeV}$).
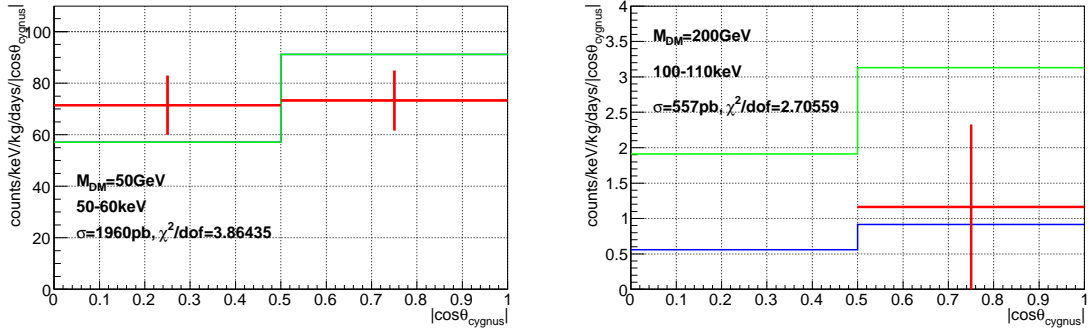
Figure 5.2.1: $\cos\theta_{\mathrm{cygnus}}$ distributions win the energy range of $50-60\,\mathrm{keV}$ (left) and $100-110\,\mathrm{keV}$ (right). Red histograms are measured $|\cos\theta_{\mathrm{cygnus}}|$ distribution. Blue and green lines are calculated $\cos\theta_{\mathrm{cygnus}}$ distribution assuming WIMP-wind model with mass of WIMP $50\,\mathrm{GeV}$ (left) and $200\,\mathrm{GeV}$ (right). Blue line is the best-fit. Green line is the $|\cos\theta_{\mathrm{cygnus}}|$ distribution when the model is excluded by 90%C.L..

Figure 5.2.2 shows the limits of SD cross section, $\sigma_{\chi-\mathrm{p}}^{\mathrm{SD}}$, as a function of mass of WIMP M_χ. The regions above the curves are excluded. Red solid line is a result of directional method in this work. Blue thick dotted line is a result of conventional method (spectrum-only) for
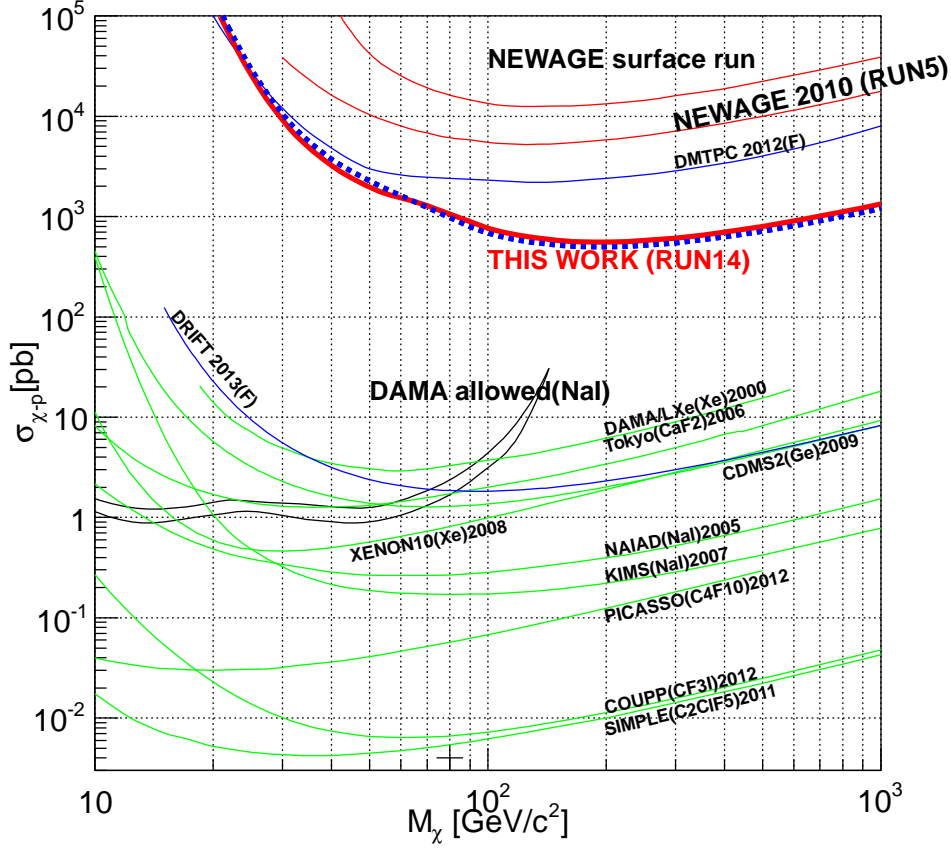
Figure 5.2.2: Limits of SD cross section, $\sigma^{\mathrm{SD}}_{\chi-\mathrm{p}}$, as a function of mass of WIMP mass M_χ. Red thick solid line is the result of a directional method in this work. Blue thick dotted line is a result obtained with the conventional method for reference. Red thin lines labeled "NEWAGE surface run" and "NEWAGE 2010 (RUN5)" are previous results measured at surface and Kamioka, respectively[83]. Allowed region (DAMA[39]) and upper limits of other experiments are shown for comparison. Green lines are limits set by liquid or solid detectors, blue lines are the limits set by gas detectors with conventional analysis.

reference. The largest systematic error is arised from the uncertainty of the energy resolution. Since the shape of the expected energy spectrum is exponential (Figure 2.1.2), the lower limit is obtained for the larger energy resolution. As described in the Section 4.4.2, the energy resolution is sum of $\sigma_{\mathrm{uni}} = 20 \pm 5\%$ and $\sigma_{\mathrm{noise}} = 2\,\mathrm{keV}$. In order to obtain the conservative limit, $\sigma_{\mathrm{uni}} = 15\%$ is used for the analysis (total energy resolution is $7.8\,\mathrm{keV}$ for $50\,\mathrm{keV}$). It should be noted that the direction-sensitive analysis and conventional method provide similar limits with this low statistic results. Figure 5.2.3 shows the calculated $\chi^2/\mathrm{d.o.f.}$ values with the WIMP model (red), and calculated that with the flat-background model (black). The minimum χ^2 values are shown in the $20 - 70\,\mathrm{GeV}$ mass region. As for the $100 - 1000\,\mathrm{GeV}$ mass region,

we evaluated the 90% C.L. upper limit by increasing the cross-section χ^2 values until exceeding 2.7. We obtained a 90% C.L. SD WIMP-proton cross section upper limit of 557 pb for WIMP mass of 200 GeV. This result marked new best sensitivity record for a SD WIMP search with the direction-sensitive method, although its sensitivity is still worse than that of the frontier of SD WIMP searches with other methods.
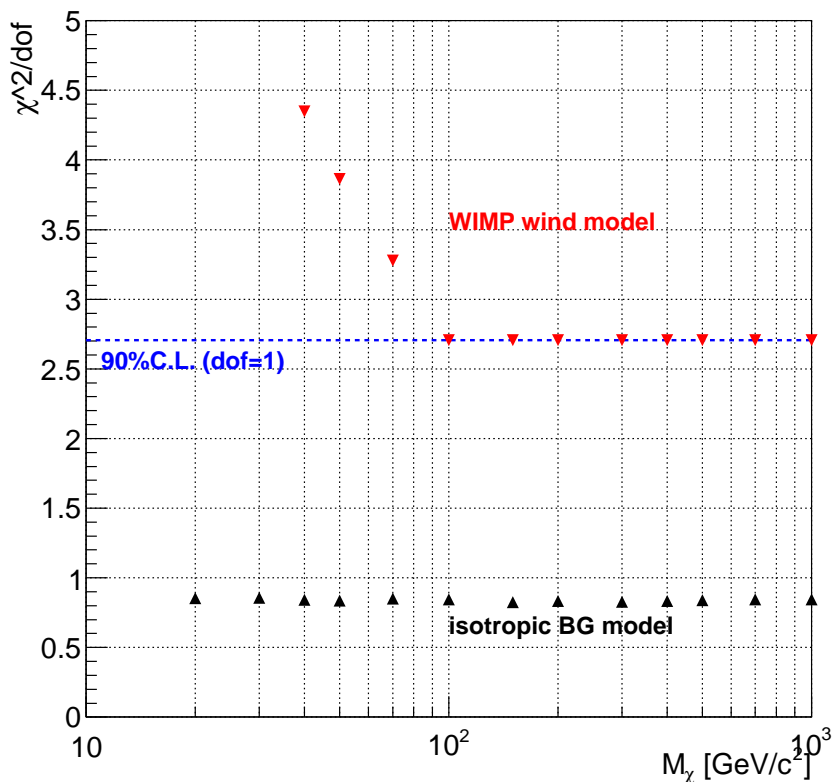
Figure 5.2.3: χ^2 values in comparison with measured $|\cos\theta_{\mathrm{cygnus}}|$ and that of models. Red points are χ^2 values with the WIMP wind model. Black points are the minimum χ^2 values with the isotropic background model.

Chapter 6

Discussion

A dark matter search in Kamioka mine has been carried out with the NEWAGE-0.3b' detector, and then a new lower upper limit for the WIMP-proton SD interaction than that of the previous run has been obtained. However, further reduction of background is necessary to reach the MSSM region. In addition, the origin of remaining background is studied in detail.

Radioactive contaminations within the detector components are well-known background sources in rare event measurements. The radioactive contaminations emit γ-rays, β-rays and α-rays. In our case, γ-rays and β-rays were rejected with a rejection power of $\sim 10^{-5}$, but α-rays cannot be discriminated from nuclear recoils around $50 \, \text{keV}$ region. Dominant natural radioactive isotopes contaminated in most of the materials are ^{238}U, ^{232}Th and ^{40}K. There are several α-decays and β-decays associated with γ-ray emissions in the U-chain and the Th-chain as shown in Figure 6.0.1. ^{40}K decays with a β-ray and a γ-ray. These isotopes wouold be contaminated in most of the material in the detector components such as metal, plastic and glass-fiber. In addition, radon in U-chain and Th-chain emanates from the material as gas. Therefore, radon and radon progeny, which are the isotopes below radon as shown in Figure 6.0.1, might exist not only in the detector components but also in the gas volume. Although α-particles emitted from the U/Th-chains have an initial energy of more than 4 MeV, they sometimes deposit only their partial energy in the detection volume and make background events of $\sim 50 \, \text{keV}$.

The final goal of this chapter is to identify the background sources in the energy range relevant to the dark matter search; $i.e.$ $50 - 400 \, \text{keV}$ energy range. Measured energy spectra are shown in Figure 6.0.2. The red spectrum is the final one with all the cut applied and the blue spectrum is the one with all but the roundness-cut applied. Since the roundness-cut has a large uncertainty in terms of the cut efficiencies for short-drift events, the understanding of the blue spectrum is studied instead of that of the red one. At first, I mention on the results
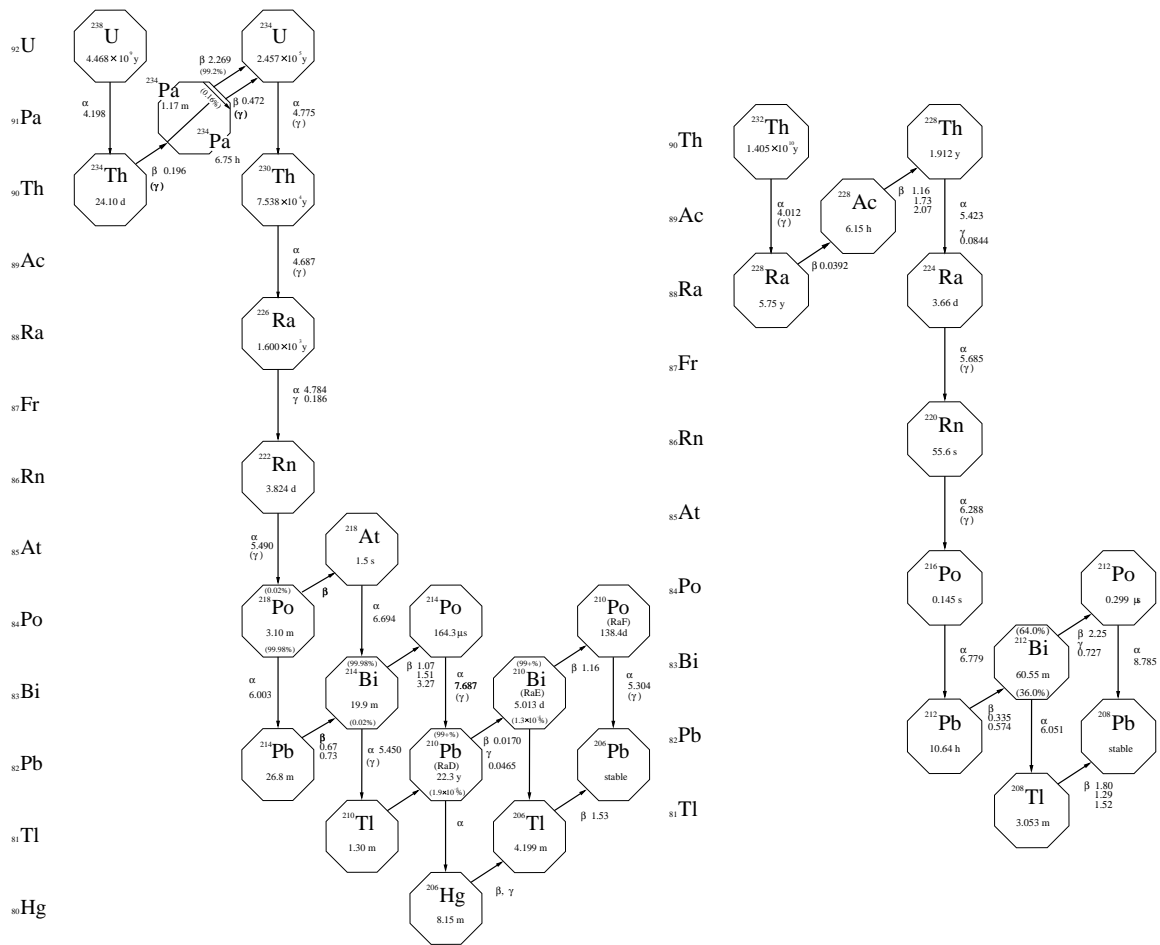
Figure 6.0.1: Decay chain of ^{232}Th and ^{238}U.

on the high energy background shown in Figure 6.0.3 as an "independent input". The high-energy spectrum consist of a peak-like component and a continuous component. By comparing the dependence of the measured track length on energy to that of calculated one by SRIM, background events of the high energy are considered to be due to α particles as shown in Figure 6.0.3. When the directional distribution is concentrated to the higher at $\pm z$ direction, with a small fraction of isotropic component. The background sources of the high energy events will be identified quantatively in Section 6.1, then the background identification in the low energy range is going to be discussed in Section 6.2.
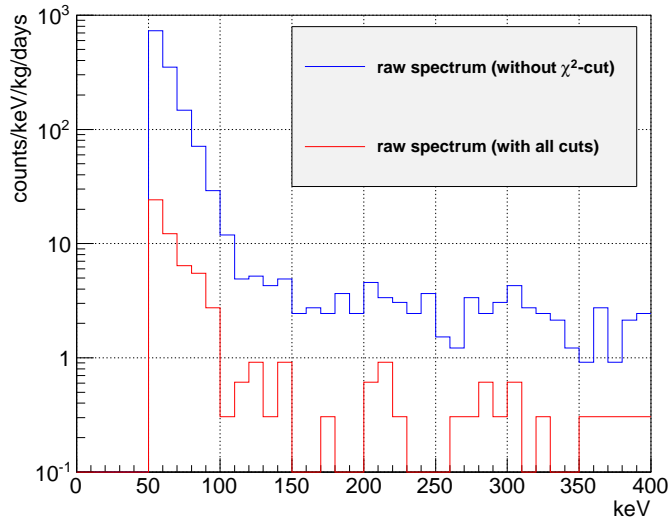
Figure 6.0.2: Obtained energy spectrum of RUN14 in the range of $50 - 400\,\mathrm{keV}$.
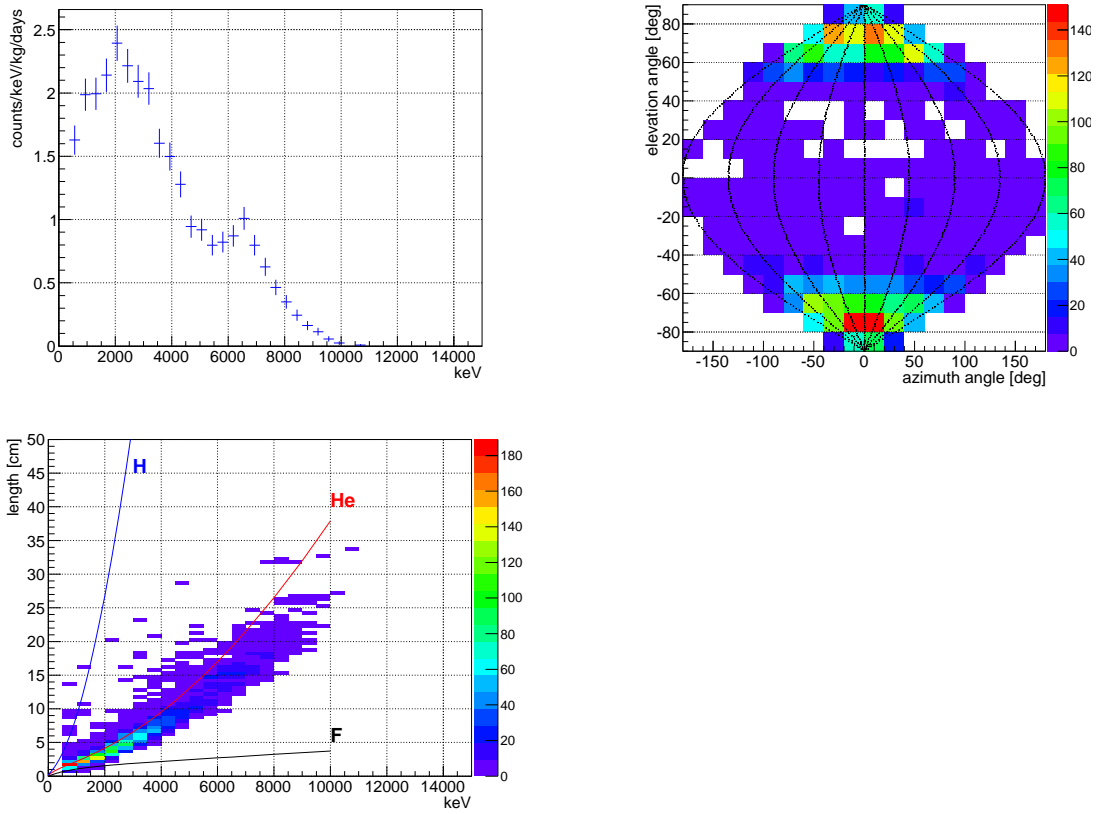
Figure 6.0.3: Obtained energy spectrum (top-left), energy-length distribution (bottom), and direction distribution (top-right) of RUN14 in the range of $500 - 15000\,\mathrm{keV}$. Only fiducial-cut is applied.

6.1   High energy backgrounds

Figure 6.1.1 schematically shows the candidates of the high-energy background. Events crossing the outer region of the fiducial area, or the veto area, as ① is removed by the fiducial-cut. Remaining events are categorized into three types; the events from $+z$ (②), the events from gas (③,③',③"), and the events from $-z$ (④,④',④",⑤,⑤', ⑥,⑦,⑦'). These three types of events differ in the drift length. By the gas diffusion, a large TOT-sum is obtained for an event with a long drift length. Figure 6.1.2 shows the simulated TOT-sums assuming three origins of the background sources. The events generated from the $-z$ region (red points; ④,④'④",⑤, ⑤',⑥,⑦,⑦'), have a short drift length and a small diffusion, and result in small TOT-sums. On the other hand, the events generated from the $+z$ region (green points; ②) and generated from the gas region (blue points; ③,③',③") have a long drift lengths and a large diffusions, and result in large TOT-sums.
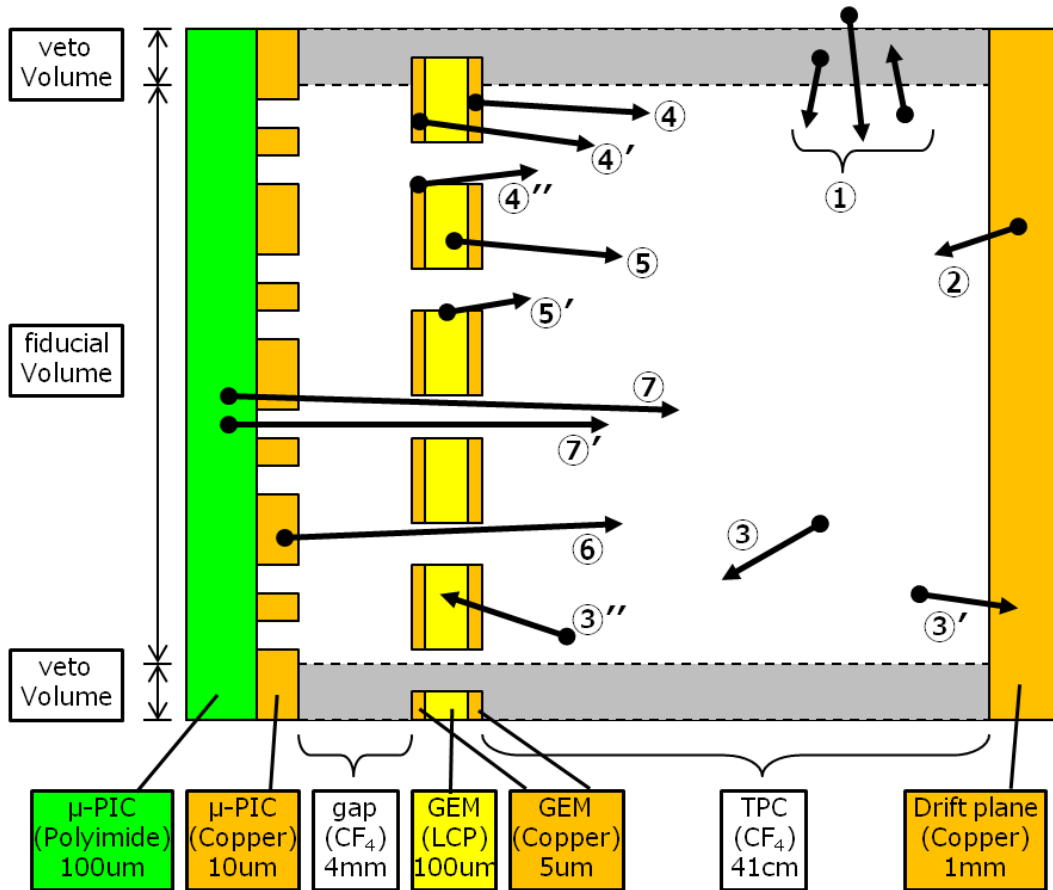
Figure 6.1.1: Candidates of high-energy background events $(500 - 15000\,\mathrm{keV})$.
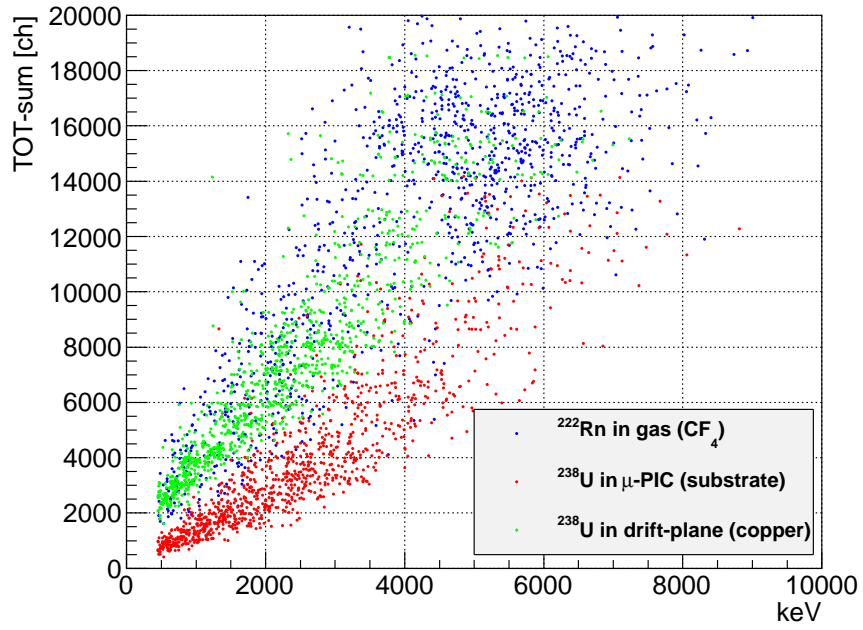
Figure 6.1.2: Simulated TOT-sum as a function of energy. Color indicates the origins of the sources.
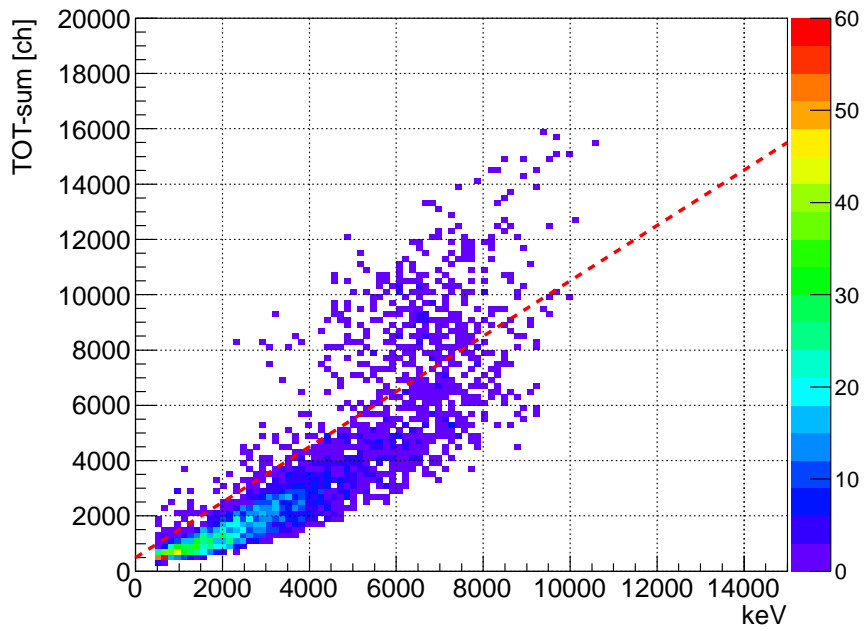
Figure 6.1.3: Measured TOT-sum as a function of energy.

Figure 6.1.3 shows the measured TOT-sum as a function of energy. By comparing with the simulated TOT-sum in Figure 6.1.2, it can be judged that the events from $-z$ region seems to be dominant, and some events from gas region also exist. The events were divided into two regions by the red dotted line to study the origin of each component. The obtained energy spectrum and direction distribution for each component are shown in Figure 6.1.4 and Figure 6.1.5, where a clear difference is seen. In the "above the line" region, the energy spectrum has a "peak" at $\sim 6\,\text{MeV}$ and the direction distribution is isotropic, while in the "below the line" region, the energy spectrum becomes "continuous" and the direction distribution concentrated to the $\pm z$ direction. We discuss on the origin of each component in the following sections.
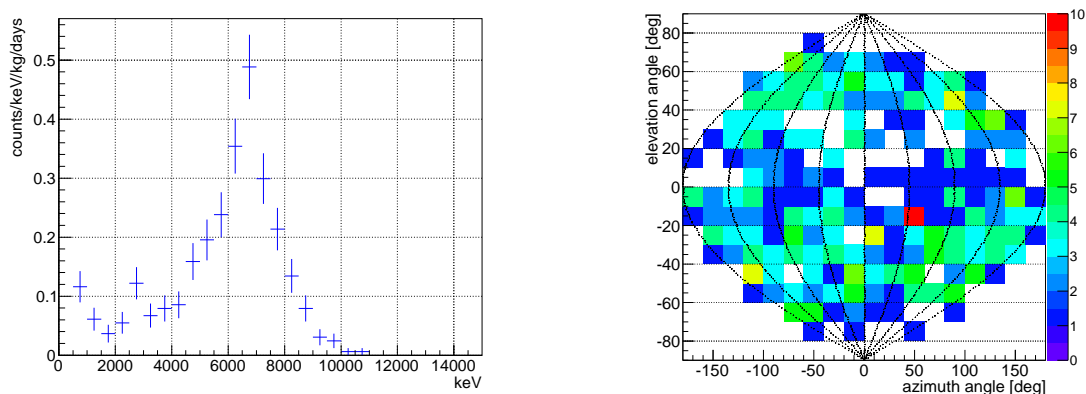
Figure 6.1.4: Obtained energy spectrum (left) and direction distribution (right) above the red dotted line in Figure 6.1.3.
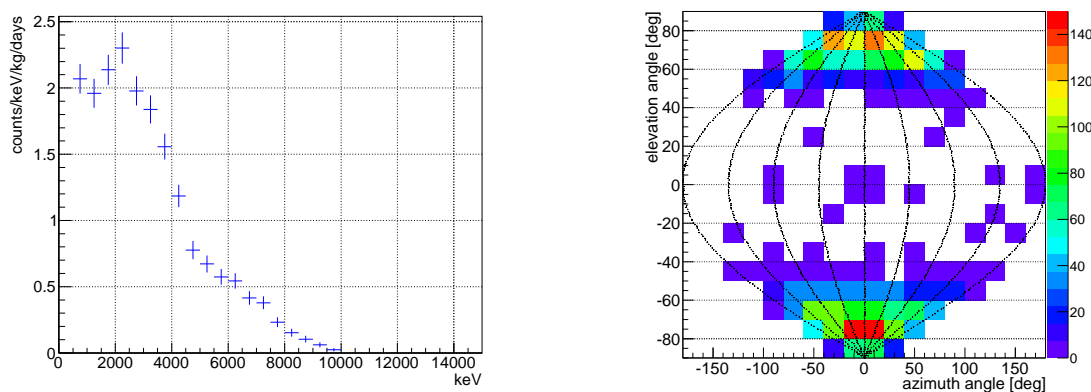
Figure 6.1.5: Obtained energy spectrum (left) and direction distribution (right) below the red dotted line in Figure 6.1.3.

6.1.1　Peak component

The peak component can be said to be due to the radon gas because 1) the peak energy is close to the expected energy of radon gas, 2) measured energy to TOT-sum correlations in Figure 6.1.3 agree with the simulated ones in Figure 6.1.2, and 3) the directions are isotropic. There are two radioactive radon isotopes; ^{220}Rn and ^{222}Rn, which decay as shown in Figure 6.0.1 making a peak at $\sim 6\,\mathrm{MeV}$ in both of the cases. Radons are generated from the decay of U-chain or Th-chain contaminated in the detector components. Radons are gas and comes out of the components and enter the detection region of μ-TPC. The life time of ^{238}U and ^{232}Th is so long that they reach the radioactive equilibrium. There is no radon when gas is re-filled in the μ-TPC. Then the number of radon N_{Rn} increases with a time constant of the radon life time $\lambda_{\mathrm{Rn}}(= \ln 2/T_{\mathrm{Rn}})$ as

$$N_{\mathrm{Rn}} = \frac{R_0}{\lambda_{\mathrm{Rn}}} \left(1 - e^{-\lambda_{\mathrm{Rn}} t}\right), \tag{6.1}$$

where t is the time from the gas re-fill, R_0 is a generation rate of the radon, T_{Rn} is the half-life of radon. Because the half-life of ^{220}Rn is so short as $T_{^{220}\mathrm{Rn}} = 55.6\,\mathrm{sec}$, the number of ^{220}Rn reaches an equilibrium within several minutes. On the contrary, the number of ^{222}Rn increases for several days because of its long half-life as $T_{^{222}\mathrm{Rn}} = 3.824\,\mathrm{day}$. We need to circulate the gas in the μ-TPC in several minute if we were to reduce ^{220}Rn by a gas circulation system (Section 4.1), which is not realistic in terms of the specification of the pump and the convection in the μ-TPC. Therefore a fundamental reduction by a material selection is required to remove ^{220}Rn. On the other hand, because the long half-life of ^{222}Rn, the radon reduction by the gas circulation system is expected. In case of reducing the radon by a gas circulation, the time dependence of the number of radon becomes

$$N_{\mathrm{Rn}} = \frac{R_0}{\lambda_{\mathrm{Rn}} + \frac{FP}{V_{\mathrm{TPC}}}} \left[1 - e^{-(\lambda_{\mathrm{Rn}} + FP/V_{\mathrm{TPC}})t}\right], \tag{6.2}$$

where $V_{\mathrm{TPC}} \simeq 125\,\ell$ is the volume of μ-TPC, F is the flow rate, P is the adsorption probability of the charcoal.

Figure 6.1.6 shows the measured time dependence the of peak component ($> 3000\,\mathrm{keV}$). Black points are measured without the gas circulation system and consistent to the time constant of ^{222}Rn. By using the gas circulation system, we obtained pink points and reduced radon rate by a factor of ~ 10 in 20 days. The pink line is fitted with the same R_0 to the black line, where P is assumed as a free parameter. Then the material of the drift cage was replaced from glass-reinforced plastic to PEEK (polyetheretherketone) as a low background material. The blue and red points are measured results in RUN14-1 and RUN14-2, respectively. The radon rate was reduced further by a factor of ~ 5. The blue and red lines are fitted by using same P

as the pink line, while R_0 is assumed as a free parameter. When cooled charcoal is added to gas circulation system and low radiative matirial is selected, the radon rate was reduced by a factor of ~ 50 in total.
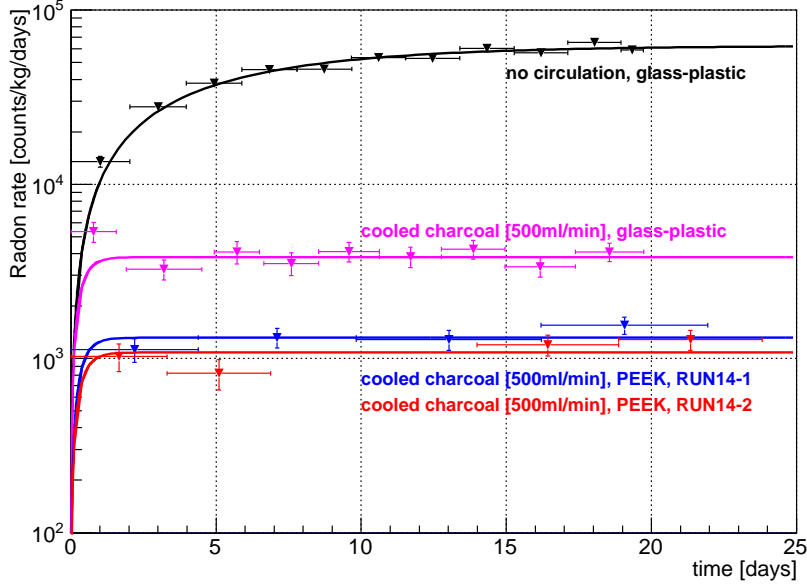
Figure 6.1.6: The measured time dependence of the peak component ($> 3000\,\text{keV}$).

Next, the amount of radon in the fiducial volume was evaluated. Because the amount of ^{222}Rn reach the equilibrium more quickly with the gas circulation system than its half-life, it is difficult to distinguish ^{222}Rn and ^{220}Rn using the time dependence anymore. Since the half-lifes of ^{218}Po, ^{214}Pb, ^{214}Bi and ^{214}Po are shorter than the that of ^{222}Rn, ^{222}Rn decays to stable ^{210}Pb in a short period compared to the decay rate of ^{222}Rn. Thus, the α particles from the daughter nucleus, ^{218}Po and ^{214}Po, are also detected when a ^{222}Rn decays in the μ-TPC. Similarly, α particles from ^{216}Po, ^{212}Pb, ^{212}Bi and ^{212}Po are also detected when a ^{220}Rn decays. More than 90% of daughter nucleus are known to be positively charged[84], and considered to drift to the drift plane where negative high voltage is applied. Since the half-life of ^{218}Po, several minute, is longer than the typical drift time of several micro seconds, ^{218}Po is considered to stick to the drift plane and decays in the place. Thus, the probability that α particles from ^{218}Po are emitted into the detection region of μ-TPC is halved; *i.e.* the other half goes into the drift plane. The daughter nucleus ^{218}Po decays on the drift plane and the probability is halved as well. For the series of ^{220}Rn, it is necessary to consider the branching ratio shown in Figure 6.0.1. In addition, since the track length of α particles of $\sim 6\,\text{MeV}$ is

95

relatively long, the fully-contained detection efficiency is precisely estimated by the simulation. By fitting the measured peak with the summarized contributions of radon daughters whose ratios are discussed above (listed in Table 6.1.1), we evaluated the content of radon for each case of ^{222}Rn and ^{220}Rn as $9.3\,\mathrm{mBq/m^3}$ and $14\,\mathrm{mBq/m^3}$, respectively.

isotope	U-chain			Th-chain			
	^{222}Rn	^{218}Po	^{214}Po	^{220}Rn	^{216}Po	^{212}Bi	^{212}Po
Energy of α collapse (MeV)	5.490	6.003	7.687	6.288	6.779	6.051	8.785
Branching ratio (%)	100	99.98	99.98	100	100	36.0	64.0
Probability of entering the gas	1	0.5	0.5	1	0.5	0.5	0.5
Detection efficiency by track length	0.52	0.45	0.31	0.40	0.36	0.44	0.23

Table 6.1.1: The parameters of radons and their progenies.

6.1.2 Continuous component

The origin of the continuous components are identified to be some combinations of ②-⑦ in Figure 6.1.1, while component ③ is estimated from the discussion in the previous section.

First of all, we discuss on the continuous component by studying the direction of the events. In the high energy region, a sufficient number of hit-strips enable to determine the head-tail of the tracks because the time-over-threshold (TOT) distribution provides the information on the energy deposition dE/dx along the tracks. Figure 6.1.7 shows the simulated energy depositions of α particles as a function of energy and length in the $0.1\,\mathrm{atm}$ CF_4 gas by using SRIM, where α particles are seen to have their energy-loss peak around $1\,\mathrm{MeV}$. This means that α particle with an energy more than $\sim 1\,\mathrm{MeV}$ increase its energy loss rate by going ahead, while α particles with a energy less than $\sim 1\,\mathrm{MeV}$ decrease its energy loss rate by going. Thus, the "normal Bragg-curve" can be seen for high energy tracks ($> \sim 4\,\mathrm{MeV}$). On the other hand, the "reversed Bragg-curve", energy loss is smaller at the end of the track, can be seen for low energy tracks ($< \sim 1\,\mathrm{MeV}$). Figure 6.1.8 shows an example of the high-energy track and TOT distribution, where the "normal Bragg-curve" in TOT distribution is seen. The direction of this event can be easily determined to be $(+x, +y, -z) \rightarrow (-x, -y, +z)$ resulting an elevation angle of $62°$. In order to examine the head-tail recognition statistically, obtained elevation angle distribution of the continuous high energy background events are shown in Figure 6.1.9 by assuming the "normal Bragg curve" regardless of the event energy. Since the "normal Bragg-curve" can be seen in $4 - 15\,\mathrm{MeV}$, obtained elevation angle distribution indicates the events run in the $+z$ direction. Besides, since the "reversed Bragg-curve" is expected in $0.5 - 1\,\mathrm{MeV}$, obtained elevation angle distribution also indicates the events are actually running towards the $+z$ direction. Thus, the direction of almost all continuous high energy backgrounds is $+z$ direction. This result disfavors the assumption ② and ③", which predict α particles going $-z$ direction.

Obtained elevation angles is high and have a peak around $70°$. This result gives us further information on the sources. The α background source should be located in the GEM or μ-PIC (④",⑤',⑥,⑦,⑦') and have to pass through the holes of GEM to make the peak around $70°$. If the copper of GEM is a background source, we should detect background from the surface copper (④) as well as the μ-PIC-side copper (④',④"), and more events of the low elevation angle should have been observed. However, obtained elevation angle is strongly concentrated to the large elevation angle. Therefore, the position of the background source is limited to the inside of the LCP of the GEM (⑤,⑤'), surface copper of the μ-PIC (⑥), and the substrate of the μ-PIC (⑦,⑦'), and each case is discussed in the following paragraphs.
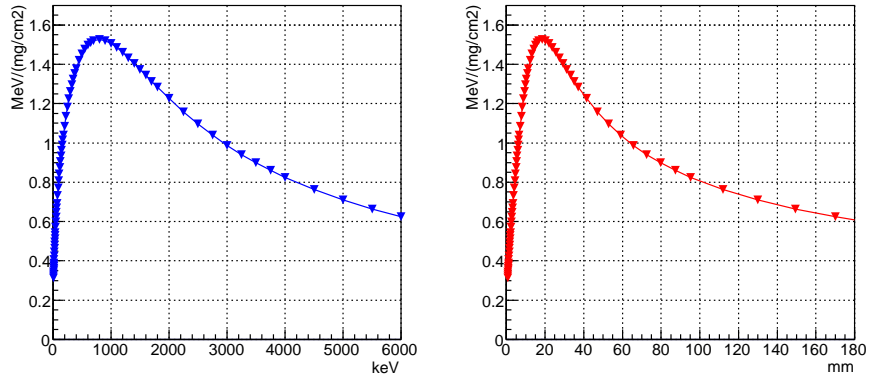
Figure 6.1.7: Energy deposition of α particles as a function of energy (left) and length (right) in the 0.1 atm CF$_4$ gas.

DM RUN14

ene_high=5468.707605 [keV]

$\theta_{elevation}$**=62.306578 [deg]**

length=13.007051 [cm]

TOT-sum=5681

roundness=0.046847
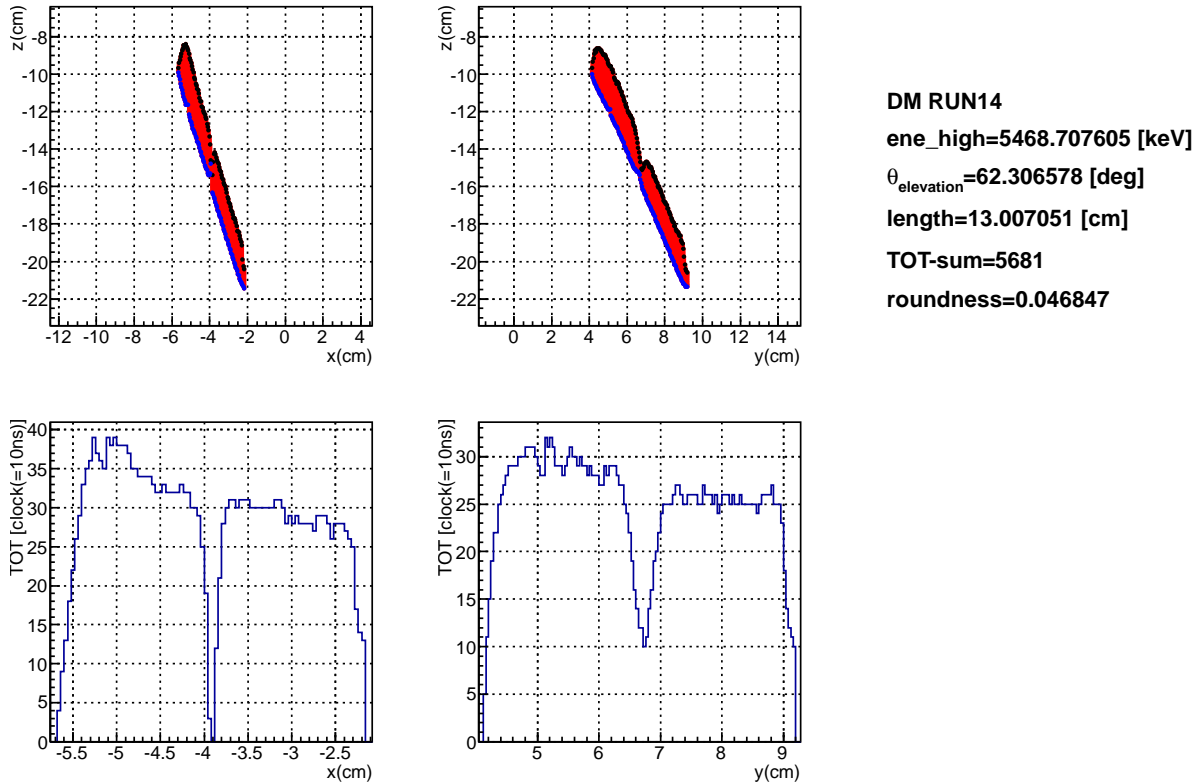
Figure 6.1.8: Example of a high energy (5470 keV) track and TOT distribution. Left-top and right-top figure shows x-z and y-z projected track, respectively. Left-bottom and right-bottom figure shows TOT distribution for x-strips and y-strips, respectively. The gap around $x = -4$ cm is due to the segmentation gap of GEM and correspond to the gap around $y = 6.7$ cm.
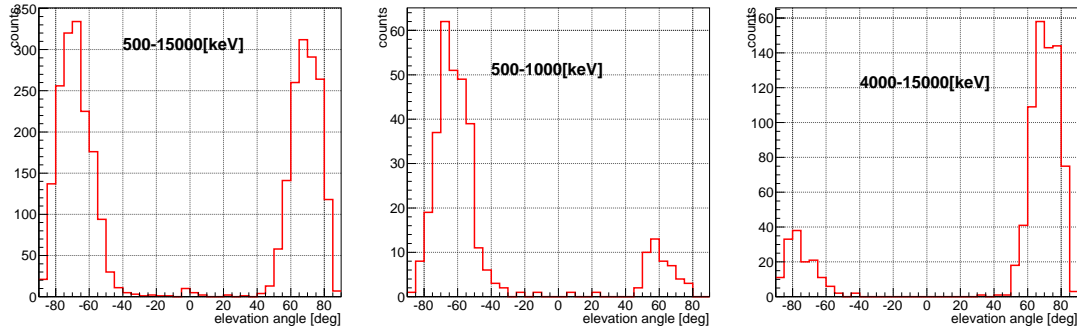
Figure 6.1.9: Measured elevation angle distribution of continuous high energy background. Left, center and right figure shows the distributions correspond to the energy region of $0.5 - 15\,\mathrm{MeV}$, $0.5 - 1\,\mathrm{MeV}$, and $4 - 15\,\mathrm{MeV}$, respectively.

Inner LCP of GEM

In order to examine the particle emission from the inside of the LCP of the GEM as a background source, we simulated the α particle emission from Th-chain in the LCP of the GEM. Figure 6.1.10 shows the simulated energy spectrum and elevation angle distribution in the energy of $0.5 - 15\,\mathrm{MeV}$. Simulated elevation angle distribution was broad to the low angle ($\sim 20 - 50^\circ$), and it was not consistent to the measurements (left of Figure 6.1.9). This is because that the events passing through the GEM hole (⑤'), which was thought to make a high elevation angle population, are less dominant than the events passing through the surface copper of the GEM with a thickness of $10\,\mu\mathrm{m}$ (⑤). Similar tendency was seen in case of assuming U-chain. Thus, the contamination of Th-chain or U-chain in the LCP of the GEM (⑤,⑤') is not found to be the main component of the high energy continuous background.
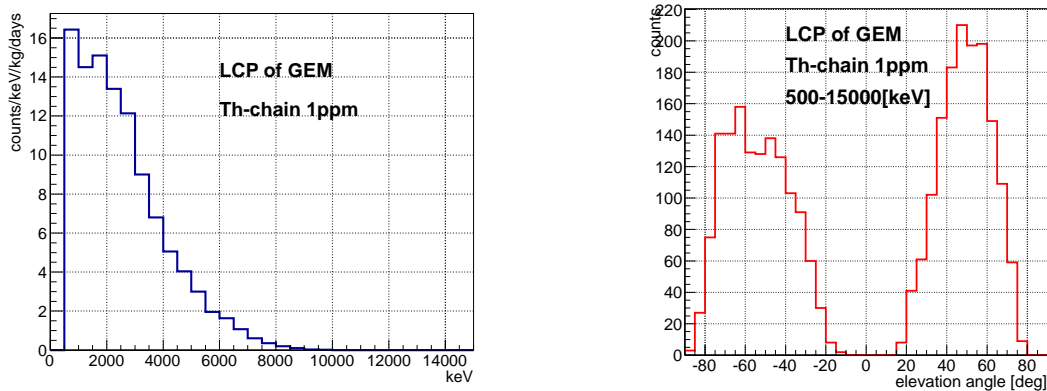
Figure 6.1.10: The simulation result of the energy spectrum (left) and elevation angle distribution in energy of $0.5 - 15\,\mathrm{MeV}$ (right) by assuming $1\,\mathrm{ppm}$ contamination of Th-chain in LCP of GEM (⑤,⑤').

99

Surface copper of μ-PIC

Next, we simulated the α particle emission from Th-chain in the surface $10\,\mu$m-thick copper of the μ-PIC. This simulation was carried out as followings. First we performed a simulation without the GEM, and then we selected the event that would cross the region corresponding to the holes of the GEM $4\,$mm above the surface of the μ-PIC. Energy deposition and hit points of track in the detection volume were analyzed. Figure 6.1.11 shows the simulated energy spectrum and elevation angle distribution in the energy of $0.5 - 15\,$MeV. Obtained elevation angle is similar to the measurements but the energy spectrum turned out to peak at $\sim 4\,$MeV, which was not consistent to the measurement (left of Figure 6.1.5). This is because that the surface copper of μ-PIC is too thin and the energy loss in the copper is too small to make low energy continuous component below $4\,$MeV. This result suggests that the contamination may exist in the deeper position of the μ-PIC. Similar tendency is seen for the simulation of U-chain. Thus, the contamination of Th-chain or U-chain in the surface copper of μ-PIC (⑥) is not found to be the main component of the continuous high energy background.
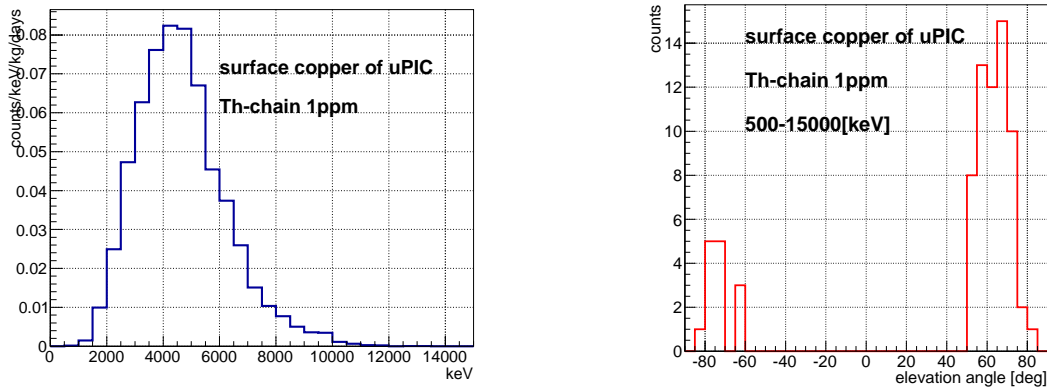
Figure 6.1.11: The simulation result of the energy spectrum (left) and elevation angle distribution in energy of $500 - 15000\,$keV (right) by assuming $1\,$ppm contamination of Th-chain in the surface copper of the μ-PIC.

Substrate of μ-PIC

The α particle emission from Th-chain and U-chain in the substrate of the μ-PIC are simulated taking account of the effect of GEM hole in the same way as described above. Also we covered a half of the surface area by copper of $10\,\mu$m as a cathode pattern. Figure 6.1.12 and Figure 6.1.13 show the simulated energy spectra and elevation angle distributions in the energy of $0.5 - 15\,$MeV for the contamination of Th-chain and U-chain, respectively. The simulated

elevation angle distributions and energy spectra reproduce the measurement results in both cases of the U-chain and Th-chain. Therefore, the substrate of μ-PIC is found to be a primary candidate of the continuous background source. Actually, glass fibers are used to reignforce the substrate, which is known to contain impurities including radioactive background sources. Here, the range of alpha particles with the energy of $< 10\,\mathrm{MeV}$ in polyimide is less than $100\,\mu$m as shown in Figure 6.1.14. Thus, the alpha particles from the the back side of the insulator ($100\,\mu$m thick of polyimide) do not come into to the detectable reagion. Although we plan the further study of radio assay using High-purity Germanium detector, in this thesis the following discussion is based on the quiantative study from the high energy continuous spectrum.
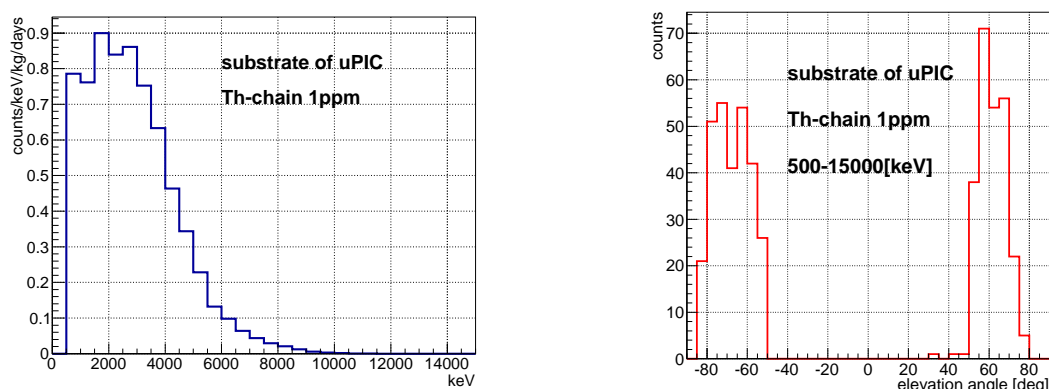
Figure 6.1.12: The simulation result of the energy spectrum (left) and elevation angle distribution in an energy range of $0.5 - 15\,\mathrm{MeV}$ (right) by assuming $1\,\mathrm{ppm}$ contamination of Th-chain in the substrate of the μ-PIC.
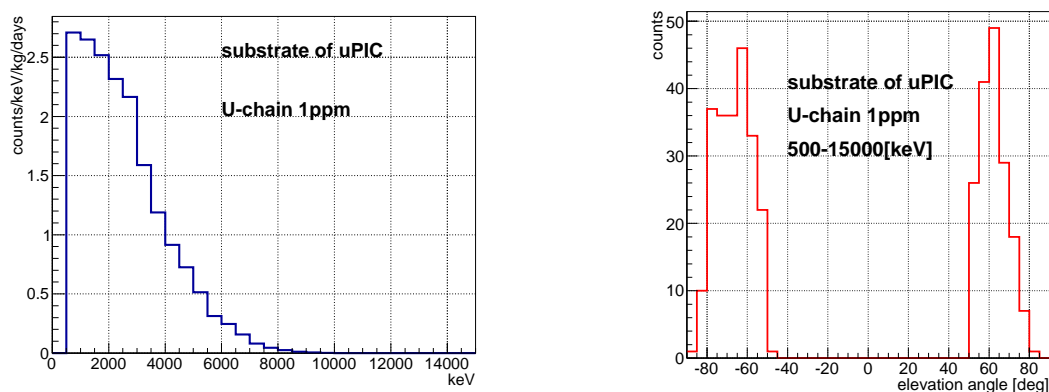
Figure 6.1.13: The simulation result of the energy spectrum (left) and elevation angle distribution in an energy range of $500 - 15000\,\mathrm{keV}$ (right) by assuming $1\,\mathrm{ppm}$ contamination of U-chain in the substrate of the μ-PIC.

101
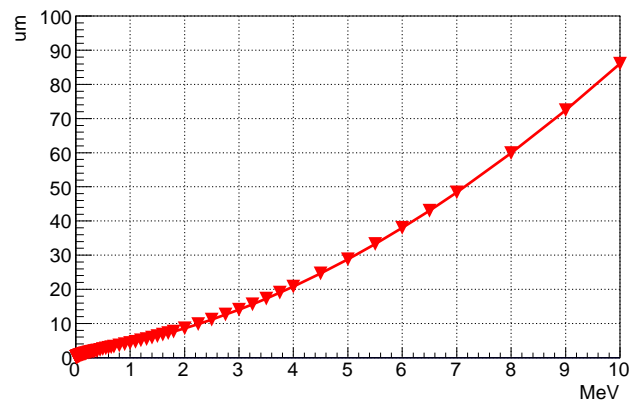
Figure 6.1.14: The calculated range of alpha particles in polyimide by SRIM. The highest energy of alpha particle of U-chain and Th-chain is 8.785 MeV, and the thickness of the insulator (polyimide) is 100 μm. Thus, the alpha particles from the back side of the insulator (polyimide) do not come into to the detectable reagion.

6.1.3 Summary of high energy background study

The high energy background sources of the dark matter search experiment are found to be radon and U/Th in the substrate of the μ-PIC. Figure 6.1.15 shows the high energy background spectrum of simulation results together with the one of measured data. In the figures, the radon component estimated in Section 6.1.1 is shown by red and orange filled histograms. The contribution of U/Th in substrate of μ-PIC are stacked with black and green histograms. The amount of U/Th was determined to explain the high energy spectrum. The case in the left top (^{220}Rn + ^{232}Th-chain model) in Figure 6.1.15 explains the measured spectrum best, while the other can still be mixed as minor components. The estimated amount of contamination for each case is written in Table 6.1.2.
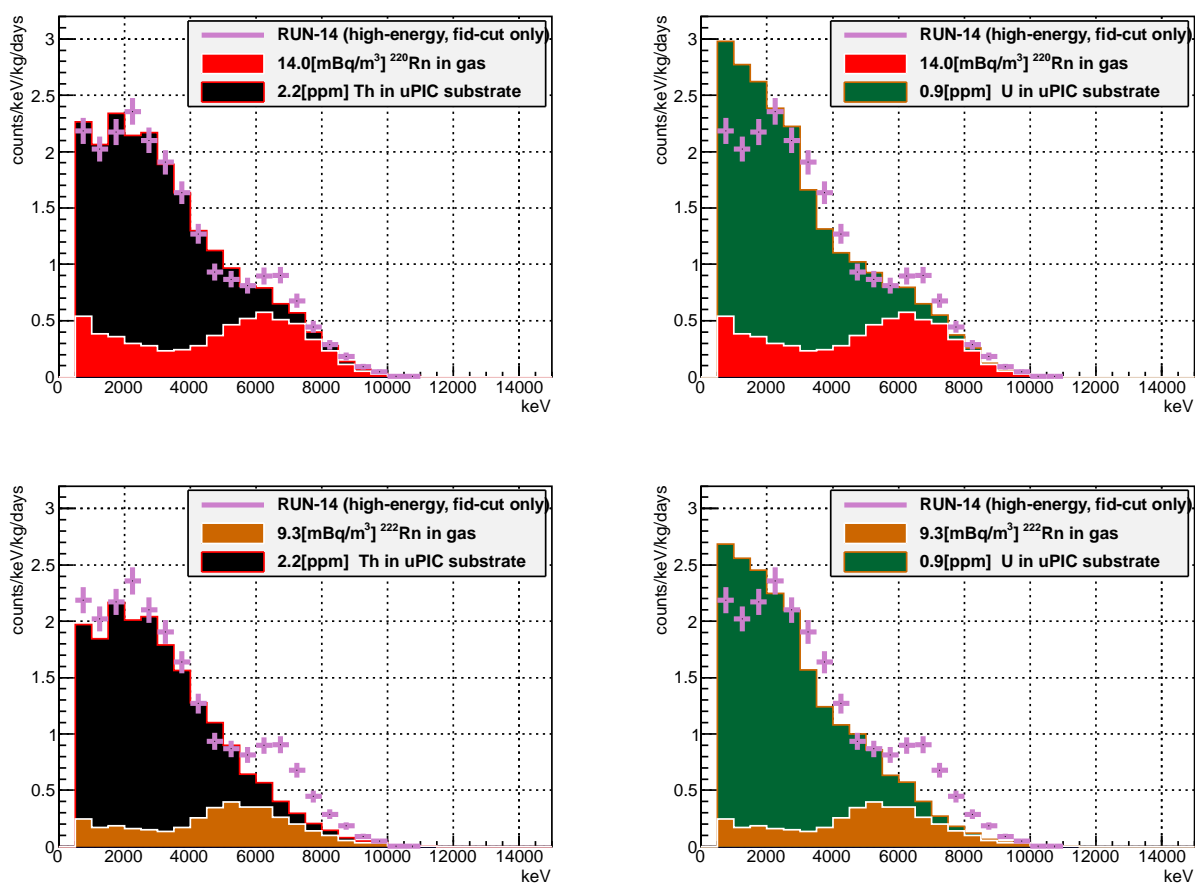
Figure 6.1.15: Energy spectrum of the high energy background. Each figure differs in the type of radon and U/Th in substrate.

component	type	amount
radon	^{222}Rn	$14\,\mathrm{mBq/m}^3$
	^{220}Rn	$9.3\,\mathrm{mBq/m}^3$
U/Th in substrate	Th-chain	$2.2\,\mathrm{ppm}$
	U-chain	$0.9\,\mathrm{ppm}$

Table 6.1.2: The estimated amount of high energy background sources. The spectrum study prefers ^{220}Rn + ^{232}Th-chain model the most, while the other components can be mixed as minor components.

6.2 Low energy backgrounds

The internal background sources was investigated based on the high energy spectrum study in the previous section. Figure 6.2.1 shows the expected candidates of the low-energy background sources. The environmental background is shown as (A), which will be discussed in Section 6.2.1. The α particles form radons in the gas make low energy background when they deposit the partial energy by stopping at GEM or drift plane (B), which will be discussed in Section 6.2.2. From the study of the high energy background as described in Section 6.1.2, substrate in μ-PIC contains U/Th-chain background sources (C), and the effect for low energy range will be described in Section 6.2.2. Although other places, surface copper of μ-PIC, GEM, and drift plane, could contain background sources to a certain extent, we consider only the dominant background source, substrate, in this thesis.

The energy of the event occurred in the region between μ-PIC and GEM, "gap region"
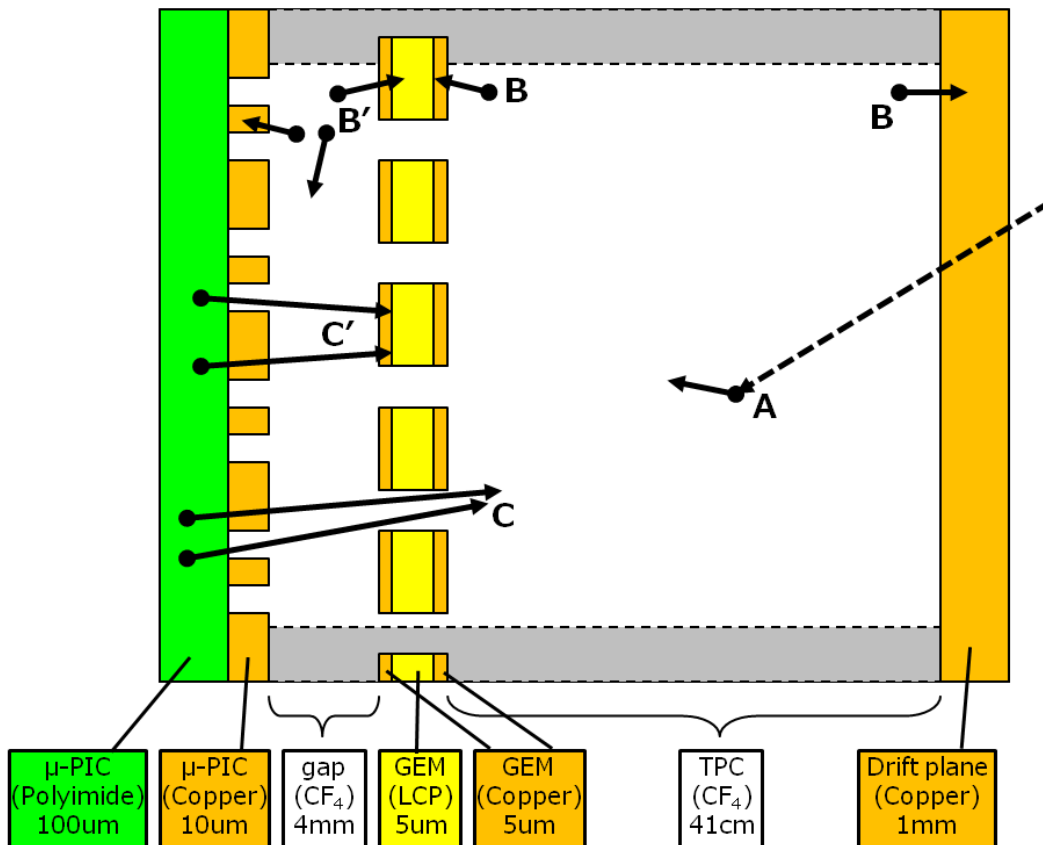
Figure 6.2.1: Candidates of low-energy background events $(50 - 400\,\mathrm{keV})$. From the discussion of high energy background as in Section 6.1, we only discuss about U/Th contamination in substrate of μ-PIC as a background from material of the detector.

(B',C'), is suppressed compared to the event in the μ-TPC (A,B.C) by the following reasons. First, α particles deposit the partial energy by stopping at GEM or μ-PIC because their track lengths are generally longer than the gap length of 4 mm. Second, since these events are not amplified by the GEM before being detected, their energies are observed as if "suppressed" by the GEM gain. Third, they run so close to the μ-PIC that the electrode-structure of the μ-PIC is seen. Thus the electron collection efficiency of μ-PIC depend on the path of the track. The α particles from radon in the gap makes low energy background, and will be described in Section 6.2.2. The α particles from substrate in μ-PIC is likely to be the most serious background, and will be described in Section 6.2.2.

6.2.1 Environmental backgrounds

In this section, the environmental background, which comes from the outside of the μ-TPC as shown (A) in Figure 6.2.1, is described. Cosmic-ray muon is a popular background sources in rare event searches. Then other major two background sources for the most of dark matter search experiments: neutrons and gamma-rays are investigated. β-rays and α-rays from the outside can be ignored because they are stopped by the vacuum chamber. Therefore the contributions of muons, neutrons, and gamma-rays are estimated in this section.

Cosmic-muon fluxes as a function of the depth in several underground laboratories in the world including our laboratory (labeled as "Super-Kamiokande") are shown in Figure 6.2.2[81]. The flux of the cosmic-ray muon at Kamioka observatory is $\sim 6 \times 10^{-8}$ /cm^2/s/sr. The muon rate passing through the effective volume of the μ-TPC was calculated to be ~ 6 counts/day. By assuming the muon rejection power as the same order of that of electron ($\sim 10^{-5}$ at 50 keV), the rate of a misidentified muon track as a nuclear track should be less than 6×10^{-3} counts/kg/days above 50 keV. That count rate is much smaller than the measured one shown in Figure 6.0.2. The secondary particles produced by cosmic-ray muons are studied as ambient gamma-rays and neutrons in the followings.

Environmental neutrons are generated in the series decay of U/Th-chain, spontaneous fission of U/Th and the spallation by the cosmic-ray muon. Generated neutrons are moderated by the material around the laboratory. Since the cross sections of the neutron capture reaction are very small for both of ^{12}C and ^{19}F, the contribution of thermal neutrons to the background spectrum was found to be negligible. The flux of fast neutrons (above 500keV) in the Kamioka mine is measured by a ^{3}He proportional counter as 2.06×10^{-6} neutron/cm^2/sec (Table 5.1.1) [82]. When neutron source is distributed uniformly to a boundless moderator which rarely absorbs neutrons, the energy spectrum of fast neutrons is known to be proportional to $1/E$[85].
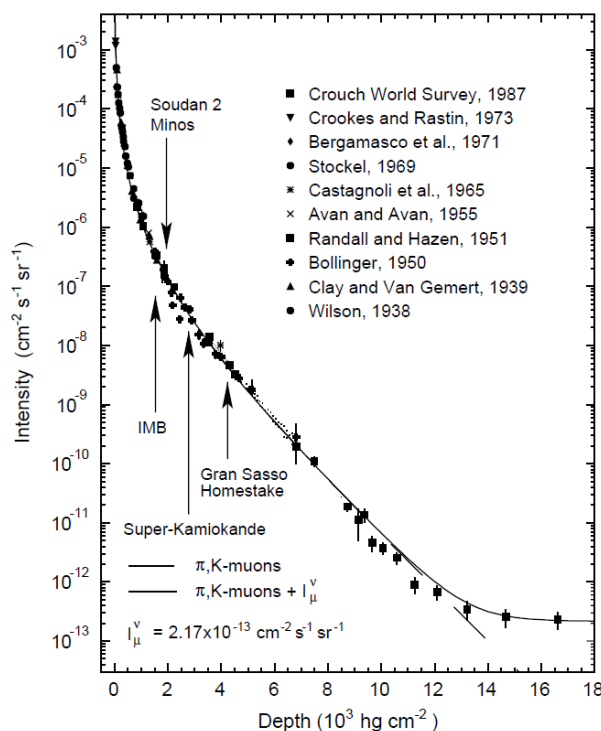
Figure 6.2.2: Cosmic-ray muon flux as a function of depth in 10^3 hg/cm^2 equivalent to km w.e.[81].

The Kamioka mine satisfies the above conditions because the laboratory is surrounded by a base rock which contains a small amount of water. By using the above assumption, we determined the flux of environmental fast neutrons in Kamioka mine as a function of energy as shown in Figure 6.2.3, and we simulated the background by neutrons. Figure 6.2.4 shows the estimated energy spectrum of nuclei recoiled by environmental neutrons. The estimated event rate at $50 - 60$ keV is 0.3 counts/keV/kg/days. Comparing to the measurements in Figure 6.0.2, the component of environmental neutrons is found to be negligible.

Ambient gamma-rays are major background sources for direct dark matter searches. Environmental gamma-rays are mainly produced in the decay of ^{40}K and U/Th-chain. Although the NEWAGE-0.3b' detector has a strong rejection power against electron tracks as described in Section 4.4.3, unrejected gamma-ray events might not be negligible. Figure 6.2.5 shows the estimated environmental gamma-ray flux in our laboratory based on the measurement by a $5 \times 5 \times 1$ cm^3 CsI(Tl) scintillator[83]. Figure 6.2.6 is obtained energy spectrum by simulation due to the environmental gamma-rays. The gamma-ray rejection power (Fig4.4.15) is taken into account. The estimated event rate at $50 - 60$ keV is 2.4 counts/keV/kg/days. Comparing to the measurements in Figure 6.0.2, the component of environmental gamma-rays is one order of magnitude less than the measurement.

107
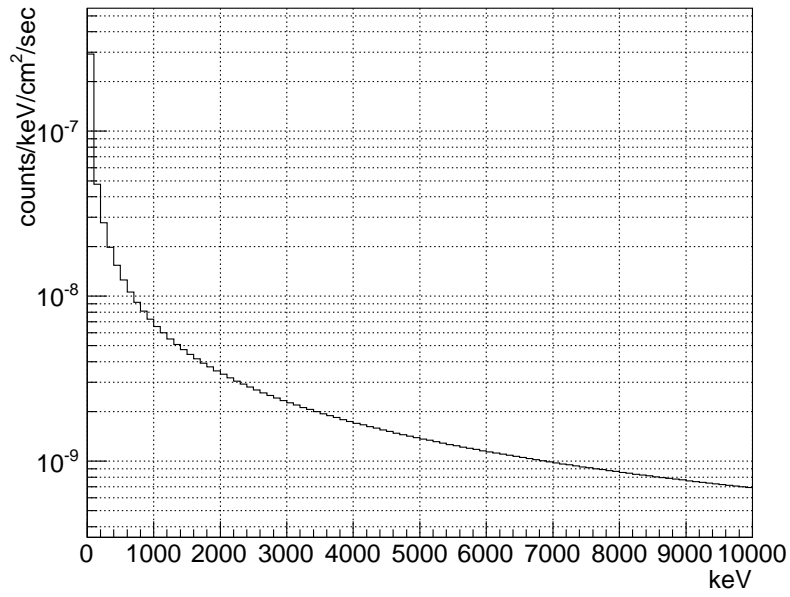
Figure 6.2.3: Estimated flux of environmental fast neutrons in Kamioka mine.
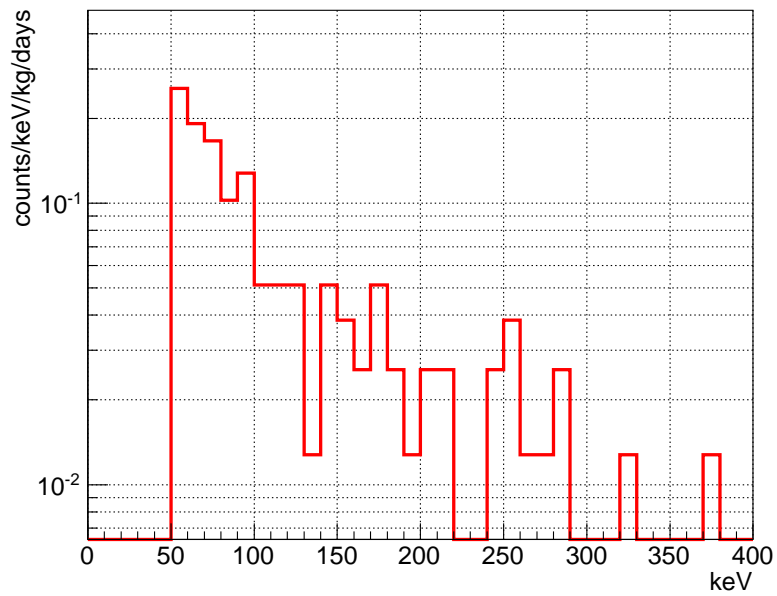
Figure 6.2.4: Estimated energy spectrum of nuclei recoiled by environmental neutrons. The estimated event rate at $50 - 60$ keV is 0.3 counts/keV/kg/days.
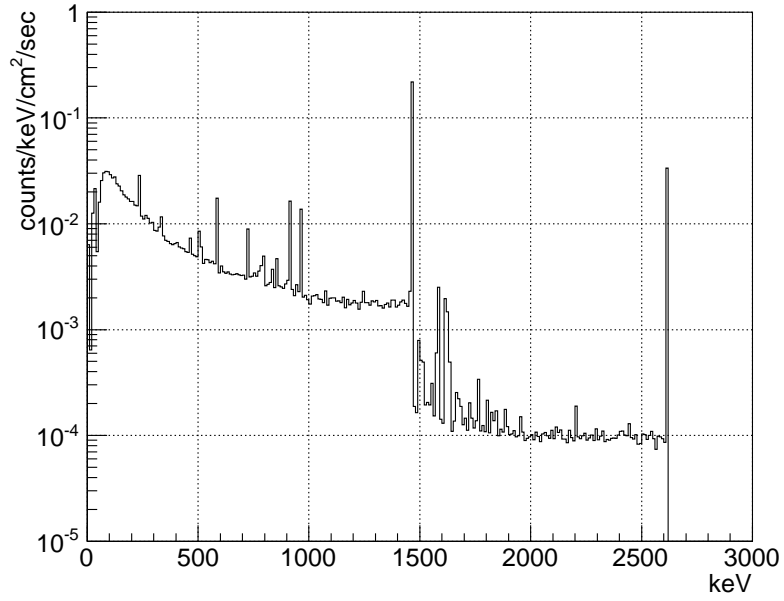
Figure 6.2.5: Estimated flux of environmental gamma-rays from measurement of a CsI(Tl) scintillator[83]. The gamma-rays from ^{40}K, U-chain, and Th-chain in the rock are taken into account.
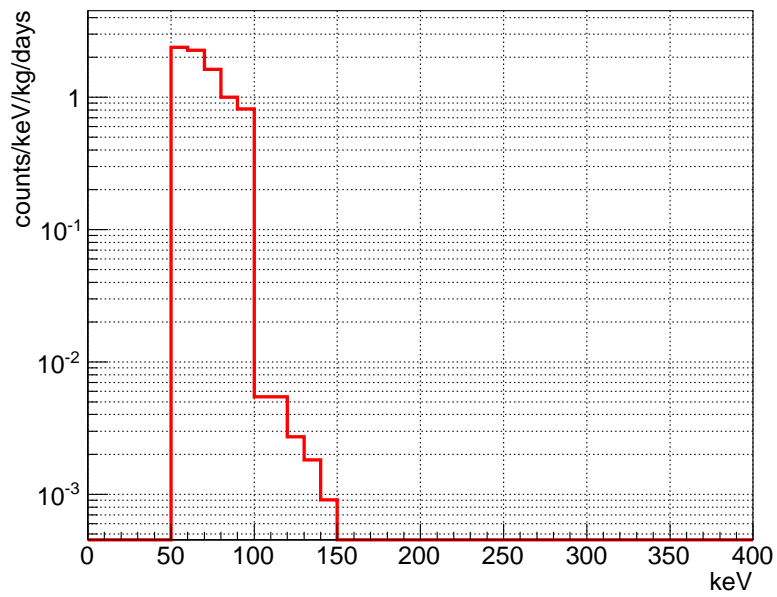
Figure 6.2.6: Estimated energy spectrum by environmental gamma-rays.

The contribution of the environmental neutrons and gamma-rays are summarized in Figure 6.2.7.
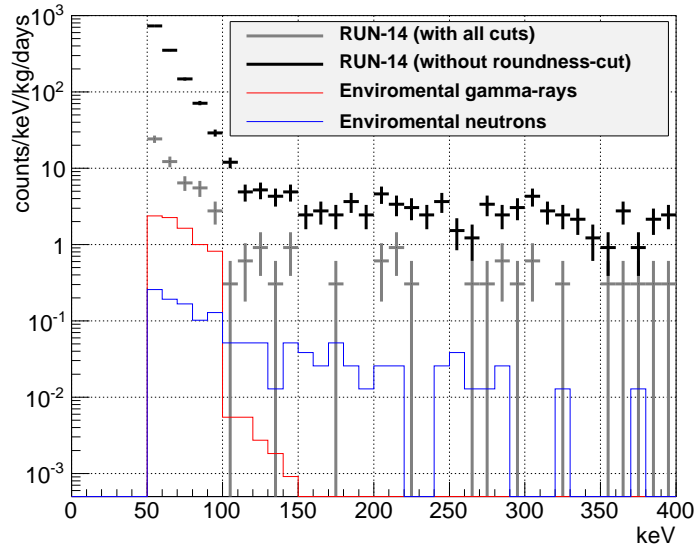
Figure 6.2.7: Energy spectrum of the measurement and estimated environmental backgrounds. Gray line shows the measured spectrum with all cuts. Black line shows the measured spectrum with all but the roundness-cut. Red line shows the estimated spectrum by environmental gamma-rays. Blue line shows the estimated spectrum by environmental neutrons.

6.2.2 Internal background

From the high energy background studies described in Section 6.1, we found that some amount of the radon in the gas and U/Th-chain in the substrate of the μ-PIC are main background sources. In this section, we explain the possibility of the contribution of the radon and the substrate to the background in the energy range of $50 - 400$ keV.

α particles from the radon in the gas makes low energy background when they deposit the partial energy by stopping at GEM or drift plane (B in Figure 6.2.1). We simulated this effect Amount of radon in the gas is evaluated in the high energy background study in Table 6.1.1. The energy spectra of the low background from these two types of radons, ^{220}Rn and ^{222}Rn, are shown in Figure 6.2.8. Althhough half of radon events which stop in the GEM will be rejected by the roundness-cut, another half which stop in the drift plane remains, and the estimated spectra was in the same order to the measured one in the energy range of $100 - 400$ keV.
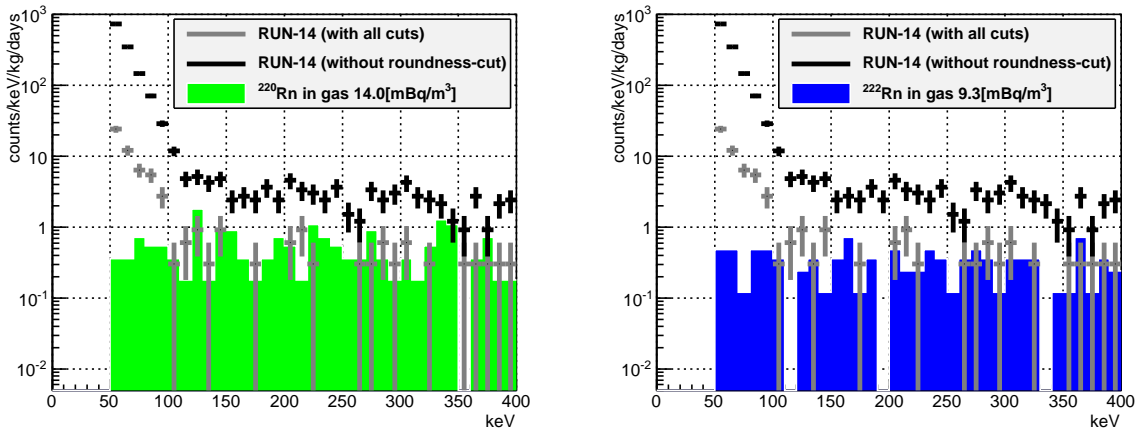
Figure 6.2.8: Estimated energy spectra of background from ^{220}Rn (left) and ^{222}Rn (right) in the detection volume. Gray line shows the measured spectrum in RUN14 with all cuts. Black line shows the measured spectrum in RUN14 with all but the roundness-cut.

Next, the contribution of the radon in the gap region (B') was studied. These gap events do not undergo the gas amplification by the GEM. By using the amount of radon in Table 6.1.1, energy spectra of background from the two types of radons, ^{220}Rn and ^{222}Rn, are estimated as shown in Figure 6.2.9. Because the gap volume is 1/100 times smaller than the detection volume, background of radon in the gap region was negligible.

As described in Section 6.1.2, the substrate in the μ-PIC contains U/Th-chain background source (C and C'), and we simulated the low energy contribution of the α particles in the detection volume from substrate by using Geant4 simulation (C). This simulation was performed in
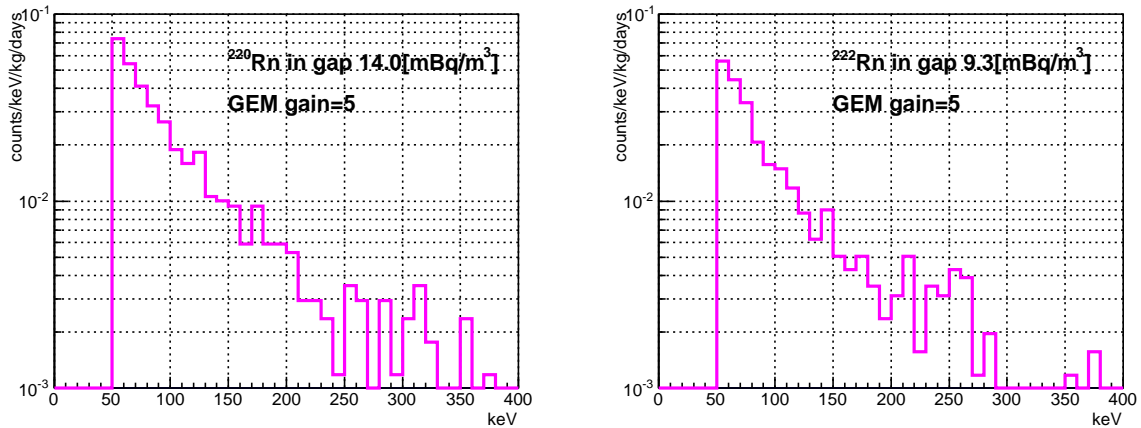
Figure 6.2.9: Estimated energy spectra of background from ^{220}Rn (left) and ^{222}Rn (right) in the gap volume. We assumed a typical gain of GEM.

the same way as the high-energy continuous background in Section 6.1.2. The contamination of U/Th-chain in substrate is evaluated by high energy background study in Table 6.1.2 We evaluated the low-energy background due to the substrate in Figure 6.2.10, which explains the flat components of measured spectrum around $100 - 400$ keV energy range. Here, α particles from substrate would be removed by the roundness-cut, and almost all measured events remained before roundness-cut were rejected by roundness-cut in the energy range of $100 - 400$ keV (Figure 5.1.3 and Figure 5.1.4). This fact supports that the measured background is due to the substrate of the μ-PIC.

Finally, the background from the substrate of the μ-PIC in the gap region (C') was studied. This simulation was performed in the similar way as the high-energy continuous background study in Section 6.1.2, except the selected events are not through the GEM hole but stopped in the GEM. These gap events do not undergo the gas amplification by the GEM, and the GEM gain was not known precisely. Therefore, several simulations were performed within the GEM gain uncertainty of 4 to 7. From the evaluated contamination values in Table 6.1.2, the low-energy background due to the gap events from the substrate was estimated and the results are shown in Figure 6.2.11, which successfully explains the rising of the background near the threshold.

In addition, we simulated the $|\cos\theta_{\mathrm{cygnus}}|$ distribution assuming the background from the substrate of the μ-PIC depositing the energy in the gap region (C') as shown in Figure 6.2.12. Compared to the measured $|\cos\theta_{\mathrm{cygnus}}|$ distribution, similar structure is seen in simulated one. This result is a cross check of the existence of background source in the substrate of μ-PIC.
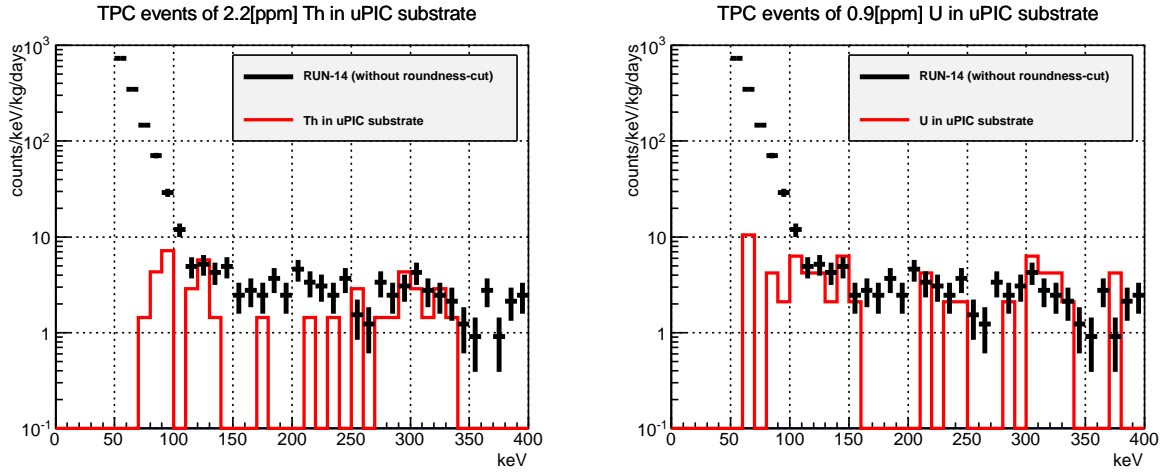
Figure 6.2.10: The estimated energy spectra of the events that α particles from radioactive impurities included in the substrate of the μ-PIC in the detection region (C in Figure 6.2.1). Left and right figure show the results by assuming 2.2 ppm of Th-chain and 0.9 ppm of U-chain, respectively. The evaluated concentration amounts of each isotope-chain discussed in Section 6.1.2 is used. We put the measured spectrum of RUN14 without the roundness-cut because the events from substrate is basically cut by the effect of z-fiducilization of roundness-cut.
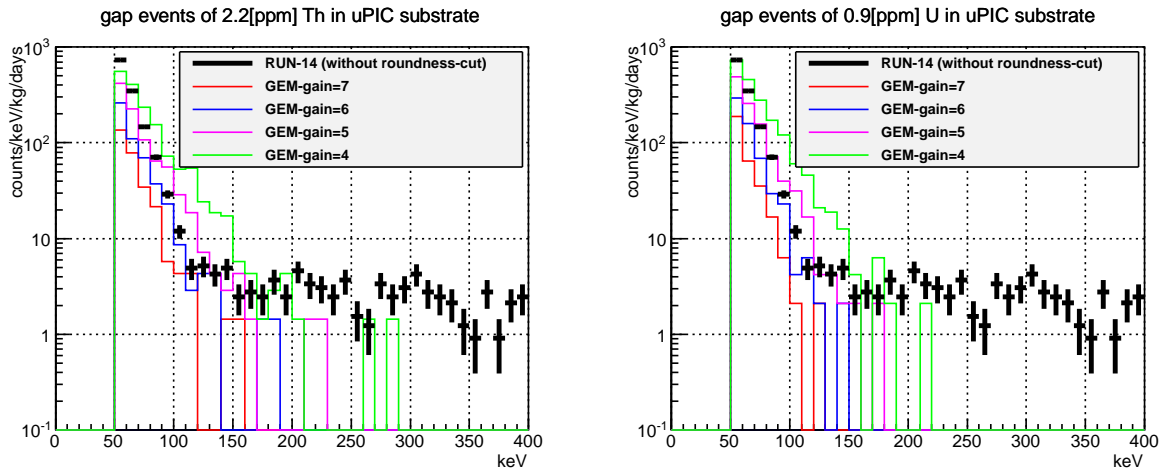
Figure 6.2.11: The estimated energy spectra of the events that α particles from radioactive impurities included in the substrate of the μ-PIC stopping in the gap region (C' in Figure 6.2.1). Left and right figure show the results by assuming 2.2 ppm of Th-chain and 0.9 ppm of U-chain, respectively. The evaluated concentration amounts of each isotope-chain discussed in Section 6.1.2 is used. We assumed several typical gain of GEM because we cannot measure the accurate gain of GEM itself. We put the measured spectrum of RUN14 without the roundness-cut because the events from substrate is basically cut by the effect of z-fiducilization of roundness-cut.

113
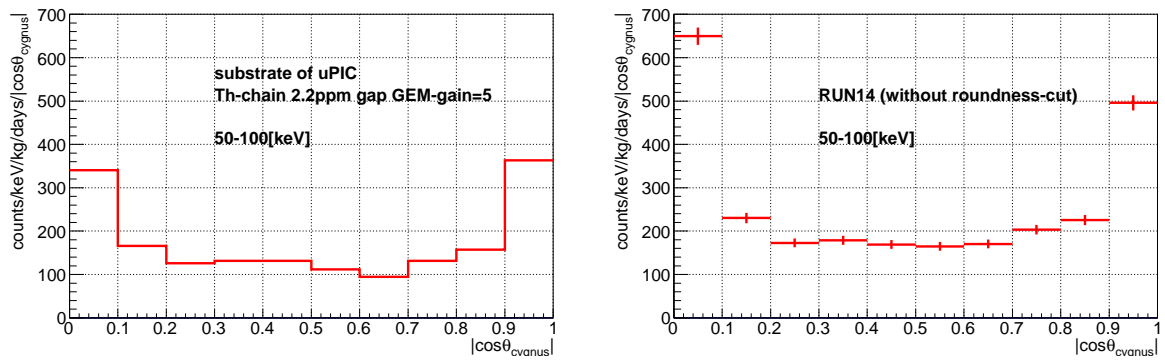
Figure 6.2.12: The simulated (left) and measured (right) $|\cos\theta_{\text{cygnus}}|$ distribution without roundness-cut. The simulation is assumed the background from the substrate of the μ-PIC depositing the energy in the gap region (C').

6.2.3 Summary of low energy background study

The contribution of the internal background is summarized in Figure 6.2.13. The measured spectrum without the roundness-cut is shown because the events from the substrate are basically rejected by the z-fiducial-cut effect of roudness-cut, and the estimation of the efficiency of roundness-cut for such low-z background events has a large uncertainty. As shown in Figure 6.2.13, the low energy background is explained well by radon and U/Th-chain in substrate of μ-PIC, which are determined from the high energy background study. Obtained component of background are summarized in Table 6.2.1. Thus, environmental backgrounds are not dominant at present.
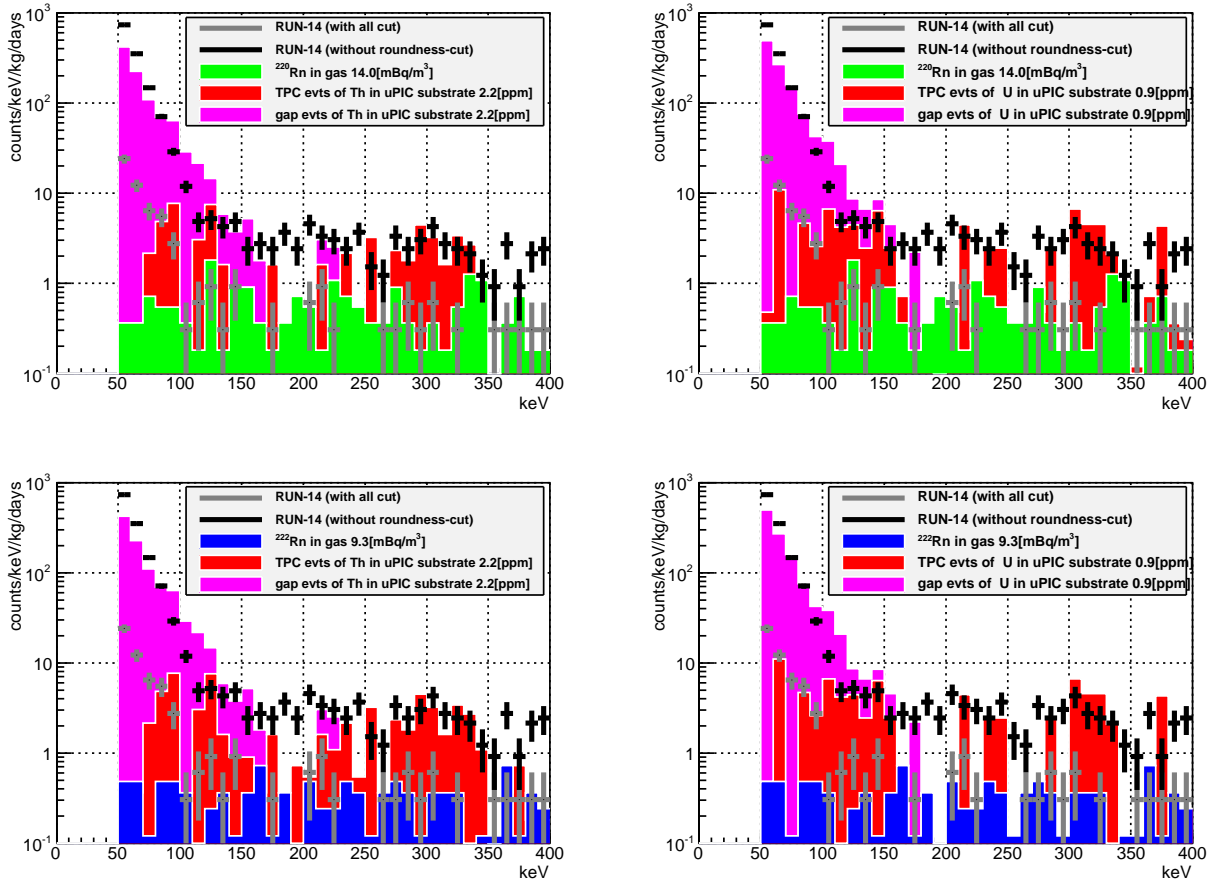
Figure 6.2.13: The estimated energy spectrum due to the radons and the radioactive impurities included in the substrate of the μ-PIC. Each figure differs in the type of radon and U/Th-chain in substrate.

particle	position	counts/keV/kg/days at $50 - 60\,\mathrm{keV}$	section
muon	cosmic	$< \sim 0.1$	6.2.1
neutron	environment	0.26	6.2.1
gamma-ray	environment	2.4	6.2.1
α (^{222}Rn/^{220}Rn)	TPC $\rightarrow$ drift plane or GEM	$< \sim 1$	6.2.2, 6.1.1
α (^{222}Rn/^{220}Rn)	gap	$< \sim 0.1$	6.2.2, 6.1.1
α (U/Th)	substrate of μ-PIC $\rightarrow$ TPC	$\sim 5 \times eff_{\mathrm{roundness-cut}}$	6.2.2, 6.1.2
α (U/Th)	substrate of μ-PIC $\rightarrow$ gap	$\sim 500 \times eff_{\mathrm{roundness-cut}}$	6.2.2, 6.1.2
RUN14 with all cut		24.1	5.1
RUN14 with all but the roundness-cut		732	5.1

Table 6.2.1: The list of background components at the threshold ($50\,\mathrm{keV}$), where $eff_{\mathrm{roundness-cut}}$ is the cut efficiency of the low-z event by the roundness-cut.

6.3   Future prospects

From the study of the remaining background the dark matter search experiment, the radioactive contamination in the substrate of the μ-PIC is found to dominate the background at the threshold energy. In the first place, a gamma-ray radio assay of the μ-PIC material by a Ge-detector is necessary to confirm the contamination of U/Th-chain. As a next step, a new μ-PIC with low-background material needs to be developed in order to improve the sensitivities. GEM signals can be used as the coincidence signal to reject the gap events.

Chapter 7

Conclusion

We developed a direction-sensitive dark matter detector, NEWAGE-0.3b' to improve the sensitivity by one order of magnitude from our previous search with NEWAGE-0.3a. NEWAGE-0.3b' was designed to have a twice larger target volume with low background material, a lowered threshold, an improved data acquisition system, and a gas circulation system with cooled charcoal. By a detector study prior to the dark matter search experiment, the energy threshold with a direction sensitivity was confirmed to be lowered from $100\,\mathrm{keV}$ to $50\,\mathrm{keV}$.

A direction-sensitive dark matter search in Kamioka underground laboratory with NEWAGE-0.3b' was performed from July 17th, 2013 to November 12th, 2013. With an exposure of $0.327\,\mathrm{kg}\cdot\mathrm{days}$, a new $90\%\,\mathrm{C.L.}$ SD cross section limit $557\,\mathrm{pb}$ for WIMP mass of $200\,\mathrm{GeV}$ was obtained (Figure 7.0.1). This result improved the limit by ~ 10 times from previous measurement, and marks the best direction-sensitive limit.

The identification of the background soruce is very important to improve the low background detector. Remaining background was studied in detail, and the substrate of μ-PIC was found to be the dominant background source. If a new low-background μ-PIC is developed, the background level will be limited by environmental gamma-rays and it will be reduced by an improvement of the tracking algorithm. The expected limit with the above improvements will reach to the DAMA region as shown in Figure 7.0.1. Further sensitivity improvements will be achieved by recognizing the sense of the track, improving angular resolution, and using large-size detectors with long-term operation, then a direction-sensitive dark matter search of the whole DAMA region will be performed.
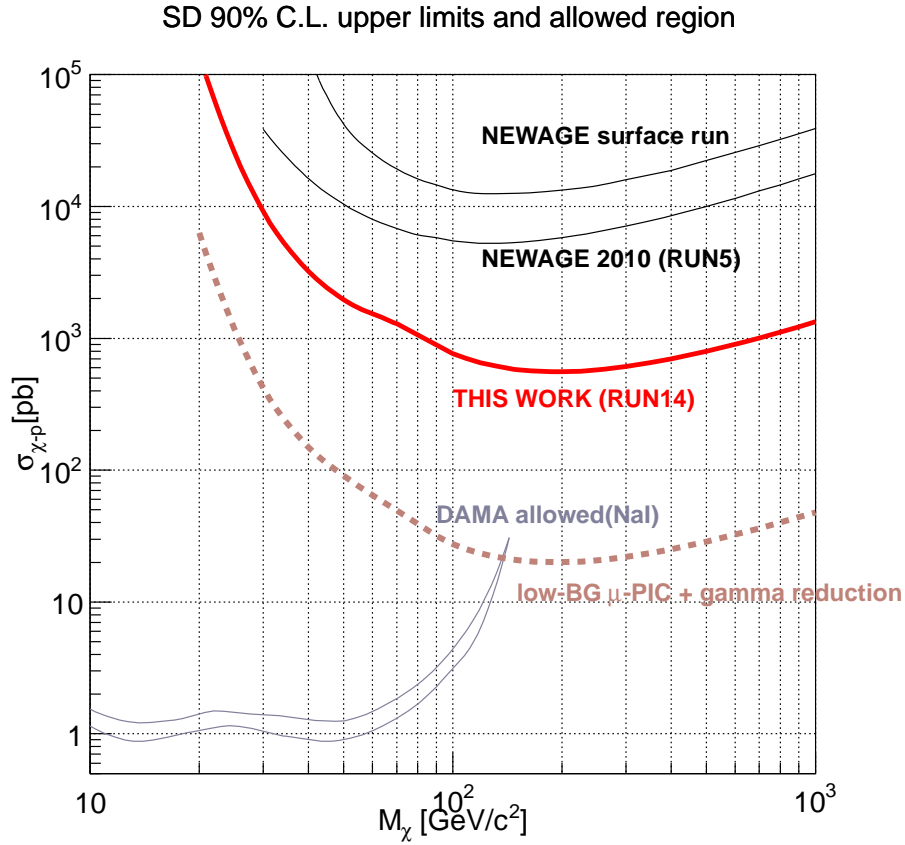
Figure 7.0.1: Limits of SD cross section, $\sigma^{\mathrm{SD}}_{\chi-\mathrm{p}}$, as a function of mass of WIMP mass M_χ. Red thick solid line is the result of a directional method in this work. Black thin lines labeled "NEWAGE surface run" and "NEWAGE 2010 (RUN5)" are previous results measured at surface and Kamioka, respectively[83]. Brown thick dotted line is a expected limit by reducing the U/Th contamination in μ-PIC and enviromental gamma-rays. Allowed region (DAMA[39]) is shown for comparison.

Acknowledgements

Bibliography

[1] P. A. R. A. et al. *arXiv:1303.5076 (submitted to Astronomy and Astrophysics)* **1** (2013) 1.

[2] D. J. Eisenstein et al. *Astrophys. J.* **633** (2005) 560.

[3] R. A. Knop et al. *Astrophys. J.* **598** (2003) 102.

[4] F. Z. et al. *Astrophys. J.* (1937) 217.

[5] K. G. Begeman, A. H. Broeils, and R. H. Sanders *MNRAS* (1991) 523.

[6] M. Loewenstein and R. F. M. et al. *Astrophys. J.* (1996) 83.

[7] D. C. et al. *Astrophys. J.* (2006) L109.

[8] D. J. Fixsen *AstroPhys. J.* **707** (2009) 916.

[9] D. Kirkman et al. *Astrophys. J. Suppl. Ser.* **149** (2003) 1.

[10] G. Jungman et al. *Phys. Rep.* **267** (1996) 195.

[11] G. Servant et al. *New J. Phys.* **4** (2002) 99.

[12] N. Arkani-Hamed et al. *J. High Energy Phys.* **07** (2002) 034.

[13] R. D. Peccei and Helen R. Quinn et al. *Phys. Rev. Lett.* **38** (1977) 1440.

[14] L. D. Luffy and K. Bibber et al. *New Journal of Physics* **11** (2009) 105008.

[15] P. Sikivie et al. *Phys. Rev. Lett.* **51** (1983) 1415.

[16] S. J. Asztalos et al. *Phys. Rev. Lett.* **104** (2010) 041301.

[17] M. Kawasaki et al. *J. Phys. Soc. Jpn.* **77, Suppl. B** (2008) 19.

[18] A. Boyarsk et al. *Ann. Rev. Nuc. Part. Sci.* **59** (2009) 191.

[19] G. M. Fuller et al. *Phys. Rev. D* **68** (2003) 103002.

[20] Hardy M. Hodges *Phys. Rev. D* **47** (1993) 456.

[21] Kalliopi Petraki, Raymond R. Volkas *Int. J. Mod. Phys. A* **28** (2013) 1330028.

[22] John Ellis, V. E. Mayes and D. V. Nanopoulos *Phys. Rev. D* **74** (2006) 115003.

[23] Spencer Chang, Ralph Edezhath, Jeffrey Hutchinson and Markus Luty *hep-ph 1307.8120v1* (2013).

[24] S. D. Hunter *Astrophys. J.* **481** (1997) 205.

[25] A. H. E. Tempel and M. Raidal *J. Cosmology Astropart. Phys.* **09** (2012) 032.

[26] S. Desai et. al *Phys. Rev. D* **70** (2004) 083523.

[27] M.G.Aartsen et. al *33nd International Cosmic Ray Conference* (2013).

[28] O. Adriani et. al *Phys. Rev. Lett.* **111** (2013) 081102.

[29] M. Aguilar et. al *Phys. Rev. Lett.* **110** (2013) 141102.

[30] ALEPH Collaboration *Phys. Lett. B* **583** (2004) 247.

[31] A. Arbey et al. *Phys. Lett. B* **720** (2013) 153.

[32] H. Baer et al. *arXiv:1307.5248 (hep-ph)* (2013).

[33] J. D. Lewin and P. F. Smith *Astropart. Phys.* **6** (1996) 87.

[34] J. Ellis et al. *Phys. Lett. B* **481** (2000) 304.

[35] A. Ferstl and K. A. Olive *Phys. Rev. D* **59** (1999) 055009.

[36] D. Spergel *Phys. Rev. D* **37** (1988) 1353.

[37] R. Bernabei et al. *J. Phys. Conf. Ser.* **375** (2012) 012002.

[38] R. Bernabei et al. *Eur. Phys. J. C* **67** (2010) 39.

[39] C. Savage et al. *Phys. Rev. D* **70** (2004) 123513.

[40] R. Bernabei et al. *Phys. Lett. B* **480** (2000) 23.

[41] G. J. Alner et al. *Phys. Lett. B* **616** (2005) 17.

[42] H. S. Lee, et al. (KIMS Collaboration) *Phys. Rev. Lett.* **99** (2007) 091301.

[43] R. B. et al. *New J. Phys.* **2** (2000) 15.1.

[44] A. Minamino *Doctorr Thesis* **University of Tokyo** (2008).

[45] E. Aprile et al. (XENON Collaboration) *Phys. Rev. Lett.* **109** (2012) 181301.

[46] E. Aprile et al. (XENON Collaboration) *Phys. Rev. Lett.* **111** (2013) 021301.

[47] D. S. Akerib et al. (LUX Collaboration) *arXiv:1310.8214* (2013).

[48] P. B. et al. *Astropart. Phys.* **28** (2000) 495.

[49] Z. Ahmed et al. (CDMS Collaboration) *Phys. Rev. lett.* **102** (2009) 011301.

[50] C. E. Aalseth et al. *Phys. Rev. D* **88** (2013) 012002.

[51] G. Angloher et al. *Eur. Phys. J.* **C** (2012) 27.

[52] J. Barreto et al. *Phys. Lett. B* **711** (2012) 264.

[53] E. Behnke et al. *Phys. Rev. D* **86** (2012) 052001.

[54] M. Felizardo et al. *1106.3014v3* (2011).

[55] S. Archambault et al. *Phys. Lett. B* **711** (2012) 153.

[56] E. Daw et al. *Astropart. Phys.* **35** (2012) 397.

[57] S. Ahlen et al. *Phys. Lett. B* **695** (2011) 124.

[58] K. Miuchi *et. al. Phys. Lett. B* **686** (2010) 11.

[59] D. Santos *et. al. J. Phys. Conf. Ser.* **309** (2011) 012014.

[60] T. Naka et al. *Nucl. Instrm. Methods Phys. Res. Sect. A* **581** (2007) 761.

[61] A. Drukier et al. *1206.6809v1* (2012).

[62] K. Fushimi et al. *J. Phys. Conf. Ser.* **469** (2013) 012011.

[63] J. Cherwinka et al. *Astropart. Phys.* **35** (2012) 749.

[64] Y. Shimizu et al. *Phys. Lett. B* **633** (2006) 195.

[65] D. R. Nygren *J. Phys. Conf. Ser.* **460** (2013) 012006.

[66] S. F. Biagi *Nucl. Instr. Meth. Phys. Res. A* **283** (1989) 716.

[67] J.F. Ziegler, J.P. Biersack *SRIM The Stopping and Range of Ions in Matter, Code* (1985).

[68] A. H. et al. *Rad. Phys. and Chem.* **77** (2008) 1311.

[69] S. E. Vahsen *EAS publication series, Proceedings of CYGNUS 2011, Third International Conference on Directional Detection of Dark Matter* **53** (2012) 43.

[70] J. P. Cussonneau *Nucl. Instr. and Meth. in Phys. Res. A* **419** (1998) 452.

[71] F. Sauli and A. Sharma *Annu. Rev. Nucl. Part. Sci* **49** (1999) 341.

[72] G. Aad *JINST* **3** (2008) P07007.

[73] T. Tanimori *et. al. Phys. Lett. B* **578** (2004) 241.

[74] J. Ellis et al. *Phys. Rev. D* **63** (2001) 065016.

[75] A. Takada *et. al. Nucl. Instrm. Methods Phys. Res. Sect. A* **573** (2007) 195.

[76] H. K. et al. *IEEE Nucl. Sci. Symp. Conf. Rec.* **1** (2005) 371.

[77] S. Agostinelli et al. *Nucl. Instr. Meth. Phys. Res. A* **506** (2003) 250.

[78] K. Miuchi *Oral presentation at CYGNUS2011, 7-10 June 2011, AUSSOIS (France)* (2011).

[79] K. Nakamura *et. al. JINST.* **7** (2011) C02023.

[80] W. H. Press, S. A. Teukolsky, W. T. Vetterling, and C. P. Flannery, *NUMERICAL RECIPES in C.* Cambridge University Press, New York, 1988.

[81] SK Collaboration *Nucl. Instrm. Methods Phys. Res. Sect. A* **501** (2003) 418.

[82] A. Minamino *Master Thesis* **University of Tokyo** (2004).

[83] H. Nishimura *Doctor Thesis* **Kyoto University** (January 2009).

[84] H. Nishimura *et. al. Astropart. Phys.* **31** (2009) 185.

[85] S. R. Hashemi-Nezhad and L. S. Peak *Nucl. Instrm. Meth. Phys. Res. A* **357** (1995) 524.